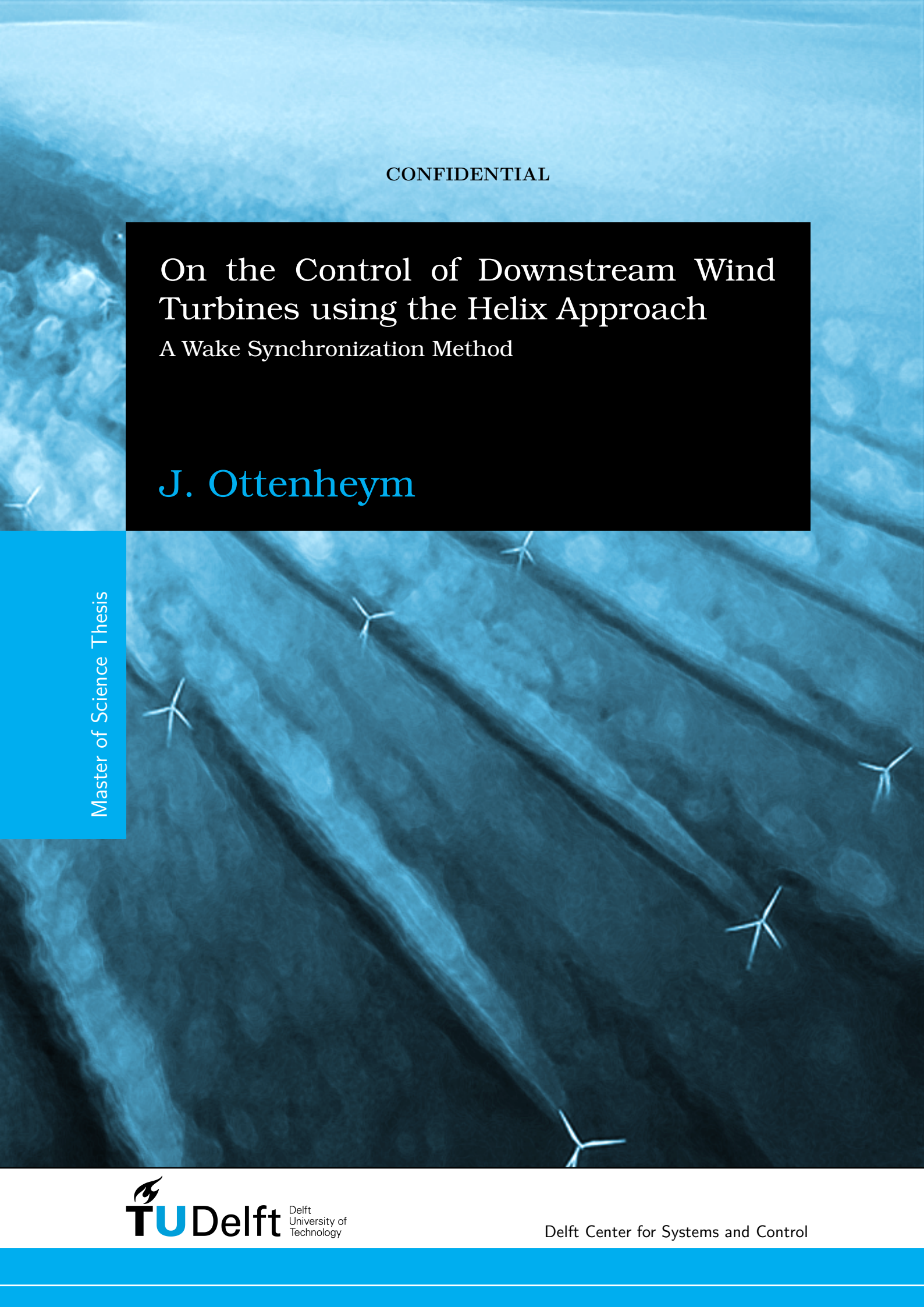


CONFIDENTIAL

# On the Control of Downstream Wind Turbines using the Helix Approach

## A Wake Synchronization Method

J. Ottenheym

Master of Science Thesis

TU Delft Delft University of Technology

Delft Center for Systems and Control

MSCCONFIDENTIAL

# On the Control of Downstream Wind Turbines using the Helix Approach

## A Wake Synchronization Method

Master of Science Thesis

For the degree of Master of Science in Systems and Control at Delft University of Technology

J. Ottenheym

March 24, 2023

Faculty of Mechanical, Maritime and Materials Engineering (3mE) · Delft University of Technology







Copyright © Delft Center for Systems and Control (DCSC)
All rights reserved.

Delft University of Technology
Department of
Delft Center for Systems and Control (dcsc)

The undersigned hereby certify that they have read and recommend to the Faculty of Mechanical, Maritime and Materials Engineering (3mE) for acceptance a thesis entitled

On the Control of Downstream Wind Turbines using the Helix Approach

by

J. Ottenheym

in partial fulfillment of the requirements for the degree of

Master of Science Systems and Control

Dated: March 24, 2023

Supervisor(s):

Prof. dr. ir. J.W. van Wingerden

Ir. A.A.W. van Vondelen

Ir. R.T.O. Dinkla

Reader(s):

Dr. ir. S.T. Navalkar

Dr. ir. W. Yu

# Abstract

The placement of wind turbines in wind farms is economically beneficial to the industry. Consequently, the wake generated by the upstream turbines introduces interactions with downstream turbines that significantly affect power generation. However, it is common practice to control the individual turbines to operate at their optimal settings and neglect the wake effect. Turbines in a wake experience lower wind speeds and an increase in turbulence. This results in lower power generation and increased fatigue loads on the downstream turbine. Wind farm control aims to increase overall power generation and reduce fatigue loads by considering all turbines in the wind farm.

Recently, numerous studies have been conducted to control the wake itself. The helix approach is one such strategy and seeks to initiate better mixing of the wake. For this, it uses Individual Pitch Control (IPC) to create sinusoidal blade bending moments acting on the rotor disc. This in turn creates a helical structure in the velocity of the wind, allowing it to better mix with the surrounding energy-rich wind. As a result, the waked downstream turbine experiences an increase in power due to the reduced velocity deficit in the wake. An extensive load analysis of the helix method has shown that the rotational frequency of this helical wake can be measured in the bending moments of the waked downstream turbine. To further develop the field of dynamic wake mixing, this work investigated the initialization of the helix method in a downstream turbine by amplifying these signals through synchronization with the incoming helical wake.

This method was tested in simulation environments with increasing levels of fidelity and number of turbines simulated. The results with low fidelity showed that synchronization could be achieved without loss of performance. In addition, less pitch actuation was required to generate large bending moments due to amplification. The final experiment was conducted for a three-turbine setup and was performed in a high-fidelity model using Computational Fluid Dynamics (CFD) methods. Here it was found that $-90°$ out-of-phase synchronization with the incoming helical wake resulted in a 9.8% increase in power generation in a turbine further downstream. These results demonstrate the clear potential of wake synchronization in a multi-turbine setting. This study, therefore, contributes to the field of dynamic wake mixing by introducing a novel field of wake synchronization.

# Table of Contents

**Acknowledgements** **xv**

**1 Introduction** **1**
1-1 Wind Turbines . . . 1
1-1-1 Turbine Wake . . . 3
1-2 Wind Farm Control . . . 3
1-2-1 Wake Control Strategies . . . 3
1-2-2 Load Impact of Dynamic Wind Farm Wake Mixing Strategies . . . 5
1-3 Problem Formulation and Research Outline . . . 6
1-3-1 Research Questions . . . 7
1-4 Report Structure . . . 8

**2 Preliminaries and Controller Strategies** **9**
2-1 Multi-Blade Coordinate Transform . . . 9
2-1-1 Change of Reference Frame . . . 10
2-1-2 The MBC Transformation and the Helix Method . . . 11
2-2 Interaction with a Downstream Turbine . . . 13
2-2-1 Phase Information of the Helical Wake . . . 15
2-3 Closed-Loop Helix Wake Synchronization . . . 17
2-3-1 Optimal Azimuth Offset . . . 17
2-3-2 Sensitivity in the Phase . . . 18
2-3-3 Controller Options . . . 19
2-4 Recursive Least Squares Estimator . . . 21
2-4-1 Phase Information Exploit . . . 21
2-4-2 The RLS Algorithm . . . 22
2-4-3 The Square-Root RLS Algorithm . . . 23
2-4-4 Converging to the Phase of the Helical Inflow . . . 24

2-4-5 RLS Controller Scheme . . . 24
2-5 Kalman Filter-Based Estimator . . . 25
2-5-1 Augmenting the Helical Disturbance . . . 26
2-5-2 Kalman Filter Estimation of the Helical Input Disturbance . . . 27
2-5-3 KF Controller Scheme . . . 28
2-6 Concluding Remarks on the Controller Strategy . . . 28

**3 Phase Synchronization in Low-Order Synchronous Machine 31**
3-1 Model Description . . . 31
3-1-1 Experiment Setup . . . 33
3-2 Results Low-Order Model . . . 34
3-2-1 Reference Tracking & Disturbance Rejection . . . 35
3-2-2 Effect of the Signal-to-Noise Ratio . . . 36
3-2-3 Out-of-Phase Disturbance Rejection . . . 37
3-3 Concluding Remarks Low-Order Model . . . 38

**4 Helix Synchronization in High-Order Wind Turbine Models 39**
4-1 NREL 5-MW Reference Wind Turbine . . . 39
4-1-1 MBC Transformed Linearized Wind Turbine Model . . . 40
4-2 Low-Fidelity Simulation Setup: OpenFAST . . . 43
4-2-1 TurbSim Custom Wind Inflow . . . 43
4-3 High-Fidelity Simulation Setup: QBlade & SOWFA . . . 47
4-3-1 QBlade Setup . . . 47
4-3-2 SOWFA Setup . . . 48
4-4 Low-Fidelity Results: OpenFAST Simulations . . . 49
4-4-1 Phase Estimation Rotating Disc . . . 50
4-4-2 Effect of Turbine Distance . . . 51
4-4-3 Effect of Pitch Amplitude . . . 52
4-4-4 Synchronization with the Helical Wake . . . 53
4-4-5 Rejection of the Helical Wake . . . 54
4-4-6 Concluding Remarks Low-Fidelity Results . . . 56
4-5 High-Fidelity Results: QBlade & SOWFA Simulations . . . 56
4-5-1 QBlade Results . . . 57
4-5-2 SOWFA Results . . . 59
4-6 Summary Results Wind Turbine Simulations . . . 61

**5 Stability Analysis 65**
5-1 Boundedness Properties and Asymptotic Stability . . . 65
5-1-1 Boundedness and Stability of KF Dynamics . . . 66
5-1-2 Boundedness and Stability of RLS Dynamics . . . 67
5-2 Stability of the Phase Convergence . . . 69
5-3 Note on Robust Stability and Performance . . . 71

**6 Conclusions and Recommendations** **73**
6-1 Conclusions . . . . . 73
6-2 Recommendations . . . . . 75

**A Mathematical Derivations** **77**
A-1 Using a DC-offset for Phase Estimation . . . . . 77
A-2 Bound on $\Delta\phi$ . . . . . 78
A-3 Equilibrium Points Phase Convergence . . . . . 79

**B MBC Transformation Second-Order System** **81**

**C OpenFAST & QBlade Results** **83**
C-1 OpenFAST: Synchronization . . . . . 83
C-2 QBlade: Synchronization . . . . . 84

**Glossary** **91**
List of Acronyms . . . . . 91

# List of Figures


1-1 Actuator disc model schematic. $\mathbf{U}$ represented the wind velocity perpendicular to the actuator disc. The actuator disc area is denoted by $\mathbf{A}$. . . . . 1

1-2 Power and thrust curve of *IEA 15-MW* reference turbine. The control regions are indicated with vertical solid gray lines. . . . . 2

1-3 Illustration of Large Eddy Simulations (LES) study for different wake mixing strategies. **Left:** stable normal wake with baseline control. **Middle:** dynamic induction control, or pulse method, with periodically shedding vortex ring. **Right:** wake resulting from the helix approach. The darker blue indicates an iso-surface for a specific wind velocity, while the lighter blue is the absolute wind velocity. The distance between turbines is scaled by the rotor diameter $D$. . . . . 5

1-4 The Power Spectral Density (PSD) of the Blade Out-of-Plane (BOoP) bending moments (**left**) and tower bending moments (**right**) for different wake mixing strategies of T2. Results are for the *NREL 5-MW* reference turbine for a wind speed of $8$ m/s and Turbulence Intensity (TI) of $5\%$. The results are filtered by a moving average filter. Red circles indicate the detected pitch frequencies of T1 for the Clockwise (CW) and Counter-Clockwise (CCW) helix strategies. . . . . 7

2-1 **Left**: relationships between different frames of reference described by the Park/Multi-Blade Coordinate (MBC) ($T_p$) and Clarke transformations ($T_c$). The arrows denote forward transformations. **Right**: rotating (R) and Non-rotating (NR) reference frames for a wind turbine in Cartesian $XYZ$-coordinates. The azimuth angle of the $b$-th blade is given by $\psi_b$. $M_{1,R}$ denotes a rotating component of the first blade. The green arrows are the projections of this component on the $y$- and $z$-axes. 10

2-2 Time-domain interpretation of Clarke and Park transformations for three-phase signals. The top row shows $\alpha\beta 0$ and $dq0$ signals from a single frequency $abc$ framework with a small phase offset on top of their phase shifts. The bottom row shows the same effect, although a second frequency with a different amplitude is added to the signal. . . . . 12

2-3 Schematic representation of the use of the MBC transformation to achieve periodic yaw and tilt moments on the turbine rotor. Here, $\theta_{tilt}$, $\theta_{yaw}$, and $\theta_{1,2,3}$ are the tilt, yaw, and individual pitch angles respectively. The rotor azimuth angle is given by $\psi$. $M_{tilt}$, $M_{yaw}$, and $M_i$ are the tilt, yaw, and individual blade bending moments respectively. Finally, $f_e$, $f_r$, and $f_\theta$ are the excitation, rotor, and pitch frequencies for a CCW helix method respectively. . . . . 12

2-4 Turbine layout and control methods of three cases for a 5D separated two-turbine scenario. Case 1 has an upstream turbine (T1) performing the helix method while a downstream turbine (T2) runs a baseline controller. Case 2 only contains T2 and experiences a steady wind inflow. For Case 3, both T1 and T2 perform the helix method. T1 always experiences a below-rated steady wind inflow coming from the left of the figure. . . . . 14

2-5 Simulation of cases from Figure 2-4 showing tilt and yaw blade bending moments of the downstream turbine T2. Simulations are performed in OpenFAST for an *NREL 5-MW* reference turbine experiencing and/or performing a CCW helix. For the bottom-right simulation, Case 3 is shown as well in dashed lines. The data is filtered using a low-pass filter leaving the excitation frequency $\omega_e$ and Direct Current (DC)-offsets. The unfiltered data is shown in gray. . . . . 14

2-6 Welch power spectra for three different reference frames of the blade bending moments. **Top:** power spectra estimates of individual blade bending moments. The Once-per-Revolution (1P) and $1P + f_e$ frequencies are shown with the dashed lines. **Middle:** this spectrum shows the tilt and yaw bending moments from a $T_p(\psi)$ transformation. **Bottom:** power spectra of resultant tilt and yaw moments from a $T_p(\psi + \omega_e t)$ transformation. The shifted versions of $1P + f_e$ and 1P frequencies are denoted by dashed lines as well. . . . . 16

2-7 Example interference output and scaled amplitudes of resulting interference. **Left:** visual representation of the computation of peak amplitudes $c$. For each combination amplitudes of interfering signals $a$ and $b$, the peak value is computed over over $\theta_a = 0$, $\theta_b \in [0, \pi]$. The resulting set of blue points forms the basis of the blue lines presented on the right. **Right:** the peak values are scaled for all $\{a, b\}$ such that minimum interference equals $\Sigma_{ab}(\Delta\phi) = 0$ and maximum interference equals $\Sigma_{ab}(\Delta\phi) = 1$. The red line indicates $\Sigma^{-}_{ab}(\Delta\phi)$, which is the smallest possible line in this set. The horizontal dashed and vertical solid lines represent points on $\Sigma^{-}_{ab}(\Delta\phi)$ for which a certain level of interference is achieved. . . . . 19

2-8 Proposed controller diagram for helix wake synchronization via an Recursive Least Squares (RLS) estimator in a downstream turbine. The wake is modeled as an input to the wind turbine system with a periodic component $V_k^{\mathrm{p}}$ and known frequency $\omega_e$. A summation of the Park and Clarke transformed output $y_k$ is used as input to the square-root RLS estimator. The resulting estimate is filtered through a low-pass filter, after which the phase $\phi$ is computed. To correct for coupling and actuator delays, the optimal azimuth offset $\psi_0$ is added before the phase estimate is used for employing the helix method. . . . . 25

2-9 Controller diagram for helix wake synchronization via a Kalman Filter (KF)-based estimator in a downstream turbine. The wake is modeled as a disturbance on the control input, containing a periodic component $u_k^{\mathrm{p}}$ and known frequency $\omega_e$. A load disturbance $w_k$ is also considered to be added. The output $y_k$ contains measurement noise $v_k$ and is used together with the control input $u_k^{\mathrm{c}}$ to the Kalman filter. The estimated disturbance states are rotated using a $T_{dq}(\omega_e t)$ transformation. The phase of the helical disturbance $\theta_a$ is computed via the inverse tangent of this estimate. This phase can directly be used for synchronization with the wake. 28

3-1 Permanent Magnet Synchronous Machine (PMSM) controller diagram. The system takes in the input $u_k$ which consists of the controllable and uncontrollable inputs $u_k^{\mathrm{c}}$ and $u_k^{\mathrm{u}}$ respectively. The uncontrollable input contains the periodic disturbance $u_k^{\mathrm{p}}$ and the noise $w_k$. Both the controllable input and the periodic disturbance have frequency $\omega_e$ with amplitude and phase $a_c$ and $\hat{\phi}$ or $a_d$ and $\theta_a$ respectively. Measurement noise $v_k$ is added to the output $y_k$. Both the RLS- and KF-based estimators use this output to compute $\hat{\phi}$. The RLS estimator takes in an azimuth offset $\psi_0$ to correct for actuator delays. The switch determines which estimate is used for the synchronization. . . . . 33

3-2 Example results of PMSM phase synchronization. **Left:** time domain result of a KF-based synchronization. The output is denoted by $y$ and $y_d$ represents the signal the output should be synchronized with. **Middle:** time domain result of the estimated phase for three different methods. The different controllers start synchronizing with the Ground Truth (GT) after $T = 200$ seconds. **Right:** Welch power spectrum estimate of the phase estimate result presented in the middle. Two peaks are visible at $\omega_e + \omega_{m0}$, which is the first harmonic of the RLS estimates. 34

3-3 Time-domain simulation results of a step reference and a pulse disturbance. **Left:** step reference of $+10^\circ$ starting at $T = 400$ s for both controllers. **Right:** pulse disturbance of $+30^\circ$ also starting at $T = 400$. The red dashed line indicated the point where the controllers are switched on. The black dashed line represents the ground truth phase. . . . . 35

3-4 Time-domain results for two experiments with different Signal-to-Noise Ratio (SNR)s due to added noise. **Left:** Output $I_{\mathrm{d}}$ of both controllers and experiments. $\mathrm{KF1}$ and $\mathrm{RLS1}$ represent the case where the amplitude of $u_k^{\mathrm{p}}$ equals $1.5^\circ$. Likewise, $\mathrm{KF2}$ and $\mathrm{RLS2}$ are the cases for which the amplitude equals $0.5^\circ$. Both signals are shown without noise and the original data is shown in gray. The signal $y_{\mathrm{d}}^{\mathrm{p}}$ is the part of the output caused by the periodic disturbance only. Hence, it represents the signal the controller should synchronize with. The mean SNR is depicted in the top right corner of each figure. **Right:** Phase estimates for each case over a time period of $1200$ seconds. The ground truth is denoted with a dashed black line. 37

3-5 Time-domain simulation results of partial and complete out-of-phase synchronization. **Left:** Partially out-of-phase synchronization by setting $\theta_b = \theta_a - \frac{\pi}{2}$ starting at $T = 400$ s for both controllers. **Right:** Completely out-of-phase synchronization by setting $\theta_b = \theta_a - \pi$ starting at $T = 400$ s. The red dashed line indicated the point where the controllers are switched on. The black dashed line represents the ground truth phase. At $T = 400$ a pulse disturbance is added of $+10^\circ$ for both experiments. . . . . 38

4-1 Bode magnitude diagrams of the MBC-transformed linearized *NREL 5-MW* system $G(s)$. This multivariate transfer function maps the tilt and yaw pitch angles, $\theta_{\mathrm{tilt}}$ and $\theta_{\mathrm{yaw}}$ respectively, to the tilt and yaw blade bending moments, $M_{\mathrm{tilt}}$ and $M_{\mathrm{yaw}}$. Different linearizations are shown for operating points ranging from $5$ to $9$ m/s wind speeds. The excitation frequencies $f_e$ of the upstream turbine are indicated by the vertical dashed lines for an ambient wind speed of $U_\infty = 9$ m/s and Strouhal numbers $St = 0.25$ (blue) and $St = 0.4$ (red). . . . . 42

4-2 Rotating disc data sets with different initial phases. The ambient wind speed is set to $9$ m/s and the velocity deficit area has a wind speed of $4.5$ m/s. The hub height is at $90$ meters and indicated with the red cross. The red circle represents the rotor diameter of the *NREL 5-MW* turbine. The point $Y = 0$ is located in the center of the x-axis. Similarly, $Z$ has a total length of $255.6$ meter but starts at $4.8$ meter. . . . . 44

4-3 Wind field volume extracted from SOWFA data and four cross-sections at different turbine distances. **Left:** three-dimensional iso-surface of a wind field produced by a *DTU 10-MW* turbine performing the helix method. The darker blue shading indicates a wind velocity in the $X$-direction of 7 m/s. On the $XY$-plane, the absolute wind velocity is plotted in lighter blue. Further down the wake, it can be seen that the structure rotates counterclockwise. The data is simulated in SOWFA. An upstream turbine is placed at $0D$ to give an indication of the scale. The dashed boxes represent $X$ locations of the different cross-sections. **Right:** four example cross-sections at different rotor distances. The color of the boundary matches the cross-sections shown on the left. The cross-sections have the same dimensions as the wind fields shown in Figure 4-2. The pixel colors indicate the wind speed in the $X$-direction. . . . . 46

4-4 Time and frequency domain results for the rotating disc wind profiles in the *NREL 5-MW* reference turbine. **Left:** phase estimates from the RLS- (solid) and KF-based (dashes) estimators for 10 minutes of simulation time. The color indicates the same data set, but $90^\circ$ in phase apart. RLS and KF estimates are separated by the optimal azimuth offset, which is $\psi_0 \approx 11^\circ$ of phase. **Right:** Welch power spectrum estimate of the $+0^\circ$ data set for the RLS- and KF-based estimators. The magnitude is shown in degrees. . . . . 50

4-5 Power generation of a *NREL 5-MW* reference turbine employing helix wake synchronization with an incoming helical wake at different turbine distances. **Top:** percentage power generation w.r.t. a Baseline (BL) case for different Strouhal numbers ($St$). A net $0\%$ increase is indicated by the dashed black line. **Bottom:** Amplitudes of tilt and yaw blade bending moments of BL turbine at the excitation frequency for each turbine distance. The blue data represents an excitation frequency with $St = 0.25$ and the red data is for $St = 0.4$. . . . . 52

4-6 Average power generation of two helix wake synchronization controllers w.r.t. a BL case for different pitch amplitudes at $4D$. The RLS-based controller is indicated with blue and the KF-based controller with red. A net $0\%$ increase is indicated by the dashed black line. . . . . 53

4-7 Comparison of tilt and yaw blade bending moments of three different control strategies for two different helical inflows. The control methods consist of a baseline controller (blue), a regular helix method (green), and an RLS-based synchronized helix method (red). Both helix methods are CCW with an amplitude of $2^\circ$. The data is post-processed by using a zero-phase digital low-pass filter. The unfiltered data is shown in gray. The dashed line at $T = 200$ seconds indicates the individual pitch control for the helix method being turned on. . . . . 54

4-8 Time- and frequency-domain results of the tilt and yaw blade bending moments for helix wake rejection. **Left:** Time-domain simulation for the three different rejection cases. The data is post-processed by using a zero-phase digital low-pass filter. The unfiltered data in gray represents the bending moments of a baseline case. The dashed red line indicated the start of the rejection. **Right:** Welch power spectra estimates of the bending moments. The dashed blue line indicates the excitation frequency. The top row consists of the tilting moment $M_{\text{tilt}}$ and the bottom row represents the yaw moment $M_{\text{yaw}}$. . . . . 55

4-9 Time- and frequency-domain results for helix wake synchronization in QBlade for steady wind conditions. **Left:** phase estimates of the RLS filter in T2 for four different initial helix phases of T1. The solid lines represent the estimates under synchronization, while the dashed lines represent the baseline cases. The vertical red dashed line indicated the start of the synchronization. **Right:** Welch power spectrum estimate for tilt blade bending moment in T2. Both the synchronized and baseline case are shown. The red dashed line indicates the excitation frequency $f_e$. . . . . 57

4-10 Results for the QBlade simulations with turbulent wind conditions. Both cases have a turbulence intensity of $TI = 5\%$, but each with a different boundary layer exponent $\alpha$. **Left:** Welch power spectra estimates of tilt and yaw blade bending moments in T2. For both cases, the BL and synchronized (Sync) turbines are displayed. The red dashed line indicated the excitation frequency $f_e$. **Top right:** comparison of the different boundary layers. It can be seen that the Power Law (PL) with exponent $\alpha = 0.08$ of case 1 roughly fits the log law (LL) with roughness length $l_0 = 2 \cdot 10^{-4}$. **Bottom right:** difference in power generation between synchronized and baseline downstream turbines $\Delta$P. The mean power generation over a period of 1200 seconds for both cases is denoted by $\bar{\text{P}}$. . . . . 58

4-11 RLS estimates of the helix phase in T2 for all eight SOWFA sets. The phase is estimated in post, as the data was not available during post-processing. The mean phase of the BL case is indicated with the black dashed line. Likewise, $-90°$ and $-180°$ differences with this mean are shown by the red and blue dashed lines respectively. . . . . 59

4-12 Generated power of the SOWFA simulations for T2 and T3. **Top:** power generation of T2 over time. **Bottom:** power generation of T3. The black dashed lines represent the mean power of both the T2 and T3 BL cases. . . . . 60

4-13 Tilt blade bending moments of T2 for SOWFA data sets. The moments are filtered using a zero-phase digital low-pass filter. The original data is shown in gray. A zoomed-in region is displayed on the right to better show the filtered data. The dark gray dashed rectangle indicates this. The vertical dashed lines are the times where the estimated phase crossed the horizontal lines in Figure 4-11. . . 61

5-1 Purely real-valued part of $\Delta\bar{\phi}$ for the ration $b/a$ and azimuth error $\Delta\psi_0$. $\Delta\bar{\phi}$ represents the part of the equilibrium point that is independent of $\theta_a$ and is equal to $-\arcsin\left(-\frac{b}{a}\sin(\Delta\psi_0)\right)$, with $a$ and $b$ being the amplitudes of the helical wake and helix actuation respectively. Both are assumed to be the blade bending moments in a $dq$ reference framework at the excitation frequency $\omega_e$. The area inside and below the dashed red line indicates the region of convergence (ROC) for which pairs of $b/a$ and $\Delta\psi_0$ will converge to a stable equilibrium point. All the points outside this area are unstable. The area inside and underneath the blue dashed line represents all $\left|\Delta\bar{\phi}\right| \leq 10°$ which would result in a minimum of $99.2\%$ of the attainable interference with the helical wake. . . . . 70

C-1 Time domain simulation results of power and load related signals for a baseline, Helix, and synchronized Helix controller in OpenFAST. The data corresponds to the synchronization experiment from Section 4-4-4. . . . . 83

C-2 Time domain simulation results of power and load related signals for a baseline, Helix, and synchronized Helix controller in QBlade. The data corresponds to the synchronization experiment with low TI and boundary layer with $\alpha = 0.08$ from Figure 4-10. . . . . 84

# List of Tables


3-1 PMSM model parameters. . . . . 32

4-1 Specifications of the *NREL 5-MW* reference turbine. . . . . 40

4-2 Estimated optimal azimuth offsets $\psi_0$ for Strouhal numbers $St = 0.25$ and $St = 0.4$. The offset is chosen as the $\psi_0 = -\psi_d$ via Equation 2-10, where $\psi_d$ is the phase lag at the excitation frequency. . . . . 43

4-3 QBlade wake and vortex numerical simulation settings used for T1. The length of wake zone 3 is chosen to be small, as here, we are less interested in the dynamics of the far wake. . . . . 48

4-4 SOWFA three-turbine setup simulation sets. All turbines run a $k\omega_g^2$ torque controller as well. The synchronized helix utilizes the RLS-based estimator. . . . . 49

4-5 SOWFA mean power generation results for T2 and T3. The percentages are given with respect to the baseline case of the same turbine row. Both the power and percentages are rounded upward. . . . . 62

4-6 Comparison between OpenFAST and QBlade results. . . . . 63

# Acknowledgements

I would like to thank my thesis supervisor, ir. Mees van Vondelen, for his invaluable guidance and support during my thesis project. His insightful feedback on my ideas and constructive criticism of my work was essential to the completion of this thesis. Mees, thank you for the many hours you took to answer all my questions and for the regular meetings where you shared your expertise. It was a pleasure collaborating with you on your paper and conducting wind tunnel experiments together. Thank you for everything you have done, and I wish you the best of luck in all your future work and research.

Secondly, I would like to express my gratitude to prof. dr. ir. Jan-Willem van Wingerden for his support throughout my thesis project. Under your supervision, I learned a lot about wind farm control and had the opportunity to witness the innovative ideas being pursued by your research team. I would also like to thank you for your contribution to the end result of this project, as the SOWFA simulations would not have been possible without your help.

Additionally, I would like to thank ir. Rogier Dinkla for his advice during our monthly meetings and his feedback on this final document. I found his perceptive remarks to be particularly helpful, and I am grateful for the time and effort he invested in providing me with such valuable feedback.

A special thanks to ir. Daniel van den Berg, who has spent a considerable amount of time helping me out with QBlade. After my midterm presentation, Daniel came up with the idea to test the helix wake synchronization in QBlade. This turned out to be a really good call, as it pushed the project forward and gave a lot of new insights. I also had the pleasure to work together with Daniel as a teaching assistant for the Robust Control course.

Finally, I would like to thank my family and friends for their continued support throughout my thesis. Especially my roommates from the OIP, for providing me with the necessary fun besides the many hours I spent working with MATLAB.

Delft, University of Technology — J. Ottenheym
March 24, 2023

# Chapter 1

# Introduction

## 1-1 Wind Turbines

Wind turbines are defined as machines that convert the kinetic energy of wind into electrical energy. There are different types of wind turbines, such as turbines with vertical or horizontal axis, and they can have different numbers of blades. The most common are the three-bladed upwind horizontal axis wind turbines (HAWT). The rotor is connected to a generator via a drivetrain in the nacelle. This rotor-nacelle assembly is supported by the tower, which rests on a fixed foundation or floating structure. The momentum of the wind passing through the rotor plane is converted into aerodynamic forces that cause the rotor to rotate. One model that describes this process is the actuator disc model [1, Chapter 3]. This model analyzes a stream tube flowing through a fictive disk representing the area swept by the rotor. A schematic representation of this process can be seen in Figure 1-1. Here it can be seen that

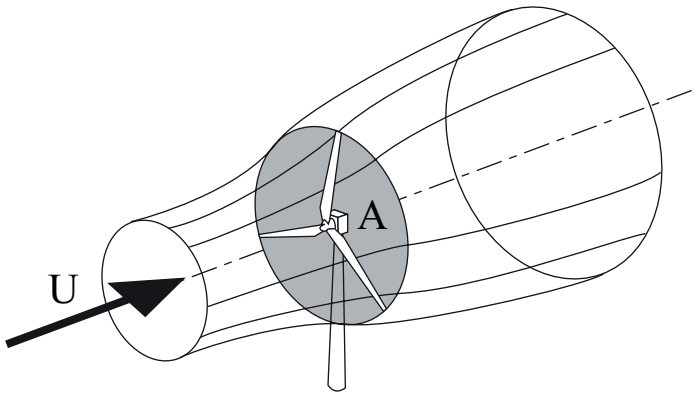



**Figure 1-1:** Actuator disc model schematic. **U** represented the wind velocity perpendicular to the actuator disc. The actuator disc area is denoted by **A**. Figure adapted from [2].

the cross-section of this stream tube is smaller upstream than downstream. This is due to the fact that the mass flow rate of the wind through the tube must remain constant and the

air is effectively incompressible at these speeds [1, Chapter 3]. As the wind velocity decreases downstream, the area of the cross-section must increase. The available power depends on the wind velocity cubed, so siting wind turbines in locations with high wind speeds is advantageous for power generation. However, the theoretical limit of steady-state energy extraction is given by the Betz limit [3], which is about 59%. To achieve this optimal power extraction ratio, the controller has to maximize its power coefficient $C_P$. This is given as the ratio between the power generated and the power available. The power coefficient is a dimensionless function of the control variables. The most common control variables are given by:

- **Generator torque ($\tau_g$).** Torque control is used to maintain an optimal Tip-Speed Ratio (TSR) ($\lambda$), which maximizes power production.
- **Blade pitch angle ($\beta$).** Pitch control can be used to rotate the blades. It can, therefore, be used to influence power production or reduce loads.
- **Yaw angle ($\gamma$).** Yaw control is used to align the rotor plane perpendicular to the wind inflow.

The tip-speed ratio is defined as the ratio between the wind velocity and the velocity of the blade tips. Therefore, a wind turbine has different operating regions depending on the wind speed. The ideal power and thrust curves for the *IEA 15-MW* offshore reference turbine [4] are shown in Figure 1-2. The operating regions are shown here as well. Region 1.5 starts at the cut-in wind speed. This is the minimum wind speed at which the turbine can deliver power. The TSR starts out high, and as the wind speed increases, the TSR decreases toward the optimal TSR. In Region 2, the goal is to maximize power by tracking the optimal TSR. Region 3 starts at the rated wind speed, above which power is held constant. As the wind speed increases above the rated wind speed, less thrust is required to keep the turbine producing its rated power. Thus, the goal is to keep the generator torque constant, limit power generation, and reject loads. Region 3 ends at a maximum set wind speed. Here, the turbine is shut down for safety reasons. Other regions are start-up ( Region 1), transition region 2.5, and shutdown of the machine.

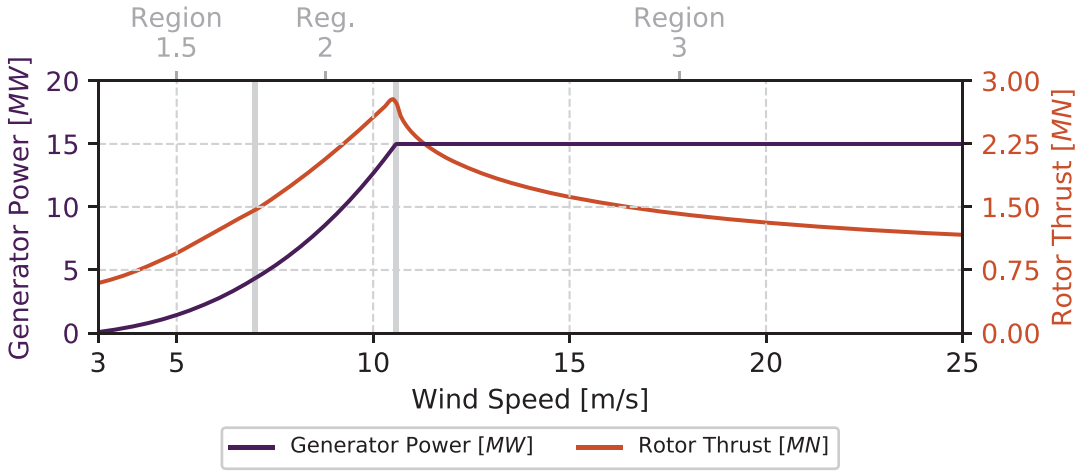



**Figure 1-2:** Power and thrust curve of *IEA 15-MW* reference turbine. The control regions are indicated with vertical solid gray lines. Figure adapted from [4].

### 1-1-1 Turbine Wake

As depicted in Figure 1-1, the cross-section of the stream tube behind the wind turbine increases because of the decrease in wind velocity. This region behind the turbine where the flow is changed is called the turbine *wake*. The increase in cross-section is called wake expansion and the decrease in wind speed is the wind velocity deficit. Besides those, the wake has more characteristics [1, Chapter 9]. The turbulence intensity is increased because of the blade's rotation, generating vorticity at the blade tips. This results in increased structural loads in the downstream turbine [5], [6]. The wake experiences meandering due to horizontal and vertical oscillations in the entire wake structure [7]. Vertical wind shear causes the wake properties to change with height because of a boundary layer in the wind speed with the ground. The turbine itself can further influence the wake by yawing out of the incoming wind flow, or via yaw or tilt moment-induced pitching of the blades [8]. Finally, wake recovery is the phenomenon where the wind speed in the wake returns to the free-stream velocity due to mixing with the ambient air. The wind condition and the turbine design itself determine when wake recovery takes place. The distance at which this happens is usually larger than multiple rotor diameters.

## 1-2 Wind Farm Control

As wind turbine wakes propagate far downwind, other wind turbines in wind farms can be affected by them under certain wind directions [9]. It is common to control turbines individually in wind farms. This is called greedy control, where each turbine aims to reach its optimal performance [1, Chapter 9]. As a result, downstream *waked* turbines will experience reduced power production and increased fatigue loads [5]. By following a greedy control strategy, a wind farm will, therefore, reach sub-optimal behavior. The distance at which wake recovery takes place is usually much larger than the distance between turbines in a wind farm, as placing turbines close together reduces costs [10]. These expenses all contribute to the Levelized Cost of Energy (LCoE) among other factors. The LCoE also depends on the power production of the wind farm. The effect of turbine wake on power production is different per wind farm due to turbine layout, turbine design, and wind conditions. However, it is estimated that average power losses due to turbine wakes are in the order of 10 to 20% of the total power output in large offshore wind farms [9]. For some wind directions, this loss can be as high as 40 to 60% of the total power. In addition to reduced power generation, the fatigue load is estimated to increase by 5 to 15% [5]. This leads to a further reduction in LCoE as maintenance costs increase. Therefore, wind farm control is referred to as one of the major challenges in wind energy science [11]. To achieve optimal control in a wind farm, other turbines, and the wake effect have to be considered.

### 1-2-1 Wake Control Strategies

The literature distinguishes three different categories of control strategies for wake control: Axial Induction Control (AIC), wake redirection control, wake steering, and wake mixing control. All these techniques may involve operating the wind turbines at sub-optimal settings for the individual turbine but increasing the overall performance of the wind farm.

In AIC, the upstream turbine is derated to reduce the wind velocity deficit. This can be accomplished by pitching the rotor blades or changing the generator torque. When the farm level energy capture increases by derating the upstream turbine, AIC is effective. However, reducing the thrust force of the upstream turbine also means reducing wake turbulence and thus wake recovery [12]. The latter reduces the wind velocity further downstream, which is generally counter to the derating of the upstream turbine. Whether AIC contributes to increased power generation is still debatable. Field tests show that the energy benefit of axial induction control is minimal [13]. Nevertheless, it could be an interesting candidate for minimizing loads within a wind farm [14].

The goal of wake redirection control is to deflect the wake via misalignment of the upstream wind turbine with respect to the wind inflow. As every action has an equal and opposite reaction, the wake initially propagates under an angle as well. This causes the wake to partially or not overlap with the downstream turbine. Wake deflection can be done by yawing or tilting the turbine [8]. In the literature, wake deflection through yaw misalignment is commonly referred to as wake steering. This is an active field of research that has been tested in the field several times [15]–[17]. The first commercial products that use yaw misalignment to steer wakes are currently already on the market [18]. Tilting the rotor up or down can also be used for wake steering. This is, however, not a common degree of freedom. Individual Pitch Control (IPC) can also be used to induce deflection of the wake. The individual control of the pitching angles of the blades can generate a directional moment on the rotor. If this directional moment is pointing away from the axis of rotation of the rotor, the wake will be deflected in the opposite direction. However, using IPC for wake deflection results in higher loads on the blades and the blade pitch bearings [8]. Wake mixing control aims to increase the mixing of the wake with ambient free-stream velocity air, such that the wake can recover energy. This phenomenon was explained in Section 1-1-1 as wake recovery. However, in wake mixing, the wake does not necessarily fully recover. A strategy using a varying thrust force was first introduced in [19]. Here, they implemented a receding horizon control approach to maximize the wind farm energy by finding the optimal thrust force set-point. Later, sinusoidal set-point signals for the thrust force were used in [20]. As a result, wake mixing was enhanced through the periodic shedding of vortex rings behind the upstream turbine. This method is called Dynamic Induction Control (DIC) and was later named the pulse method. This method proved to be more practical than the work of [19], due to the significant decrease in computational costs and was also shown to improve energy extraction experimentally in [21].

This strategy inspired the work of [22], where IPC was used to generate phase-shifted sinusoidal reference signals for each blade. This induces a helical shape in the wake, similar to the pulse method, which improves wake mixing for downstream turbines. The helix approach uses the Multi-Blade Coordinate (MBC) transformation [23] to follow the phase-shifted sinusoidal reference. These sinusoidal signals oscillate at a frequency of $f_e$, which is defined as the *excitation frequency*. The MBC transformation uses the azimuth angle of the rotor to transition from the rotating frame of the rotor to a non-rotating frame. This transformation is explained in more detail in Chapter 2. In Figure 1-3, the differences in wake mixing between the baseline control, the pulse method, and the helix approach are visualized for a two-turbine setup with laminar flow. The average power generation per wind turbine is also shown, illustrating the potential of wake mixing. However, pitch actuation and a varying rotor thrust reduce turbine life expectancy due to increased loads [24]. Although dynamic wake mixing strategies have great potential, the additional loads must be reduced before they

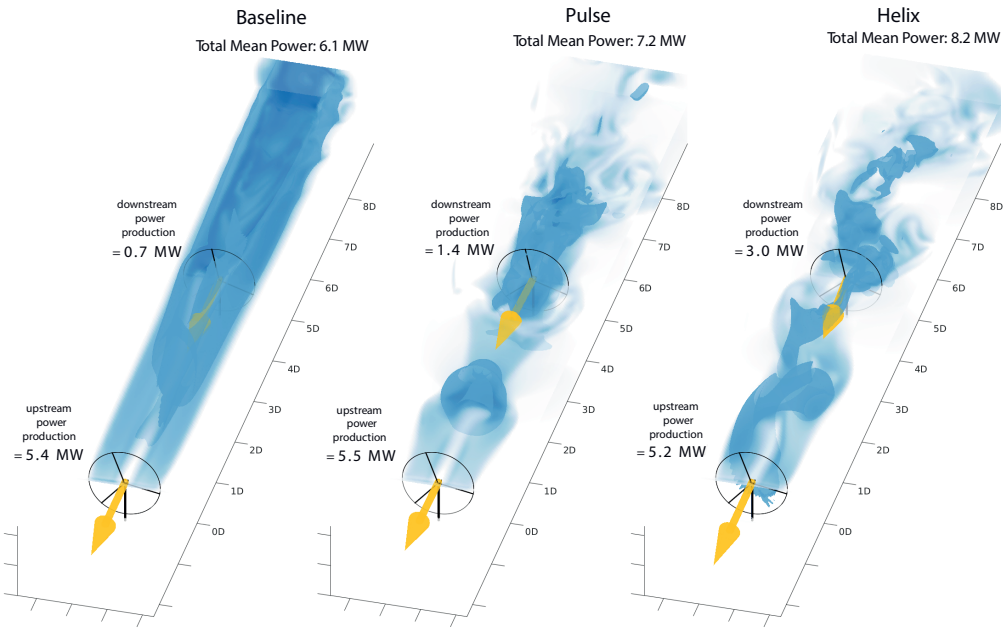



**Figure 1-3:** Illustration of Large Eddy Simulations (LES) study for different wake mixing strategies. **Left:** stable normal wake with baseline control. **Middle:** dynamic induction control, or pulse method, with periodically shedding vortex ring. **Right:** wake resulting from the helix approach. The darker blue indicates an iso-surface for a specific wind velocity, while the lighter blue is the absolute wind velocity. The distance between turbines is scaled by the rotor diameter $D$. Figure adapted from [11].

can be deployed in the field. Alternatively, wake mixing control and their dynamics should be incorporated into wind turbine design to strengthen the most affected components. The following sections address the load impact of dynamic wake mixing strategies and discuss possible solutions to mitigate these loads.

### 1-2-2 Load Impact of Dynamic Wind Farm Wake Mixing Strategies

Wake mixing control strategies, such as the helix approach, seek to maximize wind farm power generation. Compared to the pulse method, a study has shown that in simulation the helix approach results in lower Damage Equivalent Load (DEL) [24]. The different load impacts that were analyzed are the structural loads on the tower, the blade bending moments, as well as the impact on the blade pitch-bearing damage risk. In [24], the structural loads of dynamic wake mixing strategies were compared and analyzed for varying wind speeds and with low and high Turbulence Intensity (TI). Wake mixing strategies are considered to be more effective for wind speeds below the rated regime. This is because above rated, the power losses of downstream turbines are significantly lower. Therefore, the focus will be on the structural loads in this regime, as this should be more relevant. In OpenFAST, a simulation tool for wind turbines, the authors of [24] have shown that both DIC and the helix result in a significant increase in blade DELs compared to a baseline controller. In addition, DIC also shows a significant increase in tower DEL. It is hypothesized that the increased loading on

the blades is caused by the increased pitch actuation. The effect of the helix on the fatigue loads of the downstream turbines is smaller compared to the upstream turbines.

Blade pitch oscillations as induced by methods such as IPC and the helix method were assumed to increase the risk of severe damage to the blade pitch bearings. Later, a study contradicted this result [25] and showed that this risk is only increased for very small blade pitch movement ($< 0.7°$). Both DIC and the helix approach operate at a set-point pitch amplitude (e.g. $2.5°$ or $4°$). It is therefore hypothesized in [24] that the stress on the blade pitch bearings is spread out over a large enough area within the bearing. This would reduce the risk of severe surface-induced damage (SID) of the bearings [26]. However, lowering the pitch actuation to decrease blade bending moments could result in a smaller pitch amplitude. Note that the blade pitch angle also has an upper limit. This upper limit is where the lift coefficient drops due to blade stall. Furthermore, the pitch actuation can be decreased by lowering the pitching frequency $f_\theta$. For a Counter-Clockwise (CCW) rotating helix, this frequency is defined as $f_\theta = f_e + f_r$, where $f_r$ is the rotor frequency. As mentioned, the helix operates at an excitation frequency $f_e$. In [22] the optimal $f_e$ was chosen experimentally and confirmed by analyzing average wake velocities behind a turbine at different distances. The excitation frequency can be characterized in terms of the dimensionless Strouhal number $St$, which is given by

$$St = \frac{f_e D}{U_\infty}, \tag{1-1}$$

where $U_\infty$ denotes the ambient wind speed in meters per second and $D$ the rotor diameter in meters. Compared to a baseline greedy controller, the Strouhal number around $St = 0.25$ was found to give good results for DIC. The optimal Strouhal number and pitch amplitude for the helix approach have yet to be found. In [27], it was observed that $St = 0.4$ was more effective for the helix approach. Lowering the pitch actuation, while keeping the pitch angle large enough by lowering the pitching frequency $f_\theta$, can therefore result in a sub-optimal Strouhal number. This in turn results in a lower total wind farm power production.

Overall, there lies a challenge in finding the optimal operating point for the helix approach to increase WF power production while minimizing different loads. On top of that, this optimal point might vary for different wind speeds and turbulence intensities. Extending the helix approach to a control strategy that can cope with different load constraints could, therefore, be useful. Improving the interaction of multiple turbines operating with the helix approach also remains unexplored. This applies both to increasing the total energy production and to minimizing fatigue loads. In the following section, these possibilities will be further discussed.

## 1-3 Problem Formulation and Research Outline

As was discussed in Section 1-2-2, pitch actuation can be decreased by lowering the pitch amplitude or pitching frequency. This could potentially have a negative effect on the loads or wake mixing respectively. Alternatively, load reduction objectives can be shifted towards the downstream turbine. At the beginning of this section, it was mentioned that pitch actuation is needed to implement dynamic wake mixing. Significant gains in power production or load reduction could, therefore, be minimal when load constraints are incorporated.

In [24], the Power Spectral Density (PSD) of the Blade Out-of-Plane (BOoP) bending moments of the downstream turbine shows that the excitation frequency and the blade pitch

frequency of the upstream turbine are present. Figure 1-4 shows this result for the Clockwise (CW) and CCW helix, indicated by the red circles. This suggests that a control strategy could amplify these frequencies while reducing the Once-per-Revolution (1P) frequency amplitude. In turn, this could lead to the downstream turbine performing the same helix method as the upstream turbine, while less pitch actuation is required. Currently, there is a research gap in the application of the helix approach on the downstream turbine. Although it was shown that the power production of the downstream turbine increased [22] and that the load effect downstream was minimal [24], no research has been conducted on the downstream turbine operating *with* the helix approach. When multiple downstream turbines are in each other's wake, multiple turbines also need to implement the helix approach. This has to be done in a coordinated fashion, as a turbine might need to be in phase with the incoming helical wake to achieve the amplification of the bending moments. Otherwise, wake mixing further downstream might be sub-optimal and could potentially lead to increased loads. Amplifying

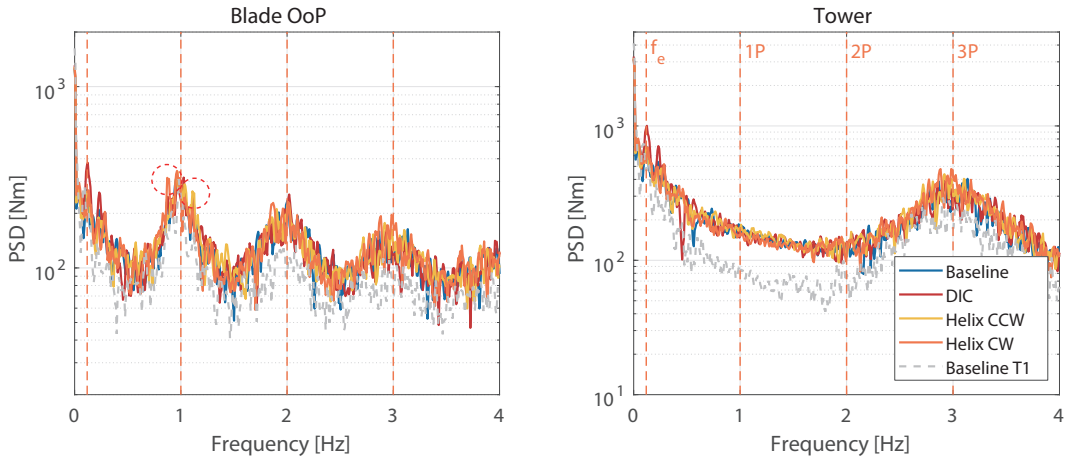



**Figure 1-4:** The PSD of the BOoP bending moments (**left**) and tower bending moments (**right**) for different wake mixing strategies of T2. Results are for the *NREL 5-MW* reference turbine for a wind speed of $8$ m/s and TI of $5\%$. The results are filtered by a moving average filter. Red circles indicate the detected pitch frequencies of T1 for the CW and CCW helix strategies. Figure adapted from [24] and modified by adding the red circles.

the blade bending moments caused by an incoming helical wake in a downstream turbine to initialize the helix method, is the main idea that will be pursued in this thesis.

### 1-3-1 Research Questions

The previous section built upon the core problem of the wake effect in wind farms and highlighted several challenges within the potential solution of wake mixing strategies. From the literature, it is clear that increased loads, due to more pitch actuation, have to be accounted for in future wake mixing applications. Eventually, an optimal wind farm level controller needs to be designed to determine when to turn on a wake mixing strategy, such as the helix. Finally, more research needs to be conducted on wake mixing strategies for downstream turbines. This master thesis will be focused on the effect of a helix wake from the upstream turbine on a downstream turbine, and how it can benefit from the incoming wake.

It is the hypothesis of this thesis that the helix method can be initiated with less pitch actuation in a downstream turbine via synchronization with an incoming helical wake. The main research question of this thesis is, therefore, formulated as:

*How can the wake of an upstream turbine employing the helix method be used to the benefit of a downstream turbine using control?*

---

In support of this main research question, three sub-questions have been formulated. The results presented in Figure 1-4 from [24] show that the incoming helical wake can be measured in a downstream turbine. The first question here, therefore, is about how these signals can be extracted and used to synchronize with this incoming wake. The second and third questions consider the implications of different kinds of synchronization. As amplification could be achieved by in-phase synchronization, out-of-phase synchronization could lead to the rejection of the helical wake. The questions are thus defined as follows:

1. *To what extent can the helix method be initiated in a downstream turbine by using the excitation frequency of the incoming helix wake?*
2. *What is the effect of amplifying the helix wake via synchronization on the power production of a waked downstream turbine?*
3. *What is the effect of rejecting the helix wake via synchronization on the power production of a multi-turbine setting?*

## 1-4 Report Structure

- **Chapter 2** explore the characteristics and key components of the helical wake that can be used for the synchronization. With this information, the requirements for the controller design will be established. After this, the implementation of two controller strategies will be elaborated.
- **Chapter 3** will test the capabilities of both controllers in a controlled environment for a low-order model with known dynamics. On top of that, this will help understand the limitations of both strategies.
- **Chapter 4** presents the simulation setups and experiments for the helix wake synchronization in a high-order wind turbine model. Three different simulation environments with increasing fidelity will be explained and the experiment results will be discussed.
- **Chapter 5** will derive the stability conditions for both controller schemes. It will also assess the stability and performance criteria for one of the controllers for the synchronization problem itself.
- **Chapter 6** this final chapter will go over the main conclusions of findings and results presented in this thesis. It will also provide the answers to the research questions defined above. Furthermore, several recommendations are given for future research.

# Chapter 2

# Preliminaries and Controller Strategies

This chapter will investigate various aspects of the interaction of helical wake on a downstream turbine in a two-turbine setting. With this information, different controller strategies will be explored that can exploit this information. First, this chapter will dive into preliminary knowledge about the Multi-Blade Coordinate (MBC) transformation and different reference frames that can be used to analyze the helix method. These different reference frames will be useful later in the initial controller description. The second section of this chapter will look at how the helix method affects a waked downstream turbine and the phase information contained in the helical wake. From this, a strategy given the name *Helix Wake Synchronization*, will be introduced. Applying this strategy in a closed-loop setting requires the consideration of some additional measures, which will also be discussed. In the last part of this chapter, two different control strategies and their implementation are explained in more detail.

## 2-1 Multi-Blade Coordinate Transform

The helix approach utilizes the MBC transformation to create varying bending moments on the rotor disc. The application of the MBC transformation in the wind turbine industry was adapted from an analysis of helicopter rotor dynamics performed by Coleman and Feingold [28]. This idea originated in the field of electrical engineering where it was used to simplify three-phase synchronous machine problems [29]. What these systems have in common, is a multi-element vector (e.g. three blades) rotating about an axis. To analyze such a system it can be viewed from different reference frames. For three-phase systems, the original reference frames are the rotating three-axis reference frame ($abc$), rotating orthogonal two-axis reference frame (*direct-quadrature-zero* or $dq0$), and the stationary orthogonal two-axis reference frame ($\alpha\beta 0$). Linear transformations and their inverse transformations describe mathematical conversion between these reference frames. For wind turbines, going from the individual blade dynamics to the combined dynamics can be characterized by the forward MBC transformation. This is identical to going from an $abc$ reference frame to the $dq0$ reference frame. In electrical engineering, this is also referred to as the Park transformation. This section discusses in more detail the various frames of reference and their transformations. An overview

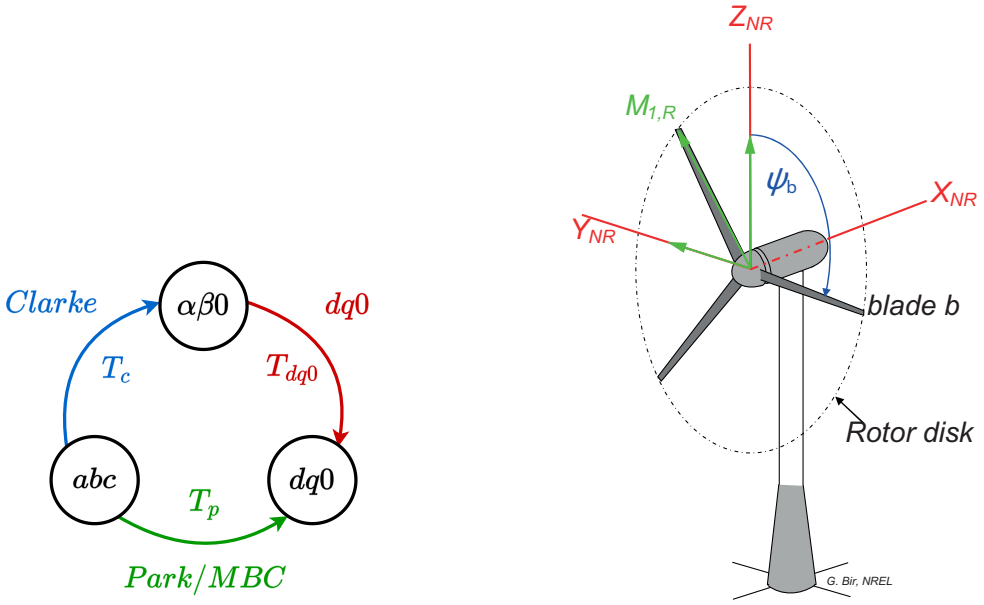



**Figure 2-1: Left**: relationships between different frames of reference described by the Park/MBC ($T_p$) and Clarke transformations ($T_c$). The arrows denote forward transformations. Inspired by [30]. **Right**: rotating (R) and Non-rotating (NR) reference frames for a wind turbine in Cartesian $XYZ$-coordinates. The azimuth angle of the $b$-th blade is given by $\psi_b$. $M_{1,R}$ denotes a rotating component of the first blade. The green arrows are the projections of this component on the $y$- and $z$-axes. Figure adapted from [31].

of these relationships is shown in Figure 2-1 on the left. In the following section, the different reference frames and their application to the Helix method are further elaborated.

### 2-1-1 Change of Reference Frame

For three-phase systems, the $abc$ components consist of three signals $v$ each 120° phase shifted from each other. The conversion from the $abc$ axes to a stationary two-axis $\alpha\beta 0$ framework is described by the Clarke transformation [32]. This transformation simplifies unbalanced three-phase problems because it does not require complex numbers or a 120° phase shift operator. The 0 component is defined as the mean of the $abc$ components, also known as the zero sequence. In Equation 2-1 the Clarke transformation, $T_c$, is written in matrix form as

$$\underbrace{\begin{bmatrix} v_0 \\ v_\alpha \\ v_\beta \end{bmatrix}}_{v_{\alpha\beta 0}} = \underbrace{\frac{2}{3}\begin{bmatrix} \frac{1}{2} & \frac{1}{2} & \frac{1}{2} \\ 1 & -\frac{1}{2} & -\frac{1}{2} \\ 0 & \frac{\sqrt{3}}{2} & -\frac{\sqrt{3}}{2} \end{bmatrix}}_{T_c} \underbrace{\begin{bmatrix} v_a \\ v_b \\ v_c \end{bmatrix}}_{v_{abc}}. \tag{2-1}$$

Going from the stationary two-axis framework to a rotating two-axis framework can be described by a $dq0$ transformation, $T_{dq0}$. This is a regular Euler rotation about the 0-axis. The transformation rotates the $\alpha\beta 0$ framework by $n\psi$ degrees, where $n$ is the harmonic number and $\psi$ can either be a constant phase or a phase changing over time. The matrix form of this

transformation is defined as

$$\underbrace{\begin{bmatrix} v_0 \\ v_d \\ v_q \end{bmatrix}}_{v_{dq0}} = \underbrace{\begin{bmatrix} 1 & 0 & 0 \\ 0 & \cos(n\psi) & -\sin(n\psi) \\ 0 & \sin(n\psi) & \cos(n\psi) \end{bmatrix}}_{T_{dq0}(n\psi)} \begin{bmatrix} v_0 \\ v_\alpha \\ v_\beta \end{bmatrix}. \tag{2-2}$$

Note that consecutively applying the Clark and $dq0$ transformations to an $abc$ framework will result in a $dq0$ framework. Hence, these two steps can be combined into one transformation to directly go to this frame of reference. This is given by the aforementioned Park transformation, $T_p$. Depending on the application, the geometric interpretation of this transformation can differ. For wind turbines, a good way of understanding this transformation is by viewing it as a projection of individual rotating blade components onto the stationary Cartesian $y-$ and $z$-coordinates. This is illustrated in the right part of Figure 2-1. This also gives an intuitive explanation of the components of the transformation. The phase angle $n\psi$ can now be viewed as the azimuth angle of the rotor times a harmonic number. While the phases $\frac{2}{3}\pi$ and $\frac{4}{3}\pi$ denote the 120° phase difference between the blades. Equation 2-3 gives the matrix form of this transformation,

$$\begin{bmatrix} v_0 \\ v_d \\ v_q \end{bmatrix} = \underbrace{\frac{2}{3}\begin{bmatrix} \frac{1}{2} & \frac{1}{2} & \frac{1}{2} \\ \cos(n\psi) & \cos\left(n\psi + \frac{2}{3}\pi\right) & \cos\left(n\psi + \frac{4}{3}\pi\right) \\ \sin(n\psi) & \sin\left(n\psi + \frac{2}{3}\pi\right) & \sin\left(n\psi + \frac{4}{3}\pi\right) \end{bmatrix}}_{T_p(n\psi)} \begin{bmatrix} v_a \\ v_b \\ v_c \end{bmatrix}. \tag{2-3}$$

In literature, the $T_{dq0}$ transform is sometimes called the Park transform and vice versa. As the original Park transformation is defined as given in Equation 2-3, this report will continue with this definition. For wind turbines, the Park transformation is called the MBC transformation instead. Note that these transformations are defined for three-component, or three-phase, systems. However, these transformations can easily be extended for $n$-component symmetrical systems which are $\frac{2\pi}{n}$ radians apart, where $n \geq 2$. This is, for example, described in [33]. To summarize, the effect of these different transformations on three-phase signals in the time domain is shown in Figure 2-2. This also gives a physical interpretation of the transformations. It can be seen that the $\alpha\beta0$ framework gives information about the Direct Current (DC) components of the signals. Whereas the $dq0$ framework gives information about the rotating components. These aspects will be exploited in later chapters. To better understand the geometrical interpretation of these transformations, the interested reader is referred to [30] where they give a comprehensive analysis.

### 2-1-2 The MBC Transformation and the Helix Method

As explained in the previous part, the MBC transformation can be used to go from a rotating framework of the rotor blades to a non-rotating framework of the rotor and vice versa via a projection. This conversion has been used in literature to enhance wake mixing by inducing a dynamic force vector on the airflow [22]. As this force rotates over time, the direction of the wake changes as well, hence increasing wake mixing. Frederik et al. found that dynamically varying the tilt and yaw moments with a periodic signal phase-shifted by 90 degrees resulted

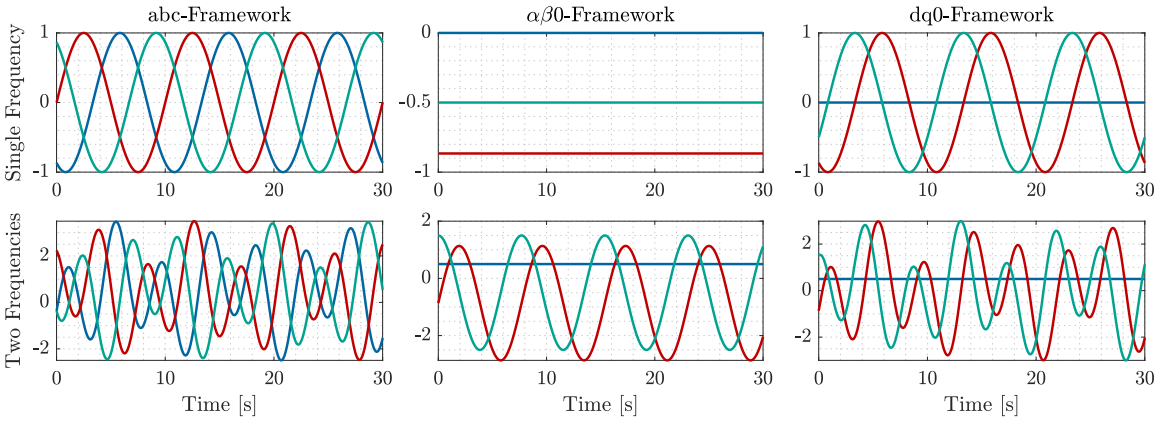



**Figure 2-2:** Time-domain interpretation of Clarke and Park transformations for three-phase signals. The top row shows $\alpha\beta 0$ and $dq0$ signals from a single frequency $abc$ framework with a small phase offset on top of their phase shifts. The bottom row shows the same effect, although a second frequency with a different amplitude is added to the signal.

in a helix-shaped wake, which significantly enhanced wake mixing. The MBC transformation can thus be used to map the individual rotating blade moments to the stationary tilt and yaw moments on the rotor disc. These former moments can be induced by superimposing sinusoidal tilt and yaw pitch angles in the non-rotating reference frame. These signals can be converted to individual pitch angles via the inverse, or backward, MBC transformation. Figure 2-3 shows a schematic representation of this feedforward scheme to generate the varying tilt and yaw moments. The forward MBC transformation for the conversion of the individual

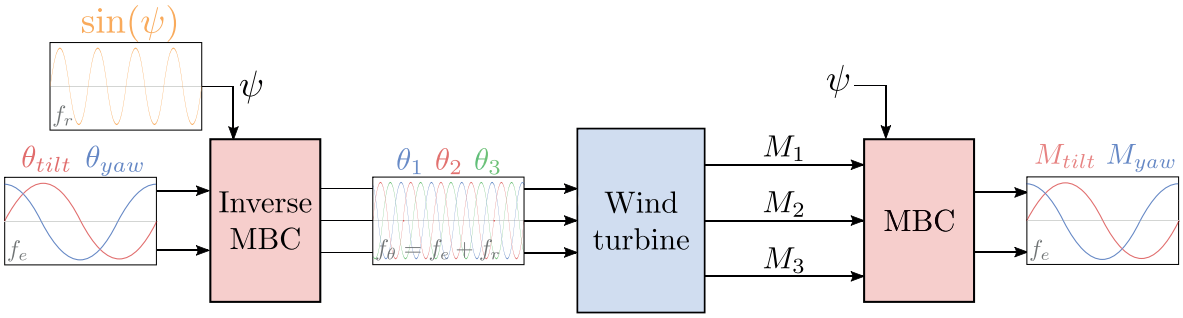



**Figure 2-3:** Schematic representation of the use of the MBC transformation to achieve periodic yaw and tilt moments on the turbine rotor. Here, $\theta_{tilt}$, $\theta_{yaw}$, and $\theta_{1,2,3}$ are the tilt, yaw, and individual pitch angles respectively. The rotor azimuth angle is given by $\psi$. $M_{tilt}$, $M_{yaw}$, and $M_i$ are the tilt, yaw, and individual blade bending moments respectively. Finally, $f_e$, $f_r$, and $f_\theta$ are the excitation, rotor, and pitch frequencies for a Counter-Clockwise (CCW) helix method respectively. Figure adapted from [22].

blade moments is given by

$$\begin{bmatrix} M_0 \\ M_{\text{tilt}} \\ M_{\text{yaw}} \end{bmatrix} = \frac{2}{3} \begin{bmatrix} \frac{1}{2} & \frac{1}{2} & \frac{1}{2} \\ \cos(\psi_1) & \cos(\psi_2) & \cos(\psi_3) \\ \sin(\psi_1) & \sin(\psi_2) & \sin(\psi_3) \end{bmatrix} \underbrace{\begin{bmatrix} M_1 \\ M_2 \\ M_3 \end{bmatrix}}_{M} = T_p(\psi) M, \tag{2-4}$$

which is identical to Equation 2-3 with $n = 1$. For a three-bladed turbine, we obtain:

$$\psi_i = \psi + \frac{2\pi(i-1)}{3} \quad \forall i \in [1, 2, 3], \tag{2-5}$$

where $\psi$ is the rotor azimuth angle. Likewise, the backward MBC transformation allows us to go from a non-rotating framework to the individual blade pitch angles via

$$\underbrace{\begin{bmatrix}\theta_1\\ \theta_2\\ \theta_3\end{bmatrix}}_{\theta} = \begin{bmatrix}1 & \cos(\psi_1) & \sin(\psi_1)\\ 1 & \cos(\psi_2) & \sin(\psi_2)\\ 1 & \cos(\psi_3) & \sin(\psi_3)\end{bmatrix} \underbrace{\begin{bmatrix}\theta_0\\ \theta_{\text{tilt}}\\ \theta_{\text{yaw}}\end{bmatrix}}_{\theta_{dq0}} = {T_p}^{-1}(\psi)\theta_{dq0}, \tag{2-6}$$

which is an application of the inverse of Equation 2-3 with $n = 1$. In Figure 2-3, the tilt and yaw moments are shifted by 90°. This causes the tilt angle to be at maximum when the yaw angle is zero and vice versa. According to the [22], this results in a helical wake that rotates CCW with a frequency of $\omega_r + \omega_e$, where $\omega_r$ is the rotor speed and $\omega_e$ is the excitation frequency in radians per second. A Clockwise (CW) rotation can also be induced by shifting the tilt and yaw moments by 270° instead. Similarly, the CW helix rotates with a rotational frequency of $\omega_r - \omega_e$, which is slightly slower than the CCW helix.

This section described the various aspects of the MBC transformation and its counterparts, the Clarke and the $dq0$ transformation. The MBC transformation plays an important role in the control of the helix method, as varying tilt and yaw moments need to be imposed on the rotor disc. The following section will explore the interactions between a downstream turbine and an incoming helical wake. The knowledge about these interactions, together with the different reference frames, will become important for the controller design in the final two sections of this chapter.

## 2-2 Interaction with a Downstream Turbine

In this section, the interactions between the downstream turbine and the incoming helical wake are investigated in three different cases. These cases are depicted in Figure 2-4. The first case represents an upstream turbine (T1) performing the helix method while a downstream turbine (T2) is running a baseline pitch and torque controller without dynamic wake mixing. The baseline controller specifications will be explained further in Section 4-1. For the second case, T2 is performing the helix method while it experiences steady wind inflow without a helical wake. The third case is a combination of the latter two, where both turbines are performing the helix method. For each case, the tilt and yaw blade bending moments of the downstream turbine T2 are analyzed. This is shown in Figure 2-5. Here, it can be seen that for Case 1, T2 only experiences the helical wake created by T1. Similarly, for Case 2, only the bending moments caused by performing the helix method can be measured. This is equivalent to the output of the feedforward scheme presented in Figure 2-3. Case 3 experiences both the bending moments caused by the helical wake and the helix method itself. By summing up the bending moments from Case 1 and Case 2, we are left with bending moments that closely resemble those of Case 3. This is shown in the bottom right of Figure 2-5, where Case 3 is shown as well with dashed lines. We therefore can approximate the interaction

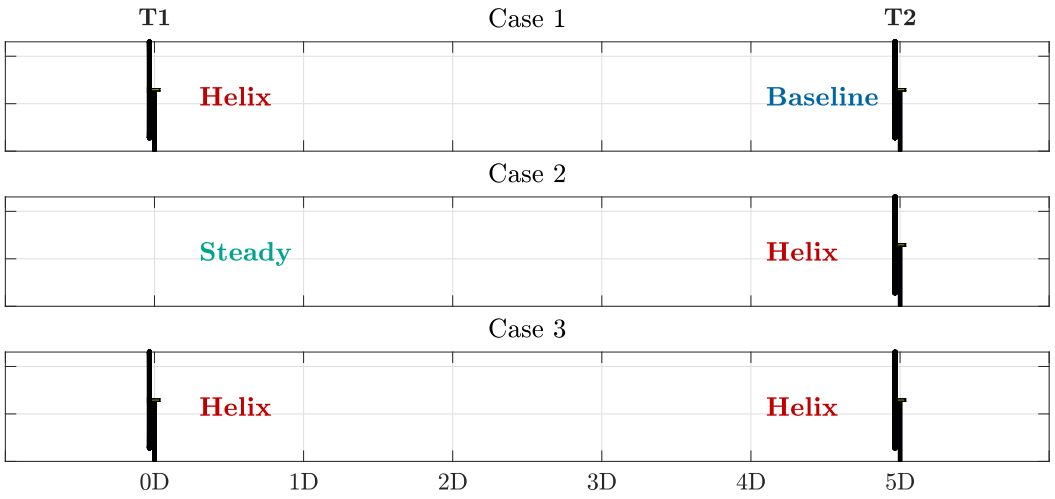



**Figure 2-4:** Turbine layout and control methods of three cases for a 5D separated two-turbine scenario. Case 1 has an upstream turbine (T1) performing the helix method while a downstream turbine (T2) runs a baseline controller. Case 2 only contains T2 and experiences a steady wind inflow. For Case 3, both T1 and T2 perform the helix method. T1 always experiences a below-rated steady wind inflow coming from the left of the figure.

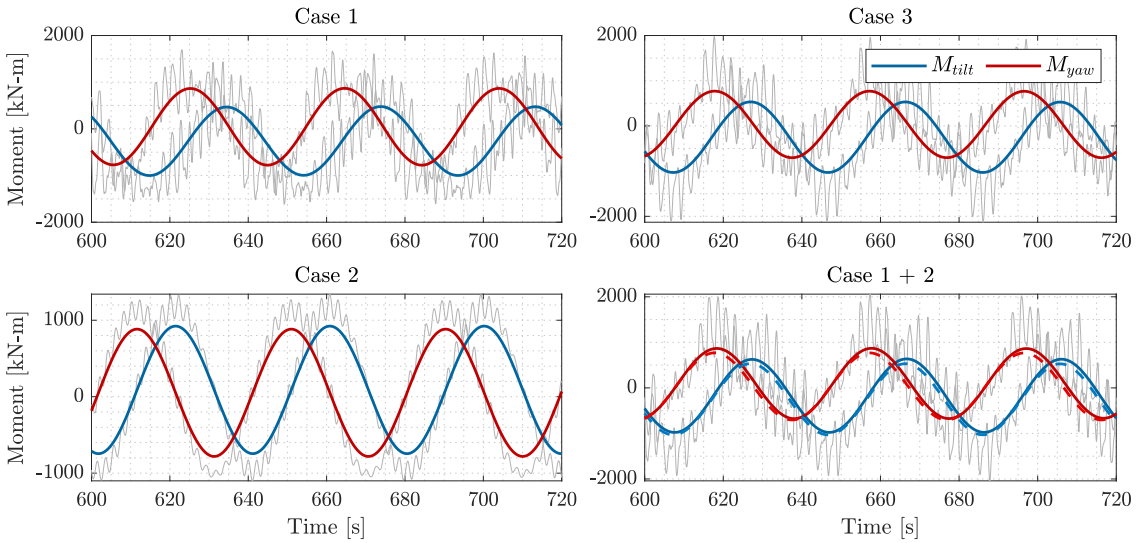



**Figure 2-5:** Simulation of cases from Figure 2-4 showing tilt and yaw blade bending moments of the downstream turbine T2. Simulations are performed in OpenFAST for an *NREL 5-MW* reference turbine experiencing and/or performing a CCW helix. For the bottom-right simulation, Case 3 is shown as well in dashed lines. The data is filtered using a low-pass filter leaving the excitation frequency $\omega_e$ and DC-offsets. The unfiltered data is shown in gray.

between a helical wake and the control effort of the helix method in a downstream turbine as a superposition of both signals. Mathematically, this can be described by an arbitrary phase

shift such that

$$\underbrace{a\sin(\omega_e t+\theta_a)}_{\text{Case 1: Helical Wake Inflow}} + \underbrace{b\sin(\omega_e t+\theta_b)}_{\text{Case 2: Helix Method}} = \underbrace{c\sin(\omega_e t+\phi)}_{\text{Case 3: Output}}, \tag{2-7}$$

where $\theta_a$ is the phase of the incoming helical wake, $\theta_b$ is the phase of the helix method and $\phi$ is the resulting phase of the interaction. The parameters $a$, $b$, and $c$ represent the amplitudes of the MBC-transformed bending moments for the incoming helical wake, control action, and output respectively. The amplitude of the resulting signal can be computed following

$$c^2 = a^2 + b^2 + 2ab\cos(\theta_a - \theta_b). \tag{2-8}$$

This relation has two interesting applications, namely being in-phase or out-of-phase with the incoming helical wake. For the case when $\theta_a = \theta_b$, we find that the amplitude c is at its maximum. While in the case $\theta_a = \theta_b - \pi$, the amplitude c will be minimal. These represent cases of constructive and destructive interference respectively and will be referred back to in later chapters. Considering the interaction between a helical wake and a downstream turbine performing the helix method as an interference problem is the core concept that will be explored in this report. In the next part, the phase information in the helical wake is investigated and it is presented how this information can be used for helix wake synchronization control.

### 2-2-1 Phase Information of the Helical Wake

The previous part showed how the incoming helical wake and a downstream turbine interact via blade bending moments in a $dq0$ reference frame. This section will investigate the phase information in the helical wake by analyzing the bending moments of an *NREL 5-MW* reference turbine. This turbine is performing a CCW helix method with a pitch amplitude of 2.5° under steady wind conditions. In this scenario, (Case 2), we can uncover what the desired result for a downstream turbine should look like. On top of that, we can relate these bending moments to the phase of the helix. Figure 2-6 shows the Welch power spectra estimates (see e.g. [34]) of the bending moments of this scenario in three different forms.

Additionally, the power spectra of the individual Blade Out-of-Plane (BOoP) bending moments are shown. Here, it can be seen that the resulting peak at $1P + f_e$ is in line with Figure 1-4 and [22] for a CCW helix. By transforming these bending moments via the MBC transform $T_p(\psi)$ (Equation 2-3), with $\psi$ being the rotor azimuth angle at time $t$, we get the result in the middle of Figure 2-6. In the frequency domain, the MBC transform shifts the rotor frequency, defined by 1P, to the zero frequency, or DC offset. This also highlights why the MBC transform converts the rotating system into a *non-rotating* system because the time-varying nature of the rotor speed is removed. However, this does not transform the system from a time-variant to a time-invariant system, since other time-variant components, such as the $3P$ frequency, are still present. The frequency at $1P + f_e$ is now shifted to the excitation frequency $f_e$, which corresponds to the output of the feedforward scheme in Figure 2-3. This means that all the necessary information about the helix is present at this frequency. One strategy could, therefore, be to filter out the excitation frequency $f_e$ from this MBC transform result.

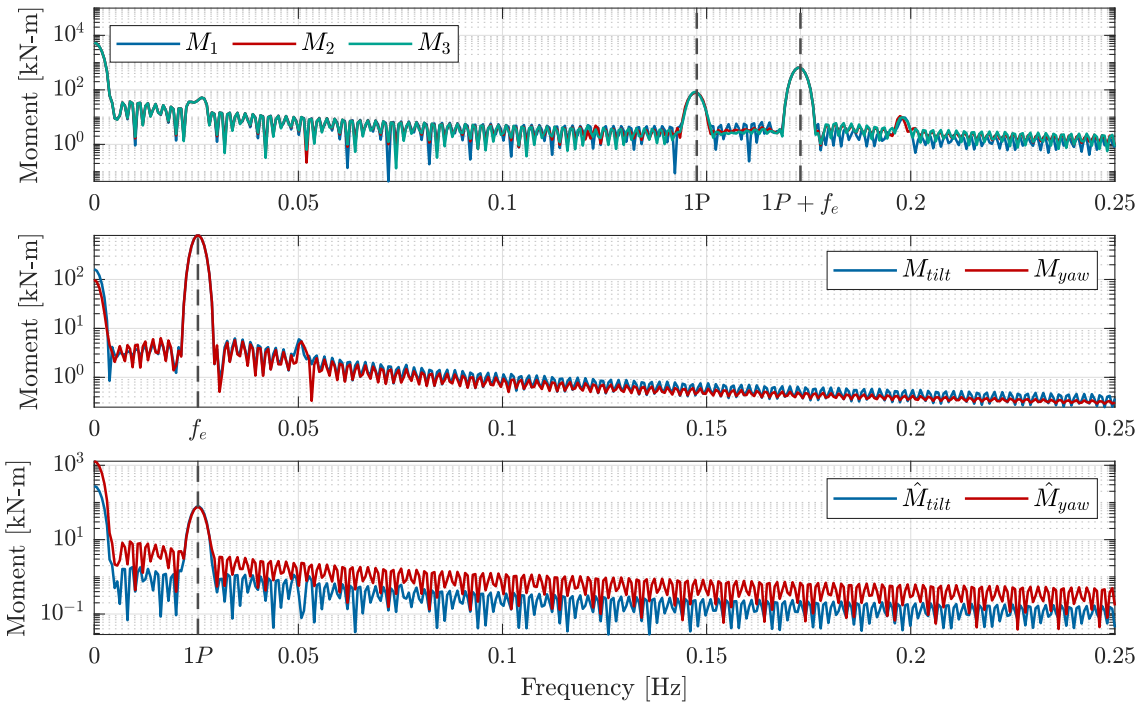



**Figure 2-6:** Welch power spectra for three different reference frames of the blade bending moments. **Top:** power spectra estimates of individual blade bending moments. The Once-per-Revolution (1P) and $1P + f_e$ frequencies are shown with the dashed lines. **Middle:** this spectrum shows the tilt and yaw bending moments from a $T_p(\psi)$ transformation. **Bottom:** power spectra of resultant tilt and yaw moments from a $T_p(\psi + \omega_e t)$ transformation. The shifted versions of $1P + f_e$ and 1P frequencies are denoted by dashed lines as well.

Another method of extracting the phase information of the helical wake is by analyzing the result of transforming the bending moments with $T_p(\psi + \omega_e t)$, where $\omega_e = 2\pi f_e$ [rad/s]. This gives a similar result as the previous transformation. However, now the $1P + f_e$ peak is shifted to the zero frequency instead. This can be interpreted as a non-rotating system from the helix's point of view, which implies that the phase information is contained in the DC offset. The phase can be computed by extracting this DC offset from these signals. A mathematical derivation of this is given in Appendix A-1. Using either the output of $T_p(\psi)$ or $T_p(\psi + \omega_e t)$ provides a means of estimating the phase via the blade bending moments. This estimated phase can then be used as control input for the helix method in T2, which results in the synchronization of T2 with the incoming wake. This method is therefore named helix wake synchronization control. It is not unlikely that other quantities, such as wind speed components, could be used to estimate the phase of the helical wake. However, as the goal of the feedforward scheme presented in Figure 2-3 is to generate sinusoidal tilt and yaw moments that are 90° out of phase, the focus of the synchronization will be on these moments as well. This also simplifies comparing, e.g, a synchronized with a non-synchronized helix. The next section will explore different aspects of closed-loop synchronization and various control strategies for helix wake synchronization in a downstream turbine.

## 2-3 Closed-Loop Helix Wake Synchronization

So far, this chapter has introduced different reference frameworks to analyze the helix method and the interactions between a downstream turbine and the helix method. MBC-transformed blade bending moments in a downstream turbine was found to be composed of the moments caused by the incoming helical wake and by the control action of the helix method. In Chapter 1, it was hypothesized that in-phase or out-of-phase synchronization with the incoming helical wake can be to the benefit of the downstream turbine. Therefore, as the previous section showed, the phase information of the helical wake has to be measured. When this phase is used for control purposes, it closes the control loop as it could alter the blade bending moments. To this end, this section will discuss two main considerations for closed-loop helix wake synchronization. First, the delay caused by coupling between the tilt and yaw control inputs is explained, and how it can be accounted for using an azimuth offset. Next, a performance measure for the level of interference is established. Finally, this section will end by listing possible controller strategies.

### 2-3-1 Optimal Azimuth Offset

The feedforward scheme presented in Figure 2-3 does not take into account possible phase lag caused by coupling and actuator delays. In industry, it is common for load mitigation with Individual Pitch Control (IPC) to apply an azimuth offset $\psi_0$ in the inverse MBC transform to compensate for this effect [35]. The interpretation and analysis of the optimal azimuth angle $\psi_0^*$ have been further studied in [36]. The optimal azimuth offset results in the least amount of coupling between the control inputs, resulting in a reduced phase lag. For closed-loop helix synchronization, this means that an azimuth angle needs to be incorporated as well. Otherwise, the synchronization might be delayed depending on the wind turbine used. [36] uses the identification of the spectral model between the tilt and yaw pitch input and the tilt and yaw blade bending moment output to estimate $\psi_0$. For helix wake synchronization, we are not interested in the azimuth offset which minimizes the coupling between the two inputs over a selected frequency range. Instead, we are only interested in the exact phase delay if we are using sinusoidal input signals at the excitation frequency $\omega_e$.

To demonstrate this, let us consider a linear parameter varying transfer function $\mathbf{G}(s, \omega_r)$, where $s$ is the Laplace variable and $\omega_r$ is the rotor rotational frequency. This could be either a linearized model, as will be derived in Section 4-1 or a spectral model as was used in [36]. Assuming we only use sinusoidal inputs which are 90° out-of-phase, and $\omega_r$ is constant, we get the following relation between the input and output:

$$\begin{aligned}
\begin{bmatrix} M_{\text{tilt}}(s) \\ M_{\text{yaw}}(s) \end{bmatrix} &= \underbrace{\begin{bmatrix} G_{11}(s,\omega_r) & G_{12}(s,\omega_r) \\ G_{21}(s,\omega_r) & G_{22}(s,\omega_r) \end{bmatrix}}_{\mathbf{G}(s,\omega_r)} \begin{bmatrix} \theta_{\text{tilt}}(s) \\ \theta_{\text{yaw}}(s) \end{bmatrix} = \mathbf{G}(s,\omega_r)\mathcal{L}\left\{ \begin{bmatrix} \sin(\omega_e t) \\ \cos(\omega_e t) \end{bmatrix} \right\}(s) \\
\begin{bmatrix} M_{\text{tilt}}(t) \\ M_{\text{yaw}}(t) \end{bmatrix} &= \begin{bmatrix} |G_{11}(j\omega_e)| \sin(\omega_e t + \angle G_{11}(j\omega_e)) + |G_{12}(j\omega_e)| \cos(\omega_e t + \angle G_{12}(j\omega_e)) \\ |G_{21}(j\omega_e)| \sin(\omega_e t + \angle G_{21}(j\omega_e)) + |G_{22}(j\omega_e)| \cos(\omega_e t + \angle G_{22}(j\omega_e)) \end{bmatrix}.
\end{aligned} \tag{2-9}$$

Here, $G_{ik}(j\omega_e)$ denotes the Fourier domain transfer function element of the $i^{\text{th}}$ row and $k^{\text{th}}$ column evaluated at frequency $\omega_e$ and likewise, $G_{ik}(s, \omega_r)$ denotes the Laplace domain

transfer function element of $\mathbf{G}(s, \omega_r)$. The $\mathcal{L}\{\bullet\}(s)$ denotes a Laplace transformed function. The complex number is represented by $j$, and the $|(\bullet)|$ and $\angle(\bullet)$ denote the magnitude and the phase respectively. In the case of $\mathbf{G}(s, \omega_r)$ being symmetric, we can compute the phase delay using the expression:

$$\psi_d = \frac{|G_{11}(j\omega_e)| \sin(\angle G_{11}(j\omega_e)) + |G_{12}(j\omega_e)| \cos(\angle G_{12}(j\omega_e))}{|G_{21}(j\omega_e)| \sin(\angle G_{21}(j\omega_e)) + |G_{22}(j\omega_e)| \cos(\angle G_{22}(j\omega_e))}, \tag{2-10}$$

where $\psi_d$ is the phase delay, which can be derived from Equation 2-7. We can thus take the azimuth offset $\psi_0 = -\psi_d$, as this will result in a minimal phase delay. The azimuth offset will be used throughout this report. In Chapters 3 and 4 it will be used during the evaluation of various results and in Chapter 5 an analysis of errors in the azimuth offset will be given. The next section will present a measure of the sensitivity in the phase, which could be the result of an error in the azimuth offset.

### 2-3-2 Sensitivity in the Phase

The previous part showed the first aspect to be taken into account for helix wake synchronization. In this part, a performance measure will be derived which can be used to determine the quality of the interference. Consider the equations given in Equation 2-7 and Equation 2-8. The latter measures the amount of interference between the helical wake inflow and the control action of the helix. As stated before, $\theta_b = \theta_a$ implies maximum or constructive interference, whereas $\theta_b = \theta_a - \pi$ implies minimum or destructive interference. One question that naturally arises when trying to synchronize two waves in a control-setting, is how much error from $\theta_a$ is allowed in $\theta_b$. More specifically, we want to define an upper bound such that $|\theta_a - \theta_b| \leq \Delta\phi$, for which a given amount of constructive interference is still achieved. For example, we want to find the smallest possible positive $\Delta\phi$ for which

$$\left| \frac{c_{\max} - c(a,b)}{c_{\max} - c_{\min}} \right| \leq \epsilon, \, \forall \, a, b > 0, \tag{2-11}$$

where $c_{\max}$ denotes the maximum possible constructive interference if $\theta_a = \theta_b$, $c_{\min}$ denotes the minimum possible destructive interference if $\theta_a - \pi = \theta_b$, and $\epsilon$ denotes some upper bound. For this, we consider $\theta_a = 0$, $\theta_b \in [0, \, \pi]$, and all values $a, b \in \mathbb{R}_{>0}$, where $\mathbb{R}_{>0} = \{x \in \mathbb{R} \,|\, x > 0\}$ denotes the subset of all real positive valued numbers larger than zero. Next, we define the following equation:

$$\Sigma_{ab}(\Delta\phi) = \frac{\sqrt{a^2 + b^2 + 2ab\cos(\Delta\phi)} - |a - b|}{a + b - |a - b|}, \quad \text{where } a, b > 0, \tag{2-12}$$

which satisfies $\Sigma_{ab}(\Delta\phi) \in [0, \, 1]$ and thus represents a scaled version of Equation 2-8. Here, 0 corresponds to destructive interference and 1 to constructive interference. The scaling is required to generalize for all possible values of $a$ and $b$. Following the proof presented in Appendix A-2, we find that the smallest possible curve which satisfies Equation 2-12 equals $\Sigma^-_{ab}(\Delta\phi) = \cos^2(\Delta\phi/2)$, where $\Sigma^-_{ab}(\Delta\phi)$ denotes the infimum of Equation 2-12. With this, we can define an upper bound $\epsilon$ and compute the maximum error $\Delta\phi$ as follows:

$$\epsilon = 1 - \Sigma^-_{ab}(\Delta\phi) = 1 - \cos^2\left(\frac{\Delta\phi}{2}\right) \quad \longrightarrow \quad \Delta\phi = 2\arccos\left(\sqrt{1 - \epsilon}\right). \tag{2-13}$$

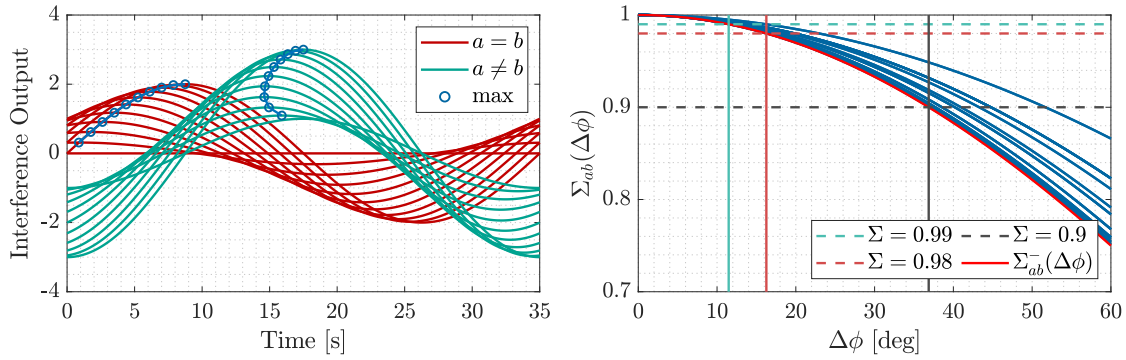



**Figure 2-7:** Example interference output and scaled amplitudes of resulting interference. **Left:** visual representation of the computation of peak amplitudes $c$. For each combination amplitudes of interfering signals $a$ and $b$, the peak value is computed over over $\theta_a = 0$, $\theta_b \in [0, \pi]$. The resulting set of blue points forms the basis of the blue lines presented on the right. **Right:** the peak values are scaled for all $\{a, b\}$ such that minimum interference equals $\Sigma_{ab}(\Delta\phi) = 0$ and maximum interference equals $\Sigma_{ab}(\Delta\phi) = 1$. The red line indicates $\Sigma_{ab}^{-}(\Delta\phi)$, which is the smallest possible line in this set. The horizontal dashed and vertical solid lines represent points on $\Sigma_{ab}^{-}(\Delta\phi)$ for which a certain level of interference is achieved.

Figure 2-7 displays a visual interpretation of deriving the bounds $\epsilon$ and $\Delta\phi$. On the left of Figure 2-7, two examples are shown for computing the peak amplitudes $c$ for different $\Delta\phi$ and combinations of $a$ and $b$. The connected blue dots represent curves on the right of Figure 2-7 which are scaled to generalize the problem (blue lines). Here, it can be seen that $\Sigma_{ab}^{-}$ indeed is the minimal curve in this set, and thus serves as a worse-case. Using $\Sigma_{ab}^{-}$, we can find the minimum attainable level of interference for every phase error $\Delta\phi$. Figure 2-7 shows a few example cases. For example, to achieve an interference within 1% of $c_{\max}$, the error in the phase has to be within $\Delta\psi = 2\arccos\left(\sqrt{0.99}\right) \approx 11.4°$. This method will become useful during the presentation of the results, as it tells us how much error is allowed before a level of performance is lost. The next section will go over various controller options that could be used to achieve helix wake synchronization.

### 2-3-3 Controller Options

The previous part described two concerns for using helix wake synchronization in a closed-loop setting. With this information, different controller strategies can be defined for different synchronization purposes. This section will elaborate on four different controller types that can be used for this problem. The azimuth offset and sensitivity in the phase are of importance for all of the below-listed controller types. The azimuth offset has to be considered to account for the coupling between the tilt and yaw pitch control inputs at the excitation frequency. Similarly, the sensitivity in the phase serves as a performance measure. This measure can provide an indication of the degree of constructive or destructive interference, depending on whether the incoming helical wake is amplified via synchronization or rejected. The different controller types are listed below. After this section, the implementation of two controller strategies will be further explained.

- *Classical Filtering Methods:* As was explained in Section 2-2-1, the phase information in the helical wake can be extracted using filtering methods. A first good option for this is classical filtering methods such as Low-Pass (LP), notch, or Moving-Average Filter (MAF) (see e.g. [37]). These filters are Single-Input Single-Output (SISO) frequency-based which are relatively easy to implement. A notch filter could be implemented to filter out the excitation frequency from the $T_p(\psi)$ transformed bending moments (middle of Figure 2-6). Likewise, an LP or MAF can be used to filter out the DC offset of the $T_p(\psi + \omega_e t)$ transformed bending moments. One downside of these filters is that they can add a significant amount of delay to the estimation. It would therefore take a considerable amount of time to get an estimate which is relatively constant over time. These filters can however still be implemented in combination with other filter or controller options.

- *IPC-Type:* In Section 2-3-1, it was mentioned that IPC is a common option in the industry for load mitigation in wind turbines. IPC can be implemented as a PID-type (Proportional, Integrator, Derivative) controller. Although such a controller is not suited for estimation problems, IPC could be used to reject the incoming helical wake by tracking a zero reference on the tilt and yaw blade bending moments. This would be similar to implementing a synchronized helix method which tries to go out of phase with the incoming helical wake to create destructive interference. This would significantly simplify the problem, as the frequency and phase information is no longer required for control. Classical IPC is a SISO controller, hence to account for coupling an optimal azimuth angle has to be considered as well. In [38], $\mathcal{H}_\infty$ loop-shaping was implemented to achieve decoupled IPC in a Multi-Input Multi-Output (MIMO) setting. Similarly, for this application, a MIMO weighting design could also be used to limit the frequency range of the control action such that IPC mainly rejects the excitation frequency. Such controller designs are, however, already widely available in the literature.

- *Adaptive Filtering Methods:* As the classical filtering methods are prone to delays and the IPC-type controller is not suited for this estimation problem, more advanced control methods can be implemented. Adaptive filters have internal dynamics which depend on the input itself and are thus recursively updated as more input becomes available. Adaptive filters are in their essence optimization problems that solve quadratic cost functions and become maximum likelihood estimators under the presence of Gaussian measurement noise [37, Chapter 21]. A broad family of adaptive filters and their extensions is available, but for this problem, we can consider a model-based Kalman Filter (KF) and model-free Recursive Least Squares (RLS) filter. The KF can be used as a MIMO state estimator and requires a linearized state-space model of our system and could therefore result in a very accurate estimate. Likewise, the RLS can also be implemented as a MIMO estimator but does not necessarily require a model of our system. This could make it more adaptive to different wind speeds. Both are therefore good options for estimating the phase of the incoming helical wake.

- *Data-Driven Repetitive Control Methods:* Similar to the IPC-type case, repetitive control (RP) could also be used to reject an incoming helical wake. The RP controller uses the information that the helical wake repeats itself every $1/f_e$ seconds. An RP control law considers a difference operator as states, such that $\delta d_k = d_k - d_{k-P}$, where $d_k$ is a periodic disturbance and $P$ represents the period length. This removes the periodic

component and leaves the aperiodic components. The model-free extension, subspace predictive repetitive control, could also be implemented [39] as this would make the controller adaptive to different wind speeds. The predictive nature of this controller is also suitable to incorporate constraints to limit e.g. the pitch amplitude or rate as was done in [40]. Compared to the other proposed control methods, SPRC is more complex and therefore more difficult to implement.

In this section, several valid control options have been listed for different control purposes. The two main options are pure rejection methods and estimation problems. The latter is preferred to the pure rejection methods, such as IPC since they are not suitable for in-phase synchronization. SPRC could be implemented at the 1P frequency to estimate the non-rotating dynamics of the wind turbine. It could then be used similarly to a KF estimator to estimate the phase. This is however harder to implement compared to the KF method. Moreover, both IPC and SPRC are already known in the literature for similar problems. Therefore, the estimation of the phase of the incoming helix is performed using two adaptive filtering strategies. The first one is the RLS method, which is suitable for different wind speeds since it is model-free. The second implementation is the KF-based estimator, which is model-based but can therefore lead to a more accurate estimate. These strategies will be further explained in the next two sections.

## 2-4 Recursive Least Squares Estimator

As pointed out in Section 2-2-1, the phase information of the incoming helical wake is contained in the DC offset of the resulting tilt and yaw moments from the $T_p(\psi + \omega_e t)$ transformation. These DC offsets can be estimated using filtering methods. Classical filters, such as low-pass filters, can be utilized to extract these values. However, such filters can impose a delay on the estimation process in the order of $f_e^{-1}$ seconds. This also does not guarantee constant values of $\hat{M}^{DC}_{tilt,\,yaw}$ as more time is required to filter out frequencies close to the zero frequency. A solution to this is to implement an adaptive filter that exploits some inherent information in the data to estimate the DC offsets. Such a solution is proposed in [41], [42] to solve a phase estimation problem in power converter applications by solving a weighted least squares estimator (WLSE) problem recursively. This is known as a recursive least squares adaptive filter [37, Chapter 21]. The following section will propose an RLS-based estimator to achieve helix wake synchronization via control. The first part will derive its dynamics which are based on exploiting the phase information of the helical wake. Secondly, the algorithm and a numerically robust extension will be given. After this, a method for converging to the correct phase will be explained. Finally, the complete controller scheme will be summarized.

### 2-4-1 Phase Information Exploit

The inherent information in the data that will be exploited is the fact that the DC information of the Park/MBC transform is contained in the Clarke transform (see Section 2-1-1). For this, the following vector is defined,

$$M_{dq}{}^{\top} = \begin{bmatrix} M_{dq}^{+1\top} & M_{dq}^{0\top} \end{bmatrix} = \begin{bmatrix} (T_p(\psi)M)^{\top} & (T_c M)^{\top} \end{bmatrix}. \tag{2-14}$$

Here, $M \in \mathbb{R}^3$ represents the individual blade bending moments and $T_p$, $T_c \in \mathbb{R}^{2\times 3}$ are the Park (Equation 2-3) and Clarke (Equation 2-1) transforms respectively, but only for computing the $d$ and $q$ components. The 0 component does not contain information about the phase of the helical inflow. Note that $M_{dq}^{+1}$, are just the tilt and yaw moments of the system, and $M_{dq}^{0}$ contains the Clarke transformed moments. $M_{dq}^{\top}$ is not a useful quantity by itself. However, it provides a means of telling the RLS estimator which frequency components to keep and which components to regard as noise. Likewise, we can define

$$M_{\alpha\beta} = M_{\alpha\beta}^{+1} + M_{\alpha\beta}^{0} = \underbrace{\begin{bmatrix} T_{dq}(\omega_e t) & T_{dq}(0) \end{bmatrix}}_{\mathbf{H}_k} M_{dq}, \tag{2-15}$$

where $T_{dq} \in \mathbb{R}^{2\times 2}$ is the $dq$ transformation. To give a more physical interpretation of $M_{dq}$ and $M_{\alpha\beta}$, we can represent Equation 2-15 as a summation of matrix-vector multiplications,

$$M_{\alpha\beta} = \sum_{n=0}^{+1} T_{dq}(n\omega_e t)) M_{dq}^{n} = \sum_{n=0}^{+1} T_p(n(\psi + \omega_e t)) M. \tag{2-16}$$

Here, $n$ is defined as the harmonic number of the corresponding frequencies. From this, it is clear that we are only interested in the $0^{\text{th}}$ and the $+1^{\text{st}}$ harmonics of $\psi$ and $\psi + \omega_e t$ for $M_{dq}$ and $M_{\alpha\beta}$ respectively. As was shown in Figure 2-6, these correspond exactly with the frequencies that we require to estimate the phase. We thus want the RLS estimator to estimate $\hat{M}_{\alpha\beta}$, where $(\hat{\bullet})$ denotes an estimated quantity, by minimizing the following error,

$$e_k = M_{\alpha\beta}(k) - \mathbf{H}_k \hat{M}_{dq}. \tag{2-17}$$

The solution $\hat{M}_{dq}$ can be used to extract $\hat{M}_{dq}^{0}$ which contains the DC offset needed to compute the phase via

$$\phi_k = \arctan\Big(\hat{M}_q^0, \hat{M}_d^0\Big). \tag{2-18}$$

Here, it is important to stress that the inverse tangent is computed via the `atan2` command in *MATLAB*, as this maps the output to $[-\pi, \pi]$ instead of $[-\frac{\pi}{2}, \frac{\pi}{2}]$.

### 2-4-2 The RLS Algorithm

The goal of the RLS algorithm is to solve a weighted least squares problem online recursively. The solution of minimizing the error given in Equation 2-17 at each time step $k$ is given by

$$\hat{M}_{dq}^{*} = \text{argmin}_{\hat{M}_{dq}} \sum_{k=0}^{j} \lambda^{j-k} \Big\| M_{\alpha\beta}(k) - \mathbf{H}_k \hat{M}_{dq} \Big\|_2^2, \tag{2-19}$$

where $\lambda$ is a forgetting factor ($0 \ll \lambda < 1$) to reduce the effect of past data and adapt to new dynamics of the system. The $(^*)$ indicated the optimal value. For this estimation problem, $\lambda$ is chosen via

$$\lambda = 1 - \frac{1}{N}, \tag{2-20}$$

where $N$ is the number of samples required for the estimation process. This will be in the order of $(f_e T_s)^{-1}$, where $T_s$ is the sampling time. Let $\hat{x}_{k-1} = \hat{M}_{dq}$ be a solution of Equation 2-19

at time $k-1$. Likewise, let $\hat{x}_k$ be a solution at time $k$. The RLS algorithm computes $\hat{x}_k$ from $\hat{x}_{k-1}$ through a recursive procedure. At each time $k \geq 0$, we compute:

$$\begin{aligned} K_k &= (\lambda^{-1} P_{k-1} \mathbf{H}_k^\top)(I - \lambda^{-1} \mathbf{H}_k P_{k-1} \mathbf{H}_k^\top)^{-1}, \\ \hat{x}_k &= \hat{x}_{k-1} + K_k(y_k - \mathbf{H}_k \hat{x}_{k-1}), \\ P_k &= \lambda^{-1}(P_{k-1} - K_k \mathbf{H}_k P_{k-1}^\top), \end{aligned} \tag{2-21}$$

where $P_k \in \mathbb{R}^{4\times4}$ is the updated covariance matrix of the process, $K_k \in \mathbb{R}^{4\times2}$ the updated controller gain matrix and $y_k = M_{\alpha\beta}$ is the measured output at time $k$. The algorithm is initialized using $P_{-1} = \Pi_0 \succ 0$ and $\hat{x}_{-1} = \mathbf{0} \in \mathbb{R}^4$.

### 2-4-3 The Square-Root RLS Algorithm

The recursive algorithm given in Equation 2-21 propagates the covariance matrix $P_k$ via a Riccati difference equation. The solution $P_k$ is, therefore, required to be positive definite in order for it to be a stabilizing solution [43]. However, because of roundoff errors, this Ricatti recursion may not guarantee positive definiteness of $P_k$ at all times $k$. An alternative algorithm called the square-root RLS or inverse QR algorithm, is therefore implemented. Equation 2-21 can be rewritten in a *factored* form which contains the terms for updating $P_k$ and $K_k$. Let $P_{k-1}^{1/2}$ denote a square-root factor of $P_{k-1}$ which satisfies

$$P_{k-1} = P_{k-1}^{1/2} P_{k-1}^{\top/2}. \tag{2-22}$$

For $P_{k-1} \succ 0$ and $P_{k-1}^{1/2}$ being a triangular square-root factor, this is known as the Cholesky factor. Then the factored form of Equation 2-21 can be written as

$$\begin{bmatrix} I_n & \frac{1}{\sqrt{\lambda}} \mathbf{H}_k P_{k-1}^{1/2} \\ \mathbf{0} & \frac{1}{\sqrt{\lambda}} P_{k-1}^{1/2} \end{bmatrix} \begin{bmatrix} I_n & \mathbf{0}^\top \\ \frac{1}{\sqrt{\lambda}} P_{k-1}^{\top/2} \mathbf{H}_k^\top & \frac{1}{\sqrt{\lambda}} P_{k-1}^{\top/2} \end{bmatrix} = \begin{bmatrix} \gamma_k^{-1/2} & \mathbf{0}^\top \\ K_k \gamma_k^{-1/2} & P_k^{1/2} \end{bmatrix} \begin{bmatrix} \gamma_k^{-1/2} & K_k^\top \gamma_k^{-1/2} \\ \mathbf{0}^\top & P_k^{\top/2} \end{bmatrix}, \tag{2-23}$$

where $\gamma = (I - \lambda^{-1} \mathbf{H}_k P_{k-1} \mathbf{H}_k^\top)^{-1}$. Note that each matrix in Equation 2-23 has a *triangular* structure. Next, we can use the following lemma.

**Lemma 2-4.1.** *Given two $n \times m$ ($n \leq m$) matrices $A$ and $B$, then $AA^\top = BB^\top$ if, and only if, there exists an $m \times m$ matrix $\Theta$ ($\Theta\Theta^\top = I_m$) such that $A = B\Theta$.*

The proof of this lemma can be found in [37, Chapter 21]. Using this lemma, we know that there should exist an orthogonal matrix $\Theta_k$ such that

$$\underbrace{\begin{bmatrix} I_n & \frac{1}{\sqrt{\lambda}} \mathbf{H}_k P_{k-1}^{1/2} \\ \mathbf{0} & \frac{1}{\sqrt{\lambda}} P_{k-1}^{1/2} \end{bmatrix}}_{A} \Theta_k = \underbrace{\begin{bmatrix} \gamma_k^{-1/2} & \mathbf{0}^\top \\ K_k \gamma_k^{-1/2} & P_k^{1/2} \end{bmatrix}}_{B}. \tag{2-24}$$

Note how the prearry $A$ only contains previous values $P_{k-1}^{1/2}$, while the postarray $B$ only contains the updated values $P_k^{1/2}$. We can thus compute the QR decomposition ([37, Chapter 21]) from the prearry for which the solution equals the lower triangular postarray. The command

in *MATLAB*, `qr` can be used to find the upper triangular postarray. Hence this command can be utilized by applying a transpose. From $B$, we can then derive the quantities $K_k$ and $P_k^{1/2}$. Positive definiteness of $P_k$ is guaranteed because the recursion propagates $P_k^{1/2}$ instead. Further mathematical background for this algorithm is also provided in [37, Chapter 21].

The square-root RLS algorithm initializes $P_{-1}^{1/2}$ and $\hat{x}_{-1}$, similar to the standard RLS algorithm. For each time step $k \geq 0$, the postarray is computed using a QR decomposition. From the solution, the covariance matrix is updated and the estimate is updated via:

$$\hat{x}_k = \hat{x}_{k-1} + (K_k \gamma_k^{-1/2})(\gamma_k^{-1/2})^{-1}(y_k - \mathbf{H}_k \hat{x}_{k-1}). \tag{2-25}$$

### 2-4-4 Converging to the Phase of the Helical Inflow

With the above-described algorithm, it is possible to extract the DC information from the output data. For Case 1 of Figure 2-4, this directly corresponds to the phase of the incoming helical wake. However, in Case 3, this output data corresponds to the sum of the bending moments caused by the helical wake plus the actuated helix method (Equation 2-7). For changes in the phase of the helical wake inflow $\theta_a$ and a fixed $\theta_b$, the estimated phase $\phi_k$ no longer equals $\theta_a$. Maximum helix wake amplification is, therefore, not guaranteed for all time steps $k$.

We can rewrite Equation 2-7 to a function of the phase $\phi$ as follows

$$\phi_k = \arctan\left(\frac{a\sin(\theta_a) + b\sin(\theta_b)}{a\cos(\theta_a) + b\cos(\theta_b)}\right). \tag{2-26}$$

For the control scheme, we need to pick a $\theta_b$ such that $\phi_k \to \theta_a$. A heuristic choice is $\theta_b = \phi_{k-1}$. This results in

$$\phi_k = \arctan\left(\frac{a\sin(\theta_a) + b\sin(\phi_{k-1})}{a\cos(\theta_a) + b\cos(\phi_{k-1})}\right), \tag{2-27}$$

which now is in the form of a nonlinear difference equation. One of the equilibrium points of this nonlinear system equals $\bar{\phi} = \theta_a$ which is stable as the absolute value of the derivative of Equation 2-27 evaluated at this equilibrium point is less than 1. The proof of this and the stability analysis of the combined RLS and nonlinear difference equation is given in Chapter 5. Furthermore, as was pointed out in Section 2-3-1, the optimal azimuth offset $\psi_0$ needs to be added to the phase of the helix control input to correct for coupling and the actuator delay.

### 2-4-5 RLS Controller Scheme

The final controller scheme for the RLS-based helix wake synchronization is given in Figure 2-8. The helical wind inflow is given by $V_k^u = V_k^p + w_k$, which contains the periodic signal $V_k^p$ and noise $w_k$. The control input $u_k$ equals the CCW helix tilt and yaw pitch angles with amplitude $a_{Helix}$, frequency $\omega_e$, and phase $\phi + \psi_0$. The output $y_k$ contains the individual blade bending moments with noise $v_k$. These are multiplied with a Park transformation for the $+1^{\text{st}}$ and $0^{\text{th}}$ (Clarke) harmonics according to Equation 2-16 to get $M_{\alpha\beta}$. This is used together with $\mathbf{H}_k$ to estimate the DC offset $\hat{M}_{dq}^0$ via the square-root RLS algorithm. Since other harmonics

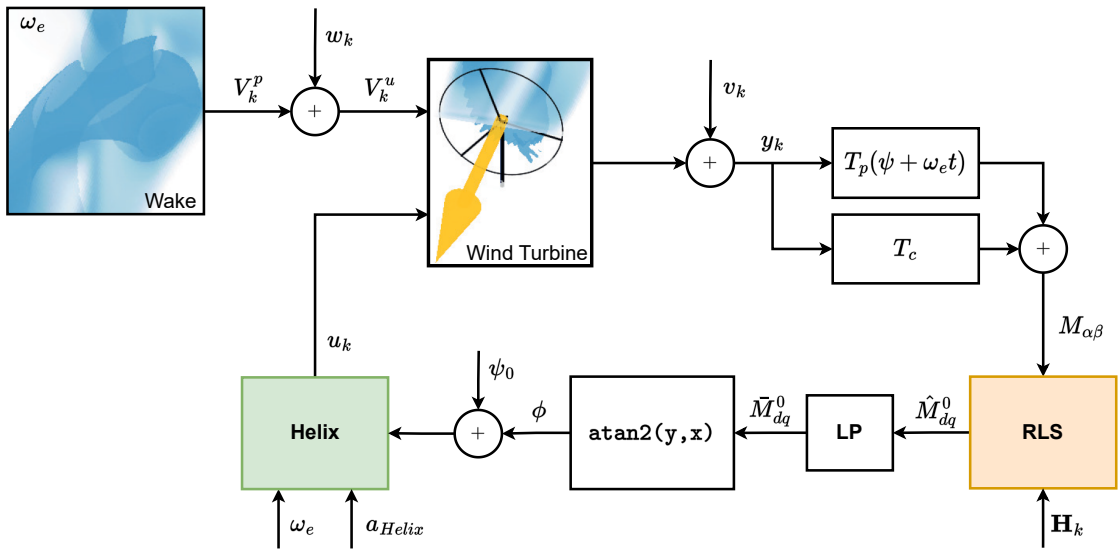



**Figure 2-8:** Proposed controller diagram for helix wake synchronization via an RLS estimator in a downstream turbine. The wake is modeled as an input to the wind turbine system with a periodic component $V_k^{\mathrm{p}}$ and known frequency $\omega_e$. A summation of the Park and Clarke transformed output $y_k$ is used as input to the square-root RLS estimator. The resulting estimate is filtered through a low-pass filter, after which the phase $\phi$ is computed. To correct for coupling and actuator delays, the optimal azimuth offset $\psi_0$ is added before the phase estimate is used for employing the helix method.

are still partly present in this estimate, a first-order low-pass filter with a passband frequency of $\omega_e$ can be added at this stage. This does not result in delays in the frequency range of interest, but it does result in a smoothed final estimate. Finally, the phase $\phi$ can be computed via Equation 2-18. This concludes the design and explanations of the RLS-based controller. The following section will elaborate on the derivation and algorithm of the second controller scheme, which is the Kalman filter-based estimator.

## 2-5 Kalman Filter-Based Estimator

The RLS-based estimator has the advantage of being easy to implement while also being adaptive to changes in the dynamics of the wind turbine. One downside is the fact that it does not directly estimate the phase of the helical wake, but rather the combined phase of the wake inflow and the controller effort. The convergence of the phase $\phi$ to the phase of the helical inflow $\theta_a$, presented in Equation 2-27, is also not suited for minimum helix wake amplification, described by $\theta_b = \theta_a - \pi$. This will be further explained in Chapter 5. The phase of the helical wake inflow can be estimated directly if information about the control input and the system dynamics are included in the estimation as well. In [44], a KF was implemented to estimate components of the incoming wind inflow to derive the effective wind speed at the hub height of a wind turbine. This work, however, modeled dynamics as a random walk, which is less suited to estimate the periodic components of the helical wake. A more suitable approach is presented in [45], where periodic dynamics are augmented in the state space of

the system in the context of modal analysis. In this section, a Kalman filter-based estimator will be presented to achieve helix wake synchronization, which is based on [46]. The first part will explain how the incoming helical wake can be modeled as a periodic disturbance on the control input. The KF incorporates this periodic disturbance as an augmented state that can be estimated. The second part explains the algorithm itself, and the last part summarizes the complete control scheme.

### 2-5-1 Augmenting the Helical Disturbance

In contrast to the RLS estimator, the periodic components of the helical wake inflow will be modeled as a disturbance on the control input. This allows the disturbance to be included as an augmented state in our system. Moreover, it alleviates the trouble of correcting for the optimal azimuth offset, as this fictitious input disturbance is measured as a pitch angle. We, therefore, do not have to translate the phase of the measured bending moments back to a phase that can be applied for pitch actuation. This augmentation of the periodic disturbance in the system dynamics is possible because of its stationarity. The Kalman filter does require a linear state-space of the wind turbine. The linearization for the KF will be further explained in Chapter 4. A continuous-time linearized model of the dynamics of the wind turbine with the inclusion of the helical input disturbance can be described by

$$\begin{aligned} \dot{x}(t) &= Ax(t) + B^{\mathrm{c}}u^{\mathrm{c}}(t) + B^{\mathrm{u}}u^{\mathrm{u}}(t) + w(t), \\ y(t) &= Cx(t) + D^{\mathrm{c}}u(t) + D^{\mathrm{u}}u^{\mathrm{u}}(t) + v(t). \end{aligned} \tag{2-28}$$

Here, $u^{\mathrm{c}}(t)$ is the control input, which should at least contain the tilt and yaw pitch angles. The helical input disturbance is included in $u^{\mathrm{u}}(t)$, where the superscript $\mathrm{u}(t)$ denotes uncontrolled inputs. The output $y(t)$ should at least contain the tilt and yaw bending moments of the blades. The variables $w(t)$ and $v(t)$ are the process and measurement noises respectively. It is assumed that the periodic component of the wind inflow can be described by

$$u^{\mathrm{p}}(t) = \begin{bmatrix} a\sin(\omega_e t + \theta_a) \\ a\cos(\omega_e t + \theta_a) \end{bmatrix}, \tag{2-29}$$

which corresponds to a tilt and yaw pitch disturbance at frequency $\omega_e$ with phase shift $\theta_a$ and amplitude $a$. This is similar to the disturbance described in Equation 2-7, although, here it is measured as an angle instead. Likewise, it is assumed that the knowledge about frequency $\omega_e$ is available. Next, the input disturbance is modeled as a state $x^{\mathrm{p}}(t) = u^{\mathrm{p}}(t)$ with the following dynamics

$$\dot{x}^{\mathrm{p}}(t) = \begin{bmatrix} \omega_e a\cos(\omega_e t + \theta_a) \\ -\omega_e a\sin(\omega_e t + \theta_a) \end{bmatrix} = \underbrace{\begin{bmatrix} 0 & \omega_e \\ -\omega_e & 0 \end{bmatrix}}_{A^{\mathrm{p}}} x^{\mathrm{p}}(t). \tag{2-30}$$

Equation 2-30 can be augmented in to Equation 2-28 and rewritten as:

$$\begin{aligned} \begin{bmatrix} \dot{x}(t) \\ \dot{x}^{\mathrm{p}}(t) \end{bmatrix} &= \begin{bmatrix} A & B^{\mathrm{p}} \\ 0 & A^{\mathrm{p}} \end{bmatrix} \begin{bmatrix} x(t) \\ x^{\mathrm{p}}(t) \end{bmatrix} + \begin{bmatrix} B^{\mathrm{c}} \\ 0 \end{bmatrix} u^{\mathrm{c}}(t) + \begin{bmatrix} w(t) \\ 0 \end{bmatrix}, \\ y(t) &= \begin{bmatrix} C & D^{\mathrm{p}} \end{bmatrix} \begin{bmatrix} x(t) \\ x^{\mathrm{p}}(t) \end{bmatrix} + D^{\mathrm{c}}u^{\mathrm{c}}(t) + v(t), \end{aligned} \tag{2-31}$$

Note that as the disturbance acts on the control input, the control input gain matrix $B^{\mathrm{c}}$ and the feed-through gain matrix $D^{\mathrm{c}}$ is used instead of $B^{\mathrm{u}}$ and $D^{\mathrm{u}}$ respectively. The unmodeled dynamics of the wake are assumed to be captured as noise on the input. The continuous time model presented in Equation 2-31 is discretized, which results in:

$$\begin{aligned} \begin{bmatrix} x_{k+1} \\ x^{\mathrm{p}}_{k+1} \end{bmatrix} &= \underbrace{\begin{bmatrix} A_d & B^{\mathrm{p}}_d \\ 0 & A^{\mathrm{p}}_d \end{bmatrix}}_{\mathbf{A}} \underbrace{\begin{bmatrix} x_k \\ x^{\mathrm{p}}_k \end{bmatrix}}_{\mathbf{x}_k} + \underbrace{\begin{bmatrix} B^{\mathrm{c}}_d \\ 0 \end{bmatrix}}_{\mathbf{B}} u^{\mathrm{c}}_k + \begin{bmatrix} w_k \\ 0 \end{bmatrix}, \\ y_k &= \underbrace{\begin{bmatrix} C_d & D^{\mathrm{p}}_d \end{bmatrix}}_{\mathbf{C}} \begin{bmatrix} x_k \\ x^{\mathrm{p}}_k \end{bmatrix} + \underbrace{D^{\mathrm{c}}_d}_{\mathbf{D}} u^{\mathrm{c}}_k + v_k, \end{aligned} \tag{2-32}$$

where $\{\mathbf{A}, \mathbf{B}, \mathbf{C}, \mathbf{D}\}$ represent the discrete-time state-space matrices of the augmented system. The augmented state is given by $\mathbf{x}_k$ for each time step $k$.

## 2-5-2 Kalman Filter Estimation of the Helical Input Disturbance

The model presented in Equation 2-32 will be rewritten in a *innovation form representation*. This will include a sequence of innovations $e_k = y_k - \mathbf{C}\hat{\mathbf{x}}_k$, which is considered to be a zero-mean white-noise sequence. Using a Kalman filter, this innovation sequence can be used to estimate an unbiased state estimate with minimum-error variance (see e.g. [47, Chapter 5]). The innovation form is given by:

$$\begin{aligned} \hat{\mathbf{x}}_{k+1} &= \mathbf{A}\hat{\mathbf{x}}_k + \mathbf{B}u^{\mathrm{c}}_k + K_k e_k, \\ y_k &= \mathbf{C}\hat{\mathbf{x}}_k + \mathbf{D}u^{\mathrm{c}}_k + e_k, \end{aligned} \tag{2-33}$$

where $\hat{(\bullet)}$ denotes an estimate, and $K_k$ is the Kalman gain. Here, it is assumed that the joint covariance matrix of the process noise $w_k$ and the measurement noise $v_k$ is known. The joint covariance matrix is given by

$$\begin{bmatrix} Q & S \\ S^\top & R \end{bmatrix} = \mathbb{E}\left[ \begin{bmatrix} w_k \\ v_k \end{bmatrix} \begin{bmatrix} w_j^\top & v_j^\top \end{bmatrix} \right] \geq 0, \quad \text{for } j = k, \tag{2-34}$$

with $R > 0$. For this application, we assume that the cross-term matrix $S = \mathbf{0}$. The optimal Kalman gain can be computed by solving the Ricatti difference equation. This gives the following update scheme for each time step $k$:

$$\begin{aligned} K_k &= \mathbf{A}P_{k-1}\mathbf{C}^\top(R - \mathbf{C}P_{k-1}\mathbf{C}^\top)^{-1}, \\ \hat{\mathbf{x}}_k &= \hat{\mathbf{x}}_{k-1} + K_k(y_k - \hat{y}_k), \\ P_k &= \mathbf{A}P_{k-1}\mathbf{A}^\top + Q - K_k\mathbf{C}P_{k-1}\mathbf{A}^\top, \end{aligned} \tag{2-35}$$

where $\hat{y}_k = \mathbf{C}\hat{\mathbf{x}}_k$ is the estimated output and $P_k$ is the updated covariance matrix. The augmented disturbance can be extracted from the estimated state $\mathbf{x}_k$. Note that Equation 2-35 and Equation 2-21 have a very similar structure. This is because the RLS algorithm can be viewed as a special case of the Kalman filter [48]. This will be further discussed in Chapter 5. The KF algorithm, therefore, suffers from the same positive definiteness issue as the RLS algorithm. A square-root implementation of the KF could thus also be implemented (see [47, Chapter 5]).

### 2-5-3 KF Controller Scheme

The controller scheme for the KF-based helix wake synchronization method is given in Figure 2-9. The Kalman filter takes both the blade tilt and yaw bending moments and tilt and yaw control pitch angles as input. The Kalman filter contains the discrete-time linearized state-space of the wind turbine required to estimate the periodic wake disturbance $u_k^{\mathrm{p}}$. This estimate is in the form of Equation 2-29. Hence, it is transformed with $T_{dq}(\omega_e t)$ to remove the $\omega_e$ frequency component. The resulting quantity $u^{\theta_a}$ contains the information about the phase of the helical disturbance. Similarly to Figure 2-8, the phase is computed using the

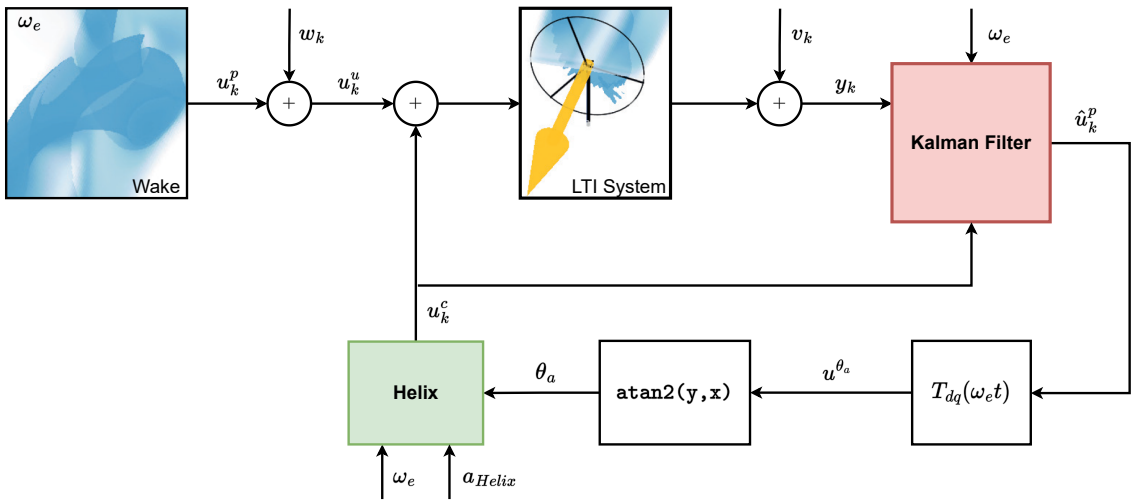



**Figure 2-9:** Controller diagram for helix wake synchronization via a KF-based estimator in a downstream turbine. The wake is modeled as a disturbance on the control input, containing a periodic component $u_k^{\mathrm{p}}$ and known frequency $\omega_e$. A load disturbance $w_k$ is also considered to be added. The output $y_k$ contains measurement noise $v_k$ and is used together with the control input $u_k^{\mathrm{c}}$ to the Kalman filter. The estimated disturbance states are rotated using a $T_{dq}(\omega_e t)$ transformation. The phase of the helical disturbance $\theta_a$ is computed via the inverse tangent of this estimate. This phase can directly be used for synchronization with the wake.

inverse tangent via `atan2(y,x)`. As was pointed out earlier, the KF-based estimator directly estimates the phase $\theta_a$ instead of $\phi$. We, therefore, do not need to correct for coupling between the tilt and yaw control angles and actuator delays. At this point, it is also possible to subtract any phase in $[-\pi, \pi]$ from $\theta_a$ without jeopardizing the stability of the system. Destructive helix wake interference via $\theta_b = \theta_a - \pi$ is therefore a viable option.

## 2-6 Concluding Remarks on the Controller Strategy

This chapter introduced the preliminaries for helix wake synchronization and presented the design of two different controller strategies. The preliminaries include the different reference frames that can be used to analyze the helix method, including the widely used MBC transformation. The interactions between an incoming helical wake and a downstream turbine were also discussed and formed the basis for which helix wake synchronization could be achieved.

The concepts of the optimal azimuth offset and a measure of sensitivity in the phase were discussed, as these are two concerns for implementing helix wake synchronization. Different controller options were listed which could be used for either in-phase helix synchronization or helix wake rejection. As this thesis is interested in both methods, both the RLS and the KF were chosen as adaptive filters for the estimation of the phase. The model-free RLS offers ease of implementation, while the model-based KF is able to achieve accurate estimates for both in-phase synchronization and out-of-phase rejection. The next chapter will test both controller implementations in a low-order model. This will help uncover the limitations of both controllers before they are implemented in a high-order wind turbine model.

# Chapter 3

# Phase Synchronization in Low-Order Synchronous Machine

In this chapter, a simplified model of a Permanent Magnet Synchronous Machine (PMSM) is derived. Although a PMSM does not represent a wind turbine, as was explained in Section 2-1-1, synchronous machines can be analyzed from a $dq$ framework as well. The synchronous machine model will take two orthogonal inputs, the voltages, and outputs two orthogonal outputs, the currents. This is similar to a wind turbine system which maps tilt and yaw pitch angles to tilt and yaw blade bending moments. The goal, here, is to demonstrate the estimation and synchronization capabilities of the controllers presented in Chapter 2. Furthermore, these capabilities are tested against varying conditions, such as load disturbances and noise. Using a simple low-order model thus allows for studying the characteristics of both controllers in a controlled environment with known dynamics. The first section contains a description of the dynamics of the PMSM and the experimental setup. The results of these experiments are evaluated in the second part of this chapter. Finally, the results for both controllers are discussed.

## 3-1 Model Description

A PMSM is a brushless synchronous electric motor with permanent magnets as the inductor. The motor has high efficiency, a large torque-to-inertia ratio, and requires little maintenance. The PMSM can be controlled via a three-phase alternating current (AC), hence, it has three voltage inputs which are 120° out of phase. Using Equation 2-3, the system can be viewed from a $dq0$ frame of reference. Following the approach presented in [49] results in the set of differential equations presented in Equation 3-1. Similar approaches have been applied in [50], [51] for model predictive control purposes.

The equations are given by:

$$\begin{aligned} \frac{dI_d}{dt} &= \frac{1}{L_d}\left(v_d - RI_d + \omega_m L_q I_q\right), & \frac{d\omega_m}{dt} &= \frac{p}{J}\left(T_m - \frac{B_v}{p}\omega_m - T_L\right), \\ \frac{dI_q}{dt} &= \frac{1}{L_q}\left(v_q - RI_q - \omega_m L_d I_d - \omega_m \phi_{mg}\right), & T_m &= \frac{3}{2}p\left[\phi_{mg} I_q + (L_d - L_q) I_d I_q\right]. \end{aligned} \tag{3-1}$$

Here, $\omega_m$ is the electrical speed of the synchronous machine, which is related to the rotor speed via $\omega_m = p\omega_r$ where $p$ is the number of pole pairs. The $v_d$ and $v_q$ represent the input stator voltages in a $dq$ framework. Similarly, $I_d$ and $I_q$ are the direct and quadrature stator currents respectively. $T_L$ represented the load torque, which is assumed to be constant. In this application, the PMSM is assumed to be surface mounted, which implies that the $dq$-axis inductance satisfies $L_d = L_q$. From Equation 3-1 it can be seen that this simplifies the relationship of the electromagnetic torque to $T_m = \frac{3}{2}p\phi_{mg}I_q$. Other parameters that are assumed to be constant include the flux of the permanent magnet $\phi_{mg}$, the total moment of inertia $J$, the viscous coefficient $B_v$, and the stator resistance $R$. The differential equations presented in Equation 3-1 also contain the nonlinear terms $\omega_m I_d$ and $\omega_m I_q$. In this application, a linearized version will, therefore, be considered. The system is linearized around the state $x_0 = [I_{d0},\, I_{q0},\, \omega_{m0}]^\top$, where $I_{d0} = I_{q0} = 0$ and $\omega_{m0} = 0.1 \cdot 2\pi$ rad/s. The following first-order Taylor series can be used to approximate the nonlinear terms using the operating points:

$$\begin{aligned} \omega_m(t) I_d(t) &\approx \omega_{m0} I_{d0} + I_{d0}\left(\omega_m(t) - \omega_{m0}\right) + \omega_{m0}\left(I_d(t) - I_{d0}\right), \\ \omega_m(t) I_q(t) &\approx \omega_{m0} I_{q0} + I_{q0}\left(\omega_m(t) - \omega_{m0}\right) + \omega_{m0}\left(I_q(t) - I_{q0}\right). \end{aligned} \tag{3-2}$$

Substituting Equation 3-2 into Equation 3-1 gives a state-space model that can be written as

$$\begin{aligned} \dot{x}(t) &= Ax(t) + Bu(t) + w(t), \\ y(t) &= Cx(t) + v(t), \end{aligned} \tag{3-3}$$

where the following matrices are defined as

$$A = \begin{bmatrix} -\dfrac{R}{L_d} & \dfrac{\omega_{m0} L_q}{L_d} & 0 \\ -\dfrac{\omega_{m0} L_d}{L_q} & -\dfrac{R}{L_q} & -\dfrac{\phi_{mg}}{L_q} \\ 0 & -\dfrac{3p^2\phi_{mg}}{2J} & -\dfrac{B_v}{J} \end{bmatrix}, \quad B = \begin{bmatrix} \dfrac{1}{L_d} & 0 \\ 0 & \dfrac{1}{L_q} \\ 0 & 0 \end{bmatrix}, \quad C = \begin{bmatrix} 1 & 0 & 0 \\ 0 & 1 & 0 \end{bmatrix}. \tag{3-4}$$

**Table 3-1:** PMSM model parameters.

| Symbol | Description | Value |
|---|---|---|
| $p$ | Number of pole pairs | 2 |
| $L_d$, $L_q$ | Direct and quadrature inductances | $8 \cdot 10^{-1}$ mH |
| $\phi_{mg}$ | Flux of permanent magnet | 0.125 Wb |
| $J$ | Total moment of inertia | 2.35 kg cm$^2$ |
| $B_v$ | Viscous coefficient | $1.1 \cdot 10^{-4}$ |
| $R$ | Stator resistance | 3 Ω |

The state matrix is given by $A \in \mathbb{R}^{n \times n}$, the input matrix by $B \in \mathbb{R}^{n \times m}$ and the observation matrix by $C \in \mathbb{R}^{q \times n}$. The feed-through matrix is considered to be $D = 0$. The state vector is given by $x(t) = [I_d,\, I_q,\, \omega_m]^\top \in \mathbb{R}^n$, where $n = 3$, the input vector by $u(t) = [v_d,\, v_q]^\top \in \mathbb{R}^m$ with $m = 2$, and the output vector is given by $y(t) = [I_d,\, I_q]^\top \in \mathbb{R}^q$ with $q = 2$. Finally, $w(t) \in \mathbb{R}^n$ and $v(t) \in \mathbb{R}^q$ are the process and measurements noises respectively. A full list of the parameter values is given in Table 3-1. With this model description, we can move on to the next section, which discusses the experimental setup.

### 3-1-1 Experiment Setup

The model presented in Equation 3-3 and Equation 3-4 is discretized with a sampling time of $T_s = 0.01$ seconds. In these tests, it is assumed that the disturbance acts on the input such that $u_k = u_k^{\mathrm{c}} + u_k^{\mathrm{u}}$. Here, $u_k^{\mathrm{c}}$ and $u_k^{\mathrm{p}}$ represent the controllable and uncontrollable inputs respectively. The uncontrollable input consists of a periodic disturbance $u_k^{\mathrm{p}}$ and the process noise $w_k$. The periodic disturbance is in the same form as Equation 2-29 with phase $\theta_a$. Likewise, the controllable input only consists of sinusoidal signals similar to the inputs of the helix method with the estimated phase $\hat{\phi}$. Both signals have a known frequency of $\omega_e$, representing the excitation frequency. The controller setup used in this experiment is shown in Figure 3-1. Here, it can be seen that the PMSM takes the input from the input

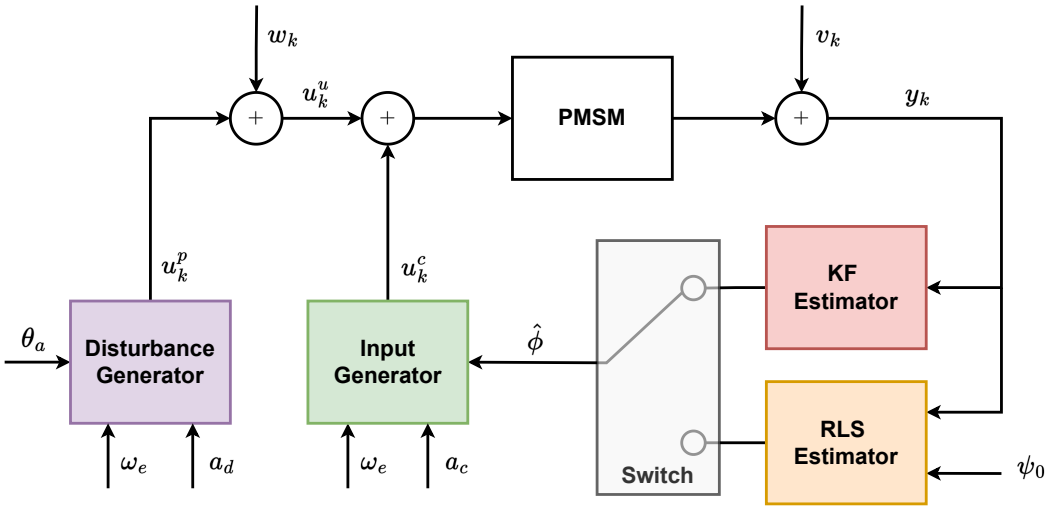



**Figure 3-1:** PMSM controller diagram. The system takes in the input $u_k$ which consists of the controllable and uncontrollable inputs $u_k^{\mathrm{c}}$ and $u_k^{\mathrm{u}}$ respectively. The uncontrollable input contains the periodic disturbance $u_k^{\mathrm{p}}$ and the noise $w_k$. Both the controllable input and the periodic disturbance have frequency $\omega_e$ with amplitude and phase $a_c$ and $\hat{\phi}$ or $a_d$ and $\theta_a$ respectively. Measurement noise $v_k$ is added to the output $y_k$. Both the Recursive Least Squares (RLS)- and Kalman Filter (KF)-based estimators use this output to compute $\hat{\phi}$. The RLS estimator takes in an azimuth offset $\psi_0$ to correct for actuator delays. The switch determines which estimate is used for the synchronization.

and disturbance signals generators. The corresponding output is fed into the RLS- and KF-based estimators, which both estimate the disturbance phase $\theta_a$. Note that the RLS estimator estimates this phase on the output side as was shown in Section 2-4, whereas the

KF estimates $\theta_a$ directly. To correct for the actuator delay, the RLS uses an azimuth offset $\psi_0$, which is computed via Equation 2-10. A switch is implemented to specify which estimate to use the synchronization. The experiment consists of three test cases, which are conducted in MATLAB. First, the reference tracking and disturbance rejection capabilities are tested. The second test investigates the convergence of the phase under the presence of noise. And finally, instead of synchronizing with the periodic disturbance, the controllers have to be partly or entirely out of phase with the periodic disturbance. The analysis of the results focuses mainly on simulations in the time domain and is presented in the next section.

## 3-2 Results Low-Order Model

Simulations of $T_{\max} = 1200$ seconds are run for each case and both control methods. The control input is activated at $T = 200$ seconds for every case. An example of a synchronized output without noise is shown in Figure 3-2 on the left. The output caused by the disturbance only is denoted by $y_d$. It can be seen that once the control input is turned on, the output $y$ increases in amplitude while remaining in phase with the disturbance. The increase in amplitude is due to the constructive interference of the amplitude of the control input and the periodic disturbance as described by Equation 2-7. Although the RLS-based estimator is

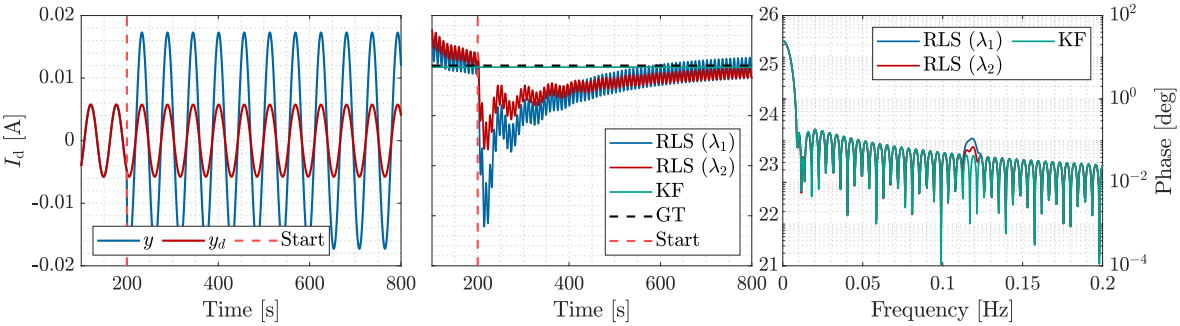



**Figure 3-2:** Example results of PMSM phase synchronization. **Left:** time domain result of a KF-based synchronization. The output is denoted by $y$ and $y_d$ represents the signal the output should be synchronized with. **Middle:** time domain result of the estimated phase for three different methods. The different controllers start synchronizing with the Ground Truth (GT) after $T = 200$ seconds. **Right:** Welch power spectrum estimate of the phase estimate result presented in the middle. Two peaks are visible at $\omega_e + \omega_{m0}$, which is the first harmonic of the RLS estimates.

model-free, besides picking the correct $\psi_0$, tuning of the parameter $\lambda$ is required as well. To accomplish this, Equation 2-20 is used and tested with two values of the number of samples. These are given by $N_1 = \frac{2\pi}{\omega_e Ts}$ and $N_2 = \frac{4\pi}{\omega_e Ts}$, which equal once and twice the number of samples in one period of $\omega_e$ respectively. A comparison of these two RLS estimates with the KF estimate and the GT is shown in the middle of Figure 3-2. A frequency domain comparison is shown on the right as well. From these results, it can be seen that the KF estimator has a Root-Mean-Square Error (RMSE) of 0.03° from the GT, which is $\theta_a = 25°$ at all time steps $k$. Because the RLS estimator does not have any information about the input, unlike the KF estimator, the estimate experiences a transient once the control input is turned on. For the RLS estimate with $\lambda_1$, the transient has a more considerate effect compared to $\lambda_2$. The reason is that estimation requires fewer samples and is therefore more susceptible to disturbances.

It is also less effective in removing the effect of harmonics, as was explained in Section 2-4-5. This results in a peak at $\omega_e + \omega_{m0}$. For $\lambda_1$, this peak is twice the magnitude of the peak for $\lambda_2$. For $\lambda_2$, the peak is $< 0.1°$ which does not affect the overall phase synchronization itself as can be deduced from Figure 2-7. For the same reason, the transient in the estimated phase of the RLS-based estimator does not affect the synchronization. These results highlight the differences between both controllers for a nominal plant without uncertainties. Both controller schemes are able to synchronize with the periodic disturbance. Under nominal conditions, the KF-based estimator has a more desirable performance due to the absence of noise and transients in the phase estimate. In the following experiments, both controllers are tested under different uncertain conditions.

### 3-2-1 Reference Tracking & Disturbance Rejection

The purpose of this test is to analyze the reference tracking and disturbance rejection capabilities of the two controllers. Reference tracking for the estimators is defined as tracking changes in the phase of the incoming periodic disturbance. For wind turbines, this could correspond to a change in the phase of the helical wake. Similarly, disturbances in the wind may cause the phase to change for a shorter period of time. In both scenarios, the change in phase is initiated at $T = 400$ seconds. In the reference tracking case, the phase $\theta_a$ experiences a step of $+10°$. Similarly, for the disturbance rejection case, the phase experiences a pulse of $+30°$ that lasts 30 seconds. The control action again starts at $T = 200$ seconds. The results are shown in Figure 3-3. From the left of this result, it can be seen that both controllers

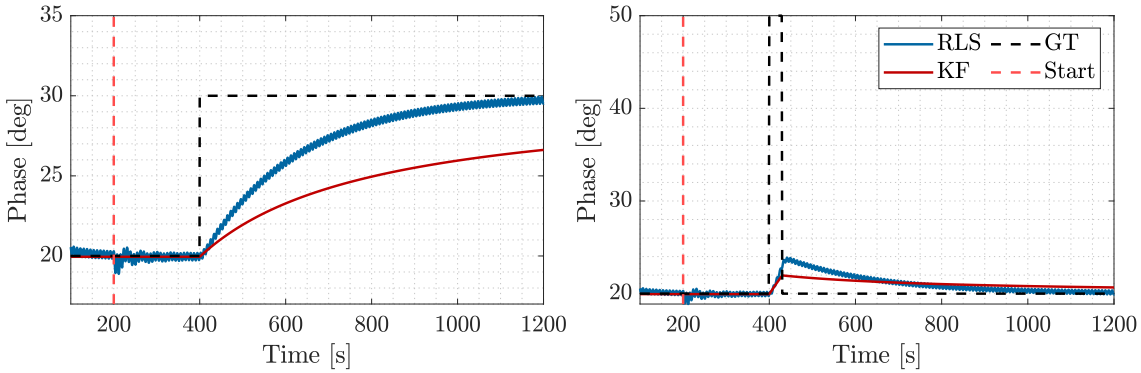



**Figure 3-3:** Time-domain simulation results of a step reference and a pulse disturbance. **Left:** step reference of $+10°$ starting at $T = 400$ s for both controllers. **Right:** pulse disturbance of $+30°$ also starting at $T = 400$. The red dashed line indicated the point where the controllers are switched on. The black dashed line represents the ground truth phase.

struggle to follow the step reference within a reasonable amount of time. Only the RLS-based controller is barely able to converge to the new phase within 10 minutes. This is because both implementations inherently assume the estimate to have no dynamics. The RLS estimates the DC offset of the $T_p((\omega_{m0} + \omega_e)t)$ transformed output, which can only change fast if $\lambda$ is small. In that case, the state covariance matrix $P_k$ would forget past data more quickly. Likewise, by following the reasoning shown in Equation 2-30, it can be seen that $\theta_a$ is defined as constant. Looking at the right of Figure 3-3, this resistance to change becomes clear as well. The pulse of $30°$ causes the KF estimate to change by about $2°$ and the RLS estimate by

about 4°. It does, however, take several minutes to converge back to the ground truth. The error in the phase from the ground truth of these results can be compared with Figure 2-7. As the step in the phase is 10°, it is still within 99% of the maximum attainable interference. Likewise, the 4° phase error from the disturbance is well within this range.

It has to be noted, however, that this step reference and pulse disturbance in the phase might not represent realistic scenarios. Not much is currently known about changes in the phase of the helix method due to disturbances. The results presented above provide some insight into the behavior of the two controllers. As explained earlier, both controllers assume that the phase of the periodic disturbance is constant. Thus, the two controllers are resistant to a change in phase. Although the phase of the periodic disturbance was subject to changes, both controllers still operated under nominal conditions. In the next part, the uncertain conditions are further investigated by evaluating the effects of the Signal-to-Noise Ratio (SNR).

### 3-2-2 Effect of the Signal-to-Noise Ratio

The next experiment explores the effect of noise in the periodic disturbance signal defined by $w_k$ in Figure 3-1. The noise is defined as Pseudo-Random Binary Noise (PRBN) of different seeds with a clock period of 1 [52], which gives a flat power spectrum. To limit the frequency range of this spectrum, the signal is filtered through a bandpass filter with cut-in and cut-out frequencies of $10^{-3}$ and $10^{2}$ Hertz. The amplitude of $w_k$ is set to 20°, which is chosen to heavily distort the input signals $u_k^{\mathrm{p}}$ and $u_k^{\mathrm{c}}$. The control input has an amplitude of 3° while the periodic disturbance is tested for 1.5° and 0.5° respectively. This will result in two different SNR, which is the ratio of the power of the signal to the power of the noise. The idea here is that this represents the case of added turbulence in the wind, where over distance the amplitude of the helical wake may drop significantly with respect to the ambient wind. Both simulations are run for 2000 seconds and tested for the two controller schemes. These are initiated at $T = 200$ seconds. The results are shown in Figure 3-4.

The mean signal-to-noise ratio is denoted by $\bar{\mathrm{SNR}}$, which is the averaged sum of the SNRs of both controllers. The SNR is computed using the MATLAB function `snr` for the output $y_k$. This function selects the fundamental frequency, which for both experiments equals the excitation frequency $\omega_e$, and compares it to the power of the noise. The second experiment has a lower SNR due to the magnitude of the interference between the periodic disturbance and the control input being lower because of the lower amplitude of $u_k^{\mathrm{p}}$. From the top left of Figure 3-4, it can be seen that the two controllers manage to synchronize with the periodic disturbance reasonably well. The difference between both controller outputs is also minimal. This can also be seen on the right of Figure 3-4, where both phase estimates manage to converge to within ±10° of the ground truth phase. This can not be said for the second experiment, as the RLS estimate starts at roughly −15° which is well out of range for optimal synchronization. This is also evident in the lower left corner of Figure 3-4, where the peak values of both controllers do not align with the output caused by the periodic disturbance. Compared to the first experiment, the second experiment has a negative SNR meaning that there is more noise compared to the fundamental frequency.

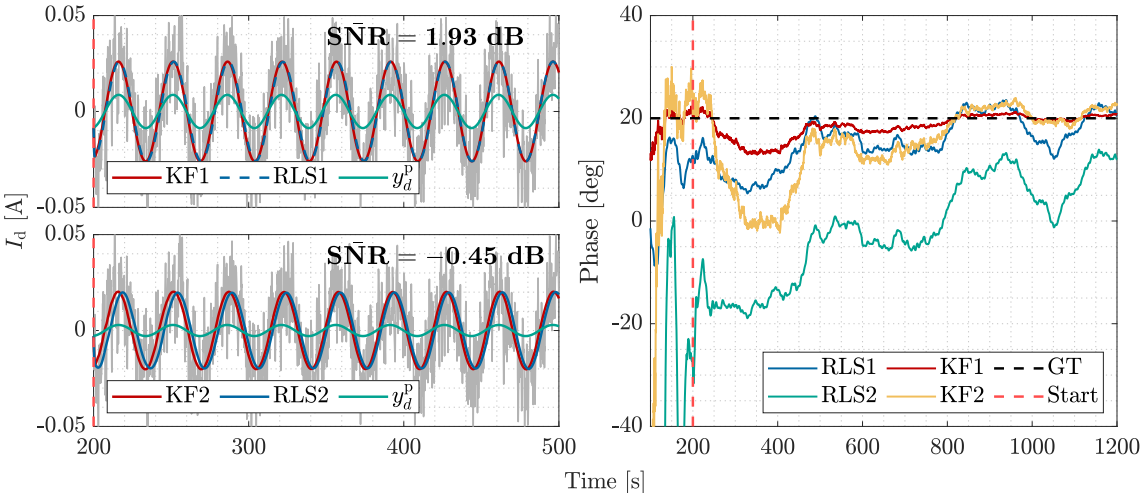



**Figure 3-4:** Time-domain results for two experiments with different SNRs due to added noise. **Left:** Output $I_\mathrm{d}$ of both controllers and experiments. KF1 and RLS1 represent the case where the amplitude of $u_k^\mathrm{p}$ equals $1.5°$. Likewise, KF2 and RLS2 are the cases for which the amplitude equals $0.5°$. Both signals are shown without noise and the original data is shown in gray. The signal $y_\mathrm{d}^\mathrm{p}$ is the part of the output caused by the periodic disturbance only. Hence, it represents the signal the controller should synchronize with. The mean SNR is depicted in the top right corner of each figure. **Right:** Phase estimates for each case over a time period of 1200 seconds. The ground truth is denoted with a dashed black line.

### 3-2-3 Out-of-Phase Disturbance Rejection

In Section 2-2 and Section 2-5-3 it was briefly mentioned that besides maximum interference, minimal interference via $\theta_b = \theta_a - \pi$ would be interesting as well. For wind turbines, in-phase and (partially) out-of-phase wake synchronization could have different effects in terms of fatigue loads, power production, or wake mixing in general. Both fully and partially out-of-phase synchronization is, therefore, tested. The former corresponds to $\theta_b = \theta_a - \pi$, whereas the latter equals $\theta_b = \theta_a - \frac{\pi}{2}$. The phase of the periodic disturbance is $\theta_a = 20°$ and on top of that, a pulse of $+10°$ disturbs the system at $T = 400$ seconds which lasts for 30 seconds. This disturbance is added as both set points are unstable equilibrium points of Equation 2-27. Hence, the disturbance helps to demonstrate this. The results of both out-of-phase methods are shown in Figure 3-5. Here, the left shows the partially out-of-phase method, and the right the fully out-of-phase method. The KF-based controller scheme has no trouble following the two different references. Even with the small disturbance added, the KF estimate stays within $< 1°$ of the ground truth. However, this can not be said for the RLS-based controller scheme. For the partially out-of-phase method, the RLS estimate $\phi$ becomes periodic. For the fully out-of-phase method, the RLS estimate has a reasonable performance up until the disturbance is added. This is because $\theta_b = \theta_a - \pi$ is a stable equilibrium point of Equation 2-27, although its region of attraction is not large enough for this small disturbance. Because of this, the estimate becomes unstable once the disturbance is applied. Both phenomena of the RLS estimator will be further explained in Chapter 5. It can be concluded that the KF has good performance for both partially and fully out-of-phase synchronization with an incoming wake. The RLS estimator in tandem with Equation 2-27 lacks this performance.

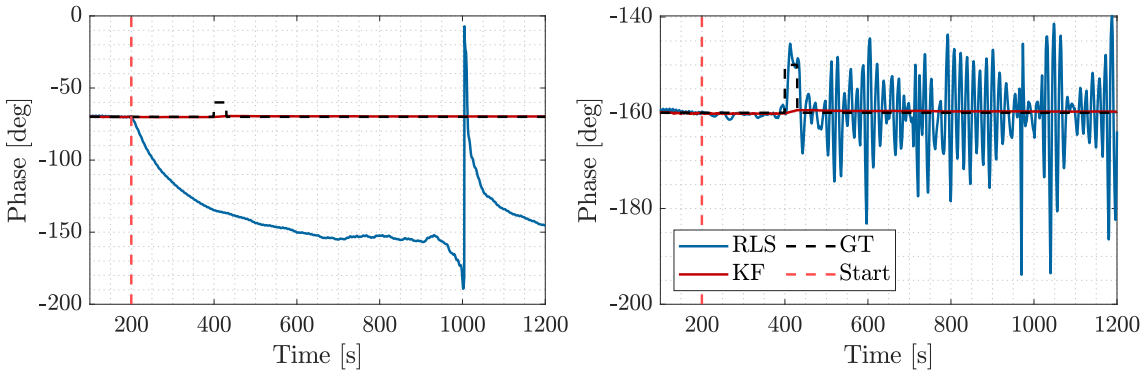



**Figure 3-5:** Time-domain simulation results of partial and complete out-of-phase synchronization. **Left:** Partially out-of-phase synchronization by setting $\theta_b = \theta_a - \frac{\pi}{2}$ starting at $T = 400$ s for both controllers. **Right:** Completely out-of-phase synchronization by setting $\theta_b = \theta_a - \pi$ starting at $T = 400$ s. The red dashed line indicated the point where the controllers are switched on. The black dashed line represents the ground truth phase. At $T = 400$ a pulse disturbance is added of $+10°$ for both experiments.

## 3-3 Concluding Remarks Low-Order Model

The results presented in this chapter demonstrate the behavior of both controllers under certain and uncertain conditions. In all experiments, the KF-based estimator showed the best performance, as its phase estimation consistently had a minimal error with the ground truth compared to the RLS-based estimator. Only its reference tracking capabilities were poor compared to the RLS method, however, it remains questionable whether this is a valid test. The results presented in Figure 3-4 and Figure 3-5 give a good insight into the limits of the RLS-based estimator. Under low SNR conditions, this estimator has a large error with respect to the ground truth. This is because the RLS estimator does not take into account noise or information about the control input signal itself. The convergence of the phase through Equation 2-27 is also not suited for partial or full out-of-phase synchronization. This will be further explained in Chapter 5. What is missing from these experiments is the behavior of the KF-based estimator under model miss-matches. It is likely that this will result in worse performance. Since this is not included, the KF-based estimator is not used under uncertain plant conditions and the RLS method is used instead. The next chapter will present the simulation setups and experiment results for the helix wake synchronization for a downstream wind turbine.

# Chapter 4

# Helix Synchronization in High-Order Wind Turbine Models

The previous chapter looked at the behavior of the two controller schemes under different conditions in a controlled simulation environment for a low-order system. The results highlighted some limitations of both controllers while also showing that both are capable of estimating the phase of a periodic disturbance with reasonable accuracy. To this end, the two methods are implemented in three different simulation tools for helix wake synchronization in a waked downstream turbine. This chapter consists of two main parts. The first part will introduce the reference turbine and elaborate on the simulation setup of each simulation tool. The first simulation environment is OpenFAST where one turbine will be simulated for various wind inflows with helical features. After this, we move up in simulation fidelity, as the setup for both QBlade and SOWFA will be explained. The second part of this chapter discusses the results of all three simulation environments. This part is divided into the results of the low- and high-fidelity models, similar to the first part of this chapter. All results are summarized at the end of the chapter.

## 4-1 NREL 5-MW Reference Wind Turbine

In this section the reference turbine model itself and the linearization process will be explained. The wind turbine model that has been used during this thesis is the *NREL 5-MW* baseline wind turbine [53]. The model is based on manufactured offshore wind turbines in the 5-megawatt range. Although the industry is moving towards larger wind turbines (see e.g. [54]), the *NREL 5-MW* is still widely used in the field of wind energy. For this thesis, it was selected over bigger reference wind turbines, such as the *IEA 15-MW*, because of its model availability for both OpenFAST and QBlade. In Table 4-1, a list of parameters of the reference turbine is given. As dynamic wake mixing strategies are mainly aimed at below-rated wind conditions, due to more significant power losses compared to above-rated conditions [24], all experiments with the *NREL 5-MW* are conducted in this region as well. For this reason,

**Table 4-1:** Specifications of the *NREL 5-MW* reference turbine. Adapted from [53].

| Description | Value |
|---|---|
| Rated Power | 5 MW |
| Rotor Orientation, Configuration | Upwind, 3 Blades |
| Control | Variable Speed, Collective Pitch |
| Drivetrain | High Speed, Multiple-Stage Gearbox |
| Rotor Diameter | 126 m |
| Hub Height | 90 m |
| Cut-In, Rated, Cut-Out Wind Speeds | 3 m/s, 11.4 m/s, 25 m/s |
| Cut-In, Cut-Out Rotor Speed | 6.9 rpm, 12.1 rpm |
| Rated Tip Speed | 80 m/s |
| Max Pitch Rate | 8°/s |

the Baseline (BL) control case is defined as a $k\omega_g^2$ torque controller which maximizes the power via the squared generator speed $\omega_g$ in rad/s and a constant gain $k = 2.3323$. The generator speed is filtered through a low-pass filter before it is used for control. The baseline controller also has a static pitch of 0.106°. Besides this pitch offset, the baseline controller does not perform the helix method or Individual Pitch Control (IPC). The Recursive Least Squares (RLS) and Kalman Filter (KF) based controllers run a baseline controller as well but include the helix wake synchronization on top of that. For each experiment in this chapter, the synchronization controllers are always compared to a downstream turbine with a baseline controller. The next part will derive the linearized model of the *NREL 5-MW* turbine. This is required for the KF itself and to determine the optimal azimuth offset $\psi_0^*$ for the RLS estimator.

### 4-1-1 MBC Transformed Linearized Wind Turbine Model

The KF-based estimator requires a linear model of the *NREL 5-MW* turbine for its estimates. Likewise, a linear system can be used to get a good estimate of the optimal azimuth angle. Wind turbine systems are highly nonlinear because of their rotating nature and variable speed. Hence, the nonlinear system has to be linearized around certain operating points. Linearizing around a fixed rotor and wind speed does, however, not yet result in a Linear Time-Invariant (LTI) system because the system still has a rotating nature. This would result in a Linear Parameter-Varying (LPV) system, where the system dynamics are dependent on the rotor azimuth angle $\psi$. To reduce this periodicity, the Multi-Blade Coordinate (MBC) transformation can be utilized once more, as was explained in Chapter 2. This is because the dynamics can be transformed into a non-rotating reference frame. Secondly, we are interested in the MBC-transformed dynamics between the tilt and yaw pitch angles and the tilt and yaw blade bending moments. Hence, the resulting linearized system is also in the desired reference frame for helix wake synchronization.

OpenFAST can be used to linearize the *NREL 5-MW* turbine around given operating points. The system is, therefore, linearized around a constant rotor speed for different steady wind speeds at 36 azimuth positions. The azimuth positions are separated by 10° each. The different wind speeds range from 5 to 9 m/s, with 1 m/s between wind speed linearization points. This range is chosen such that there is a model available for every different turbine

distance of the downstream turbine, where it experiences lower average wind speeds. The average wind speed in the rotor plane also lies within this range for distances $3D$ to $6D$. On top of that, these wind speeds are all below the rated wind speed. The linearization results in the following state-space:

$$\begin{aligned} \dot{x} &= A(\psi)x + B(\psi)u, \\ y &= C(\psi)x + D(\psi)u, \end{aligned} \tag{4-1}$$

where the state vector $x$ contains a number of degrees of freedom of the system and their derivatives, and $u$ and $y$ are the input and output vectors respectively. The matrices $A(\psi)$, $B(\psi)$, $C(\psi)$, and $D(\psi)$ are the linear parameter varying state, control input, output, and feedthrough matrices respectively. The vectors $x$, $u$, and $y$ are defined as perturbations from the operating points.

Next, the system matrices and vectors can be transformed from a rotating reference framework to a non-rotating framework. In MATLAB this can be done by utilizing the command `fx_mbc3` (or the older `mbc3` command) from the *OpenFAST Toolbox* [31]. This results in 36 linearized state-space models which are in a non-rotating reference framework. This is given by:

$$\begin{aligned} \dot{x}_{\mathrm{NR}} &= A_{\mathrm{NR}}(\psi)x_{\mathrm{NR}} + B_{\mathrm{NR}}(\psi)u_{\mathrm{NR}}, \\ y_{\mathrm{NR}} &= C_{\mathrm{NR}}(\psi)x_{\mathrm{NR}} + D_{\mathrm{NR}}(\psi)u_{\mathrm{NR}}, \end{aligned} \tag{4-2}$$

where the subscript NR denotes that the vectors elements are non-rotating. Going from Equation 4-1 to Equation 4-2 can be described by the following set of relations:

$$\begin{aligned} A_{\mathrm{NR}}(\psi) &= \begin{bmatrix} T_1^{-1} & 0 \\ 0 & T_1^{-1} \end{bmatrix} \left( A(\psi) \begin{bmatrix} T_1 & 0 \\ \omega_r T_2 & T_1 \end{bmatrix} - \begin{bmatrix} \omega_r T_2 & 0 \\ \omega_r^2 T_3 + \dot{\omega}_r T_2 & 2\omega_r T_2 \end{bmatrix} \right), \\ B_{\mathrm{NR}}(\psi) &= \begin{bmatrix} T_1^{-1} & 0 \\ 0 & T_1^{-1} \end{bmatrix} B(\psi) T_{1C}, \\ C_{\mathrm{NR}}(\psi) &= T_{1O}^{-1} \begin{bmatrix} C_1(\psi)T_1 + \omega_r C_2(\psi)T_2 & C_2(\psi)T_1 \end{bmatrix}; \qquad C(\psi) = \begin{bmatrix} C_1(\psi) & C_2(\psi) \end{bmatrix}, \\ D_{\mathrm{NR}}(\psi) &= T_{1O}^{-1} D(\psi) T_{1C}. \end{aligned} \tag{4-3}$$

The detailed derivation of Equation 4-3 is given in [23], [31]. The transformation matrix $T_1$ can be built with Equation 2-6 and the appropriate sizes for the number of degrees of freedom that are in the system. Likewise, $T_2$ and $T_3$ consist of first and second derivative terms of Equation 2-6 respectively. $T_{1C}$ and $T_{1O}$ are very similar to $T_1$, except their sizes match the number of control inputs and a number of outputs. A full derivation and description of these matrices are given in Appendix B.

It was mentioned before that the MBC transform reduces the periodic nature of the rotor frequency. However, the azimuth angle is still present in the transformation matrices. This does not result in an LTI system, as other time-varying components (e.g. the $3P$ frequency) are still present. The azimuth angle and rotor speed, therefore, still affect this system. Fortunately, the set of non-rotating models can be averaged to approximate an LTI system because the periodicity is reduced [55]. Averaging the non-rotating state, control, output,

and feedforward matrices from Equation 4-3 over their 36 different linearizations, gives the following approximate LTI system:

$$\begin{aligned} \dot{x}_{\text{NR}} &= \bar{A}_{\text{NR}} x_{\text{NR}} + \bar{B}_{\text{NR}} u_{\text{NR}}, \\ y_{\text{NR}} &= \bar{C}_{\text{NR}} x_{\text{NR}} + \bar{D}_{\text{NR}} u_{\text{NR}}, \end{aligned} \tag{4-4}$$

where $(\bar{\bullet})$ denotes an averaged matrix. As we are only interested in the mapping from the tilt and yaw pitch angles to the tilt and yaw blade bending moments, we can define $u_{\text{NR}} = [\theta_{\text{tilt}}, \theta_{\text{yaw}}]^\top$ and $y_{\text{NR}} = [M_{\text{tilt}}, M_{\text{yaw}}]^\top$. Equation 4-4 can therefore be written as a $2 \times 2$ transfer function $G(s)$, where $s$ is the Laplace variable. The Bode magnitude diagram of this transfer function is shown in Figure 4-1 below. From this diagram, we can find that around

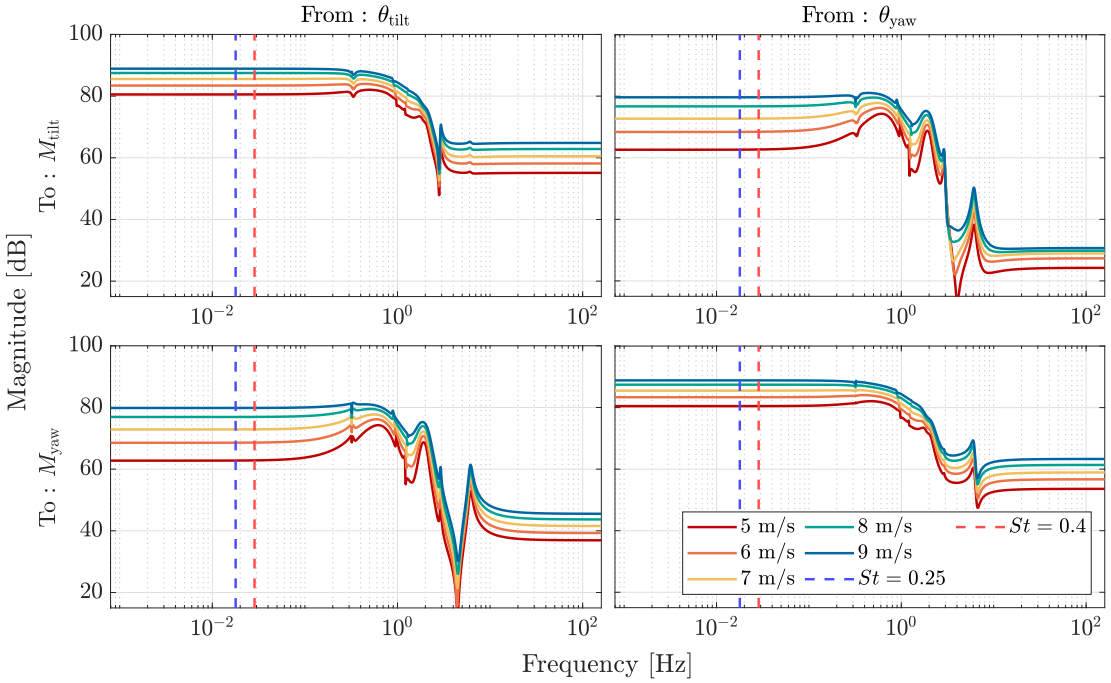



**Figure 4-1:** Bode magnitude diagrams of the MBC-transformed linearized *NREL 5-MW* system $G(s)$. This multivariate transfer function maps the tilt and yaw pitch angles, $\theta_{\text{tilt}}$ and $\theta_{\text{yaw}}$ respectively, to the tilt and yaw blade bending moments, $M_{\text{tilt}}$ and $M_{\text{yaw}}$. Different linearizations are shown for operating points ranging from 5 to 9 m/s wind speeds. The excitation frequencies $f_e$ of the upstream turbine are indicated by the vertical dashed lines for an ambient wind speed of $U_\infty = 9$ m/s and Strouhal numbers $St = 0.25$ (blue) and $St = 0.4$ (red).

the excitation frequencies for $St = 0.25$ and $St = 0.4$, the linearizations have similar dynamics but with a higher gain for higher wind speeds. These linearized models are used for the KF-based estimator with Equation 2-32 for the known wind speeds. Note that the linearized system is implemented based on the velocity deficit at T2 and not based on the ambient wind speed. Figure 4-1 is also used to get an estimate of the azimuth angle for the RLS method. We find that at both excitation frequencies, $G(s)$ can be viewed as a symmetric system. Hence, Equation 2-10 is used to compute the azimuth offsets for the different wind speeds and Strouhal numbers. These values are shown in Table 4-2. With the linearized models and azimuth offsets, the controllers can be implemented for the *NREL 5-MW* reference turbine. The next two sections will elaborate on the simulation setups for the different experiments.

**Table 4-2:** Estimated optimal azimuth offsets $\psi_0$ for Strouhal numbers $St = 0.25$ and $St = 0.4$. The offset is chosen as the $\psi_0 = -\psi_d$ via Equation 2-10, where $\psi_d$ is the phase lag at the excitation frequency.

| | **5 m/s** | **6 m/s** | **7 m/s** | **8 m/s** | **9 m/s** |
|---|---|---|---|---|---|
| $St = 0.25$ | $8.56°$ | $11.6°$ | $14.6°$ | $18.0°$ | $21.1°$ |
| $St = 0.4$ | $9.33°$ | $12.5°$ | $15.6°$ | $19.2°$ | $22.3°$ |

## 4-2 Low-Fidelity Simulation Setup: OpenFAST

In this section, the first simulation tool, OpenFAST, and the simulation setup will be explained for a one-turbine setting. This implies that only one *NREL 5-MW* is simulated. By customizing the wind input to this turbine, we can still run a simulation as if it were a waked downstream turbine. As only one turbine is simulated and the wind data is not generated within OpenFAST using Computational Fluid Dynamics (CFD) methods or alike, this simulation environment is considered to be low-fidelity. First, a brief explanation of OpenFAST will be given for some context. After this, this section will go into detail about the different wind inflow data sets that will be used for these low-fidelity experiments.

OpenFAST is a wind turbine simulation tool that is built upon the FAST (Fatigue, Aerodynamics, Structures, and Turbulence) v8 code [56]. This engineering tool is physics-based and can be used to simulate the coupled nonlinear dynamic response of wind turbines. OpenFAST combines different modules to simulate aerodynamics, hydrodynamics, on- and offshore structures, electrical and control systems, and their interactions. It is also able to simulate different kinds of wind turbines, such as two- or three-bladed horizontal-axis rotors, different tower, and hub configurations as well as fixed-bottom or floating substructures. Furthermore, the software can be extended with FAST.Farm to simulate multiple turbines and their wake. Unfortunately, FAST.Farm is not capable of simulating complex wake dynamics, such as required for dynamic wake mixing strategies. This is because it only captures a few key wake features, like wake meandering and wake-deficit evolution, to be computationally efficient. Helical structures in the wake can, therefore, not be simulated.

To predict the aerodynamics of the interaction between the horizontal-axis wind turbine and the wind inflow, OpenFAST uses the module *AeroDyn* [57]. This module uses Blade Element Momentum (BEM) theory to compute induced velocities on wind turbine blades [1]. On top of that, the structural dynamics of the blades are captured by the module *ElastoDyn*. This module can thus be used to compute the individual blade bending moments. Although OpenFAST can only simulate one turbine, it has modules that can handle complicated wind inflow data and translate it into individual blade bending moments. This means that it can be used to simulate a downstream turbine experiencing a helical wake without simulating the upstream turbine. To accomplish this, the wind inflow data must be adjusted such that it includes a periodically rotating pattern over time. How this will is done is explained in the next part.

### 4-2-1 TurbSim Custom Wind Inflow

TurbSim is a tool that can simulate stochastic, full-field, turbulent wind conditions [58]. It simulates a time series of three-dimensional wind speed vectors at points in a two-dimensional

vertical rectangular grid that is fixed in space. This grid field can be used as input to *AeroDyn* and thus OpenFAST. It is also possible to read and edit this output via MATLAB. This way the generated wind speed vectors can be overwritten by new ones. For the low-fidelity experiments in OpenFAST, TurbSim is only used for this very reason. In Section 4-3-1, TurbSim will also be used to simulate turbulent wind fields for one of the higher fidelity experiments. The following two parts will describe which settings have been used in TurbSim and how the output has been edited to create data useful for studying the helix wake synchronization in OpenFAST. The first data set is the rotating disc set, which is a simplified version of a helix wake. Here, the velocity deficit caused by the helical wake is represented by a disc that rotates in the rotor plane with the excitation frequency. This set is used to test both controllers in the high-order wind turbine as it has a very clean periodic signal compared to an actual helical wake. For the second data set, a helical wake from the high-fidelity simulation SOWFA is used to overwrite TurbSim data. This is a more accurate data set compared to the rotating disc, while also ensuring a low computation time. In the next part, the rotating disc data set is elaborated first.

### Rotating Disc

A simplified helical wind field is designed to test if customized TurbSim can be used as well as if both controller schemes presented in Chapter 2 can estimate a phase from the data. In TurbSim, an $18 \times 28$ grid with grid height 170.4 meter and grid width 255.6 meter is simulated. The reasoning behind these values will be given in Section 4-2-1. A first explanation is that the rotor diameter has to fit inside while also considering the hub height, both given in Table 4-1. All other settings are redundant as they are either overwritten or can be edited at a later stage. The data consists of $U, V, W \in \mathbb{R}^{n \times m \times k}$, where $n = 28$ is the number of grid points in the $Y$ direction, $m = 18$ is the number of grid points in the $Z$ direction and $k$ is the total number of time steps. The directions $X$, $Y$, and $Z$ are defined in the same way as shown in Figure 2-1. The vectors $U$, $V$, $W$ move along the positive $X$, $Y$, $Z$ respectively. For simplicity, $V$ and $W$ are set to 0 for all grid points and time steps. At each time step, $U$ is set to the ambient wind speed $U_\infty = 9$ m/s. Next, all grid points within the rotor diameter are set to half the ambient wind speed. And finally, the center of this area is rotated over time with a small radius such that the result in Figure 4-2 is achieved. This

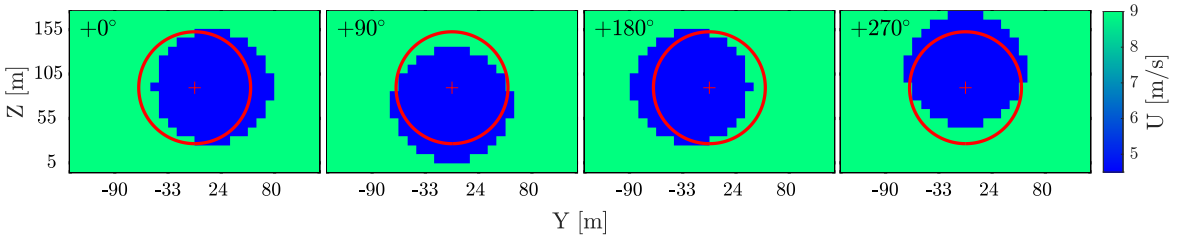



**Figure 4-2:** Rotating disc data sets with different initial phases. The ambient wind speed is set to 9 m/s and the velocity deficit area has a wind speed of 4.5 m/s. The hub height is at 90 meters and indicated with the red cross. The red circle represents the rotor diameter of the *NREL 5-MW* turbine. The point $Y = 0$ is located in the center of the x-axis. Similarly, $Z$ has a total length of 255.6 meter but starts at 4.8 meter.

rotating disc rotates in a Counter-Clockwise (CCW) fashion from the perspective of the wind

turbine with a period of $\omega_e$. For this data set, a Strouhal number of 0.4 was used resulting in $\omega_e \approx 0.18$ rad/s. The total number of time steps can either be set to a large number or to a number such that the rotation repeats itself. In total, four different rotating disc data sets are used in this report. Each is identically the same, except for the initial phase offset. These are in the set $\{+0°, +90°, +180°, +270°\}$, as also shown indicated in Figure 4-2. Both estimators should therefore estimate four different phases which are exactly 90° apart. The rotating disc data set serves as a controlled setting for the helix wake synchronization as it produces relatively clean blade bending moments due to its simplicity. Its simplicity is also its limitation as it is not representative of an actual helical wake. For this reason, the next part will describe the second data set used in OpenFAST, which uses helical data from CFD simulations.

### Helical Data

As it is possible to customize wind inflow data created via TurbSim, it is also possible to overwrite it with existing data from the helix method. The authors from [22], [24] provided data with $\{U, V, W\}$ velocity vectors within a three-dimensional grid field over time with a CCW helical velocity deficit. By taking a cross-section of this data in the $YZ$ plane, the same procedure as for the rotating disc can be applied. Moreover, the three-dimensional grid field can go up to $8D$. Therefore, it is even possible to generate slices of the helical structure at different rotor distances. This way, not only can a downstream turbine be simulated which experiences an incoming helical wake, but also the effect of turbine distance can be analyzed. A three-dimensional surface of the helical structure and the resulting cross-sections at $3D$ to $6D$ are shown in Figure 4-3. This volume of wind data is simulated using SOWFA, which is a high-fidelity simulation environment. SOWFA will be further explained in Section 4-3-2. One limitation is that this simulation was done for the *DTU 10-MW* reference turbine instead of the *NREL 5-MW*. This wind field is therefore scaled for the *DTU 10-MW* turbine, which has a rotor diameter of 178.3 meter. The grid width and height, therefore, have to be scaled to match with the *NREL 5-MW*. Due to the fact that this SOWFA simulation took a significant amount of time, the grid sizes were chosen to be smaller to save on simulation time. The grid sizes equal $m = 25$ and $n = 28$. On top of that, TurbSim does not allow the grid height to be larger than twice the hub height. For this reason, the $Z$ direction has to be trimmed while also ensuring that the rotor diameter fits inside the cross-section. This leaves us with $m = 18$ and is the reason for the sizes presented in Section 4-2-1.

It should also be noted that this helical data already has a predefined excitation frequency $f_e$. It is found that over $k = 800$ time steps the helical structure rotates exactly 12 times. To make this structure rotate with a desired frequency, TurbSim has to sample the data with a specific sampling time. The smaller the sampling time, the slower it will rotate. Using the relation:

$$T_s = \frac{N_{\text{rot}}}{f_e k}, \tag{4-5}$$

the sampling time $T_s$ can be chosen via the desired $f_e$. This only represents the sampling time that is given to TurbSim and not the sampling time used for the controller schemes. For the *NREL 5-MW* turbine with a Strouhal number of 0.25 and 0.4, the sampling times correspond to $T_s = 0.42$ and $T_s = 0.2625$ seconds respectively. Whilst this helical wake data set is an improvement in fidelity over the rotating disc data set, using it in OpenFAST still

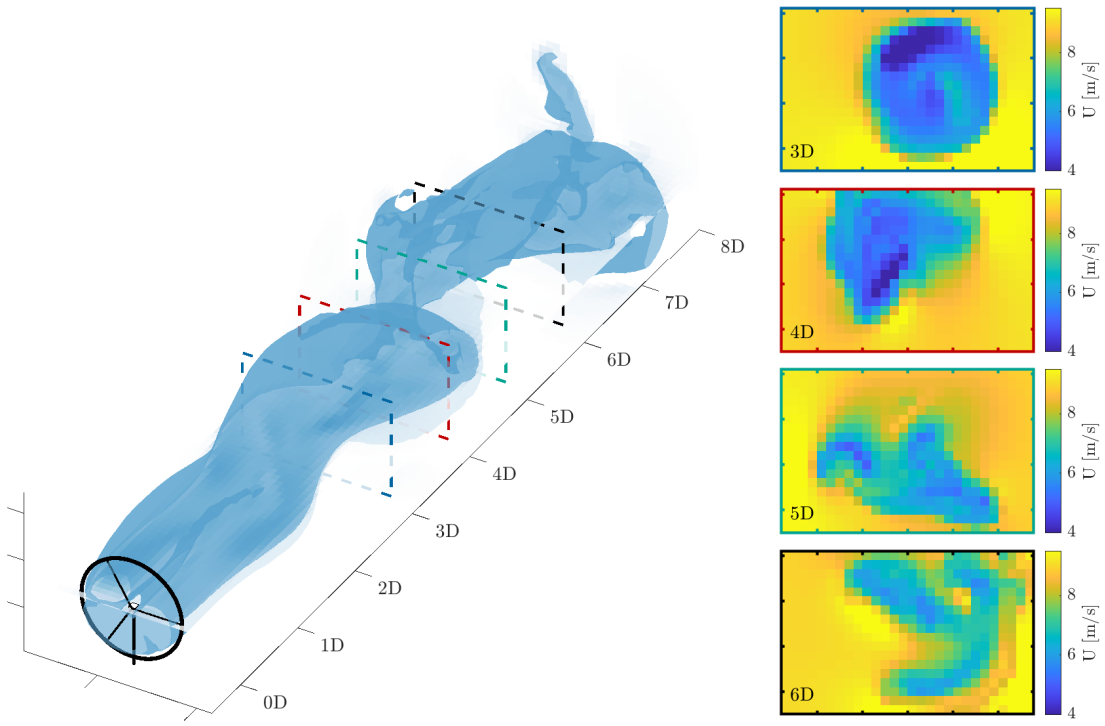



**Figure 4-3:** Wind field volume extracted from SOWFA data and four cross-sections at different turbine distances. **Left:** three-dimensional iso-surface of a wind field produced by a *DTU 10-MW* turbine performing the helix method. The darker blue shading indicates a wind velocity in the $X$-direction of 7 m/s. On the $XY$-plane, the absolute wind velocity is plotted in lighter blue. Further down the wake, it can be seen that the structure rotates counterclockwise. The data is simulated in SOWFA by the authors of [22], from which the figure style is also adapted. An upstream turbine is placed at $0D$ to give an indication of the scale. The dashed boxes represent $X$ locations of the different cross-sections. **Right:** four example cross-sections at different rotor distances. The color of the boundary matches the cross-sections shown on the left. The cross-sections have the same dimensions as the wind fields shown in Figure 4-2. The pixel colors indicate the wind speed in the $X$-direction.

has its limitations. The BEM theory used in OpenFAST assumes symmetric loads in the actuator disc. Hence, large blade deflections caused by the amplification of the blade bending moments could violate this assumption. Additionally, the helical data from SOWFA has a low spatial resolution and was not produced by a *NREL 5-MW* turbine. It thus remains unknown whether the dynamics resulting from the interactions between the turbine and this wind inflow are representative of the helix method. To this end, helix wake synchronization has also been tested in two higher-fidelity models. These models will be further explained in the following section.

## 4-3 High-Fidelity Simulation Setup: QBlade & SOWFA

Both the rotating disc and helical wake data sets serve as good test cases for both controller schemes presented in Chapter 2. However, both OpenFAST and TurbSim are not designed to deal with the case of a downstream turbine experiencing a helical wake. The data set shown in Figure 4-3 also has a low spatial resolution and steady wind conditions, which makes it less representative of a real-world example. The helix wake synchronization is therefore also tested in two other simulation environments which are considered to be higher fidelity models. This is because they are both capable to simulate multiple turbines, their wake, and the interaction between those two. These simulation environments are QBlade and SOWFA. The main difference between these tools is that QBlade uses the free-wake vortex to simulate the wake [59], while SOWFA uses CFD methods to simulate an entire wind field and its interaction with the wind turbines. A two-turbine setup is considered for QBlade and a three-turbine setup is considered for SOWFA. The first part will describe the simulation settings for the QBlade experiments.

### 4-3-1 QBlade Setup

QBlade is designed as a modular implementation of efficient multi-fidelity aerodynamic, structural dynamic, and hydrodynamic solvers [60]. It can also use the free-wake vortex method to simulate the wake of a turbine. In [61], QBlade was also used to implement the helix method for floating offshore wind turbines and is therefore suitable for this problem as well. The simulation consists of a two-turbine setup where the upstream turbine (T1) employs the regular helix method. The downstream turbine (T2) is either running a synchronized helix method or a baseline controller without the helix method. The synchronized case uses the RLS-based estimator, as no linearized model was made in the QBlade environment for this thesis. The helical wake produced by the free-wake vortex method results in a lower Signal-to-Noise Ratio (SNR) in the blade bending moments of the downstream turbine compared to the simulations done in OpenFAST. Because of this, the downstream turbine is placed at $4D$ instead of $5D$, the latter of which has a larger velocity deficit. To save on computation costs, only the wake of T1 is computed using the free vortex method. T2 uses the unsteady BEM method, similar to what has been used in OpenFAST, as we are only interested in the blade bending moments. The wake and vortex settings for T1 are summarized in Table 4-3. Both turbines also incorporate ATEF dynamic stall in their aerodynamic model [62].

In total, two different experiments are performed. The first experiment tests the helix wake synchronization method under steady wind conditions with an ambient wind speed of 9 m/s. Similar to Section 4-2-1, four simulation instances are run where the phase of the helix of T1 is varied by 90° each with a total simulation length of 15 minutes. Both T1 and synchronized T2 perform a 2° CCW helix method with an excitation frequency of $1.79 \cdot 10^{-2}$ Hertz for which the Strouhal number equals $St = 0.25$. The second experiment consists of two simulations of 30 minutes with turbulent wind conditions for one phase of T1. Both turbulent wind fields are generated using the in-built TurbSim extension. They are generated with a normal turbulence model (NTM) with spectral model IECKAI for turbine class I. For each case, the turbulence intensity is set to $TI = 5\%$, which is considered a low-turbulence setting and is also used in [22]. The difference between the cases is the power law exponent for the boundary

layer. The power law is described by:

$$u = u_0 \left( \frac{z}{z_0} \right)^{\alpha}, \tag{4-6}$$

where $u$ is the wind speed in meters per second, $z$ is the height in meters, $u_0$ and $z_0$ are the mean wind speed and reference height respectively, and $\alpha$ is the power law exponent. This power law determines how the wind speed changes with height. In [22], a log law, which is a similar measure, was used with a roughness length of $l_0 = 2 \cdot 10^{-4}$ meters. To match this value, the first case uses a power law exponent of $\alpha = 0.08$, which fits the log law curve. This represents a smooth open sea surface. The QBlade user manual, however, suggests a power law exponent of $\alpha = 0.14$ for an offshore setting. The second case, therefore, uses this setting. In literature, this value has a closer resemblance to open land surfaces, and thus $\alpha = 0.08$ is a better choice for open sea surfaces. This is also backed up in the literature, for example, see [63], [64]. Nonetheless, both cases are simulated for this thesis, as it gives a good perspective on the effect of the boundary layer on helix wake synchronization. More information about the boundary layer can also be found in e.g. [58]. The grid size is $35 \times 51$ points with a height of 340 meters and a width of 500 meters. A mean wind speed of 8 m/s is chosen to keep the wind speed below the rated wind speed within region 2. This also reduces the excitation frequency to $1.59 \cdot 10^{-2}$ Hertz. The reference height is set to $z_0 = 85$ meters, which is slightly below the hub height. For both the steady and turbulent experiments, the RLS-based estimator uses an azimuth offset of $\psi_0 = 18°$. The resulting data of both experiments are analyzed in MATLAB.

### 4-3-2 SOWFA Setup

The final simulation tool used for this thesis is the Simulator fOr Wind Farm Applications (SOWFA) [65]. SOWFA uses CFD methods to simulate wind flow and turbulence. Specifically, it uses Large Eddy Simulations (LES) to simulate the fluid dynamics of the turbulent atmosphere. Turbines can be modeled using an Actuator Line Model (ALM) (see e.g. [1, Chapter 3.6]) which allows for the wake to be simulated. SOWFA is used to simulate a three-turbine setup under steady wind conditions. The goal here is to evaluate the effect of helix wake synchronization in T2 on the turbine farthest downstream, T3. On top of that, the total power production of the three-turbine system is considered as well.

**Table 4-3:** QBlade wake and vortex numerical simulation settings used for T1. Table layout and settings inspired by [61]. Compared to [61], the length of wake zone 3 is chosen to be smaller, as here, we are less interested in the dynamics of the far wake.

| **Wake Variables** | **Setting** | **Vortex Variables** | **Setting** |
|---|---|---|---|
| Wake Relaxation | 1 (No. Relaxation) | Initial Core Radius in | 0.05% Chord |
| Max. Wake Elements | $2 \cdot 10^5$ [-] | Vortex Viscosity | 800 [-] |
| Max. Wake Distance | 100 D | Vortex Strain | Off |
| Wake Reduction Factor | 0.001 [-] | Trailing Vortices | Enabled |
| Near Wake Length | 0.5 Revolutions | Shed Vortices | Enabled |
| Wake Zone 1/2/3 Length | 6/12/2 | Wake Rollup | Enabled |
| Time Step | 0.05 [s] | | |
| Azimuthal Step | 3.15° [deg] | | |

**Table 4-4:** SOWFA three-turbine setup simulation sets. All turbines run a $k\omega_g^2$ torque controller as well. The synchronized helix utilizes the RLS-based estimator.

| | **BL** | **Set 1-6** | **Synchronized** |
|---|---|---|---|
| T1 | Helix, 4° CCW | Helix, 4° CCW | Helix, 4° CCW |
| T2 | - | Helix, 2° CCW, Phase 0°-360° | Sync. Helix, 2° CCW, $\psi_0 = 18°$ |
| T3 | - | - | - |

The wind inflow profile is created in SOWFA via a precursor simulation with a neutral Atmospheric Boundary Layer (ABL). The wind conditions for this precursor are a below-rated wind speed of 9 m/s with laminar flow. This precursor is used to generate wind-shear conditions and large turbulent structures without simulating the wind turbines. Planes in this precursor are saved for each time step and used as inflow boundary conditions. SOWFA combines all this wind data with the ALM to simulate the wind farm. The turbine model chosen for this simulation is the *DTU 10-MW* [66], as for this model the turbine setup and precursor were readily available. Compared to Table 4-1, the *DTU 10-MW* has the same rated wind speed but a larger rotor diameter of 178.3 meter and a larger hub height of 119 meter with a rated tip speed of 90 m/s. The turbines are separated by a distance of $5D$.

SOWFA is a very powerful tool that has a large computational cost. Because of this, one series of simulations is performed in a row to analyze the effect of every helix phase in T2 on T3. The first set consists of a baseline case, where T1 is performing a 4° CCW helix while T2 and T3 only perform a $k\omega_g^2$ torque controller to manage the power generation. This set serves as a comparison case for the other test cases. T1 is performing the same helix method for all simulation sets and T3 is always performs a torque controller only. The next six sets each run a 2° CCW helix method in T2, while the phase of the helix is slowly varied over time. The phase is varied from 0° to 360° over the six sets, starting at 0° to 60° for Set 1. This is to analyze the effect of each different phase on the total power production of the three-turbine setup. It thus includes a synchronized case, a partial and complete helix wake rejection cases. The final set is a 2° CCW synchronized helix case that uses the RLS-based estimator with an azimuth offset of $\psi_0$. The RLS method is used over the KF-based estimator because of the ease of implementation of the RLS method and the unavailability of a linearized model. Each set is simulated for a period of 6000 seconds with a sampling time of $T_s = 0.2$. The controllers are switched on at $T = 1000$ seconds and the first 1000 seconds are removed due to transients. This leaves a total of $T_{\max} = 4000$ seconds of usable time. All controller setups are summarized in Table 4-4.

This concludes the simulation setups for both OpenFAST and the high-fidelity tools QBLade and SOWFA. The results for the high-fidelity models are presented in Section 4-5. The next part of this chapter will analyze the results of all experiments. The next section will start with the low-fidelity results in OpenFAST. The final section of this chapter will give a brief overview of the main results.

## 4-4 Low-Fidelity Results: OpenFAST Simulations

In this section, the results of the OpenFAST simulations are shown and evaluated. The first experiment will test the phase estimation capabilities of both the RLS- and the KF-based

estimators using the rotating disc data set. This experiment also serves as a proof-of-concept for the custom wind profiles made via TurbSim. On top of that, this data set provides a more controlled scenario compared to the helical wake profiles generated via SOWFA, as the rotating disc spectrum mainly consists of a peak at the excitation frequency. The second experiment will explore the influence of turbine distance on helix wake synchronization. Similarly, a third experiment investigates the effect of the helix method pitch actuation. These latter two tests focus on the increase in power generation and contribute to finding the optimal settings for maximizing the power in a waked downstream turbine. The final two experiments study the helix wake synchronization and rejection methods. The helix synchronization is also compared to a non-synchronized helix case. For helix wake rejection, only the KF-based estimator is tested, as Chapter 3 showed that the RLS-based estimator is not well suited for this problem.

### 4-4-1 Phase Estimation Rotating Disc

In Chapter 3, it was shown that both the RLS- and KF-based estimators could estimate an unknown phase in a low-order linear model. The rotating disc data set, presented in Section 4-2-1, is used to test and compare both estimators in OpenFAST for the *NREL 5-MW* reference turbine. This data set does not represent a real scenario but results in relatively sinusoidal tilt and yaw bending moments. This makes it an ideal test case for phase estimation in a high-order wind turbine. The objective here, therefore, is to estimate the phase without synchronization. This is done for the four rotating disc inflow profiles, [+0°, +90°, +180°, +270°], each 90° in phase apart. The results are shown in Figure 4-4. On

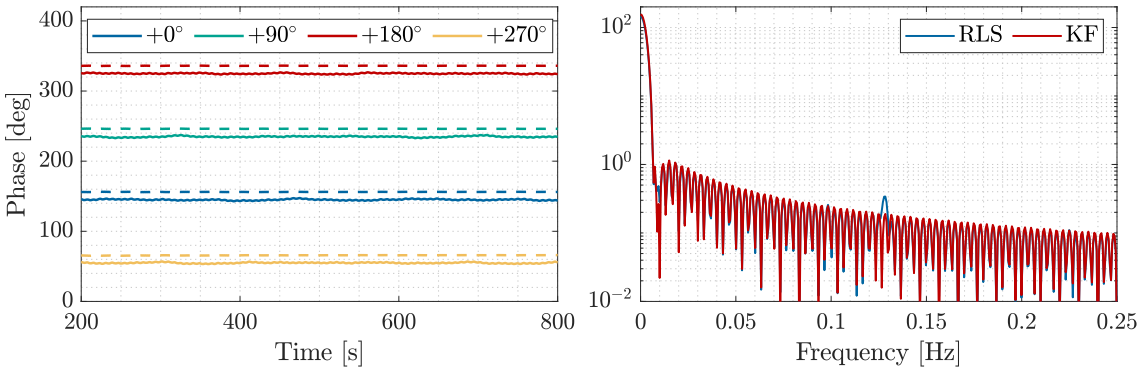



**Figure 4-4:** Time and frequency domain results for the rotating disc wind profiles in the *NREL 5-MW* reference turbine. **Left:** phase estimates from the RLS- (solid) and KF-based (dashes) estimators for 10 minutes of simulation time. The color indicates the same data set, but 90° in phase apart. RLS and KF estimates are separated by the optimal azimuth offset, which is $\psi_0 \approx 11°$ of phase. **Right:** Welch power spectrum estimate of the +0° data set for the RLS- and KF-based estimators. The magnitude is shown in degrees.

the left of Figure 4-4, a simulation time of 10 minutes is shown, of which the first 200 seconds are removed due to startup transients. The solid lines represent the RLS-based estimates and the dashed lines represent the KF-based estimates. Note that these estimates are separated by the selected azimuth angle $\psi_0$, which means that they converged to the same value. Both estimators are able to distinguish the four inflow files from each other by exactly 90°.

Looking at the Welch power spectrum estimates, presented on the right of Figure 4-4, it can be seen that both estimators produce a relatively smooth signal as most frequencies have a contribution of $< 1°$ phase. The RLS estimator does, however, show a small peak of about $0.34°$ phase at $f_r + f_e$ Hertz. This is because the RLS filter is not able to completely remove all the $\psi(t) + \omega_e t$ harmonics. Their effect is already reduced by the low-pass filter shown in Figure 2-8. From Figure 2-7, it can be seen that the effect of $0.34°$ phase error from the steady-state on the amount of amplification can be neglected. Hence, the magnitude of this peak does not affect the overall result when synchronization will be applied. The KF estimate does not suffer from this problem and, therefore, produces a smooth phase estimate. With these results, it can be concluded that custom wind inflow data can be used for the helix wake synchronization in OpenFAST. This is because both estimators managed to differentiate all four different phases with a $90°$ difference.

### 4-4-2 Effect of Turbine Distance

Next, we move to the helical wake data set presented in Section 4-2-1. The first test examines the effect of turbine distance. To do this, simulations are performed for each cross-section of the SOWFA volume at different turbine distances, varying from $3D$ to $6D$ with half rotor distances in between. Four different helical starting points are chosen for each of these cases. Again, within [$+0°$, $+90°$, $+180°$, $+270°$], $90°$ apart. Simulations are run for a baseline case without the helix method (BL) and an RLS-based synchronized case. For the synchronized case, the pitching of the blades starts at $T = 200$ seconds. The total simulation time is 1000 seconds of which the first 240 seconds are removed due to transients. For each distance and control method, the total generated power is measured over this period of time and averaged over the four different helical starting positions. This is given by:

$$\text{Generated power w.r.t. Baseline} := \left( \sum_{j=1}^{4} \frac{P_j^{\text{Sync}}}{P_j^{\text{BL}}} - 1 \right) \cdot 100\%, \tag{4-7}$$

where $P_j^{\text{Sync}}$ and $P_j^{\text{BL}}$ are the total generated power for the synchronized and baseline case respectively for starting phase $j$. The results are shown in Figure 4-5, where this entire experiment is conducted for $St = 0.25$ and $St = 0.4$ with an ambient wind speed of $U_\infty = 9$ m/s. The synchronized case performs a CCW helix with an amplitude of $2.5°$. From the top of Figure 4-5, it can be seen that the net power production of a synchronized helix compared to a baseline case is $> 0\%$ from $4D$ to $6D$. The synchronized method produces on average between $1.0 - 1.1\%$ more power compared to a baseline case for distances $4D$ and $4.5D$ and $2.5°$ amplitude. The difference between the Strouhal numbers for these distances is in the order of $0.05\%$. This difference increases to about $0.1\%$ as the turbine distance goes up. The average generated power of the synchronized case is also shown in Figure 4-5 below. From this figure, it can be seen that the difference in power production between the Strouhal numbers becomes considerably small. The bottom of Figure 4-5 shows the baseline amplitudes of the MBC-transformed blade bending moments at the respective excitation frequencies for both Strouhal numbers and at each distance. It can be seen that the tilt and yaw amplitudes at the excitation frequency are not equal at each distance. The increase in power production with respect to a baseline case at $4D$ correlates with the peak in the yaw moment. Overall, the most interesting region for synchronization using the SOWFA data set and the *NREL*

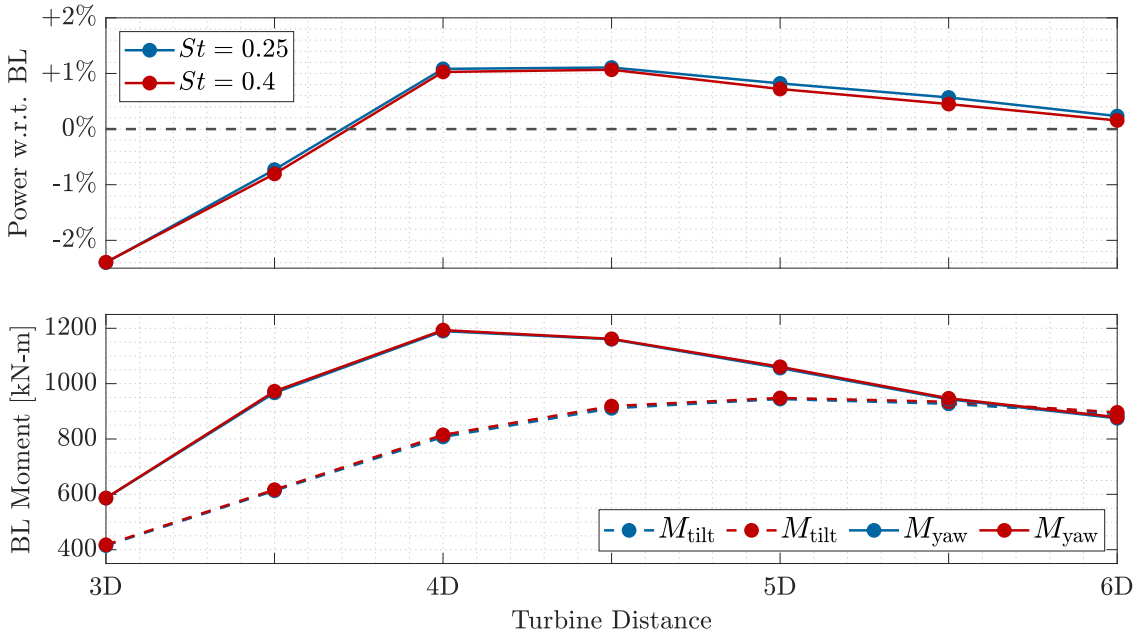



**Figure 4-5:** Power generation of a *NREL 5-MW* reference turbine employing helix wake synchronization with an incoming helical wake at different turbine distances. **Top:** percentage power generation w.r.t. a BL case for different Strouhal numbers ($St$). A net $0\%$ increase is indicated by the dashed black line. **Bottom:** Amplitudes of tilt and yaw blade bending moments of BL turbine at the excitation frequency for each turbine distance. The blue data represents an excitation frequency with $St = 0.25$ and the red data is for $St = 0.4$.

*5-MW* reference turbine in OpenFAST, is between $4D - 5D$ turbine distance. The next section will analyze the effect of the pitch amplitude of the synchronized helix method in this region.

### 4-4-3 Effect of Pitch Amplitude

The next experiment investigates the effect of the helix pitch amplitude on the power generation of helix wake synchronization. A similar experiment is conducted as for the varying turbine distances but, here, the pitch amplitude is varied between [0.5, 4] degrees instead. Besides an RLS-based synchronization case, this experiment also includes a KF-based synchronization. The pitch action starts at 200 seconds. Both methods are compared to a baseline case that does not perform the helix method. For each pitch amplitude, four different wind inflow profiles, within [+0°, +90°, +180°, +270°], are simulated for 1000 seconds. The first 240 seconds are again removed due to transients. The generated power with respect to the baseline case is also computed via Equation 4-7. Finally, the turbine distance is fixed at $4D$ with a Strouhal number of $St = 0.4$ as this is within the range of the largest power increase. Results are shown in Figure 4-6. Here, both the RLS- and the KF-based controllers manage similar power generation up to 3° amplitude. After this, not only the power generation becomes less compared to BL, but also, the power generation of the KF method becomes less than the RLS method. As the KF controller uses a model of the wind turbine which is linearized around 0° pitch amplitude, this model starts to deviate from the actual model as

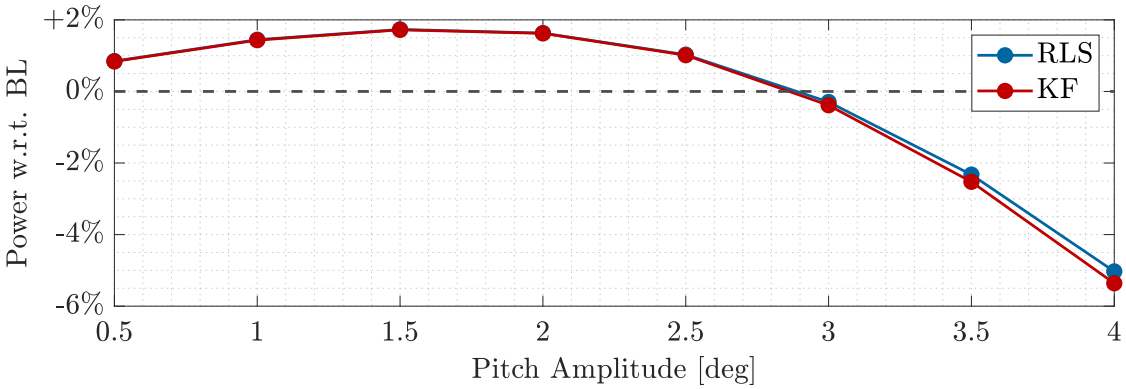



**Figure 4-6:** Average power generation of two helix wake synchronization controllers w.r.t. a BL case for different pitch amplitudes at $4D$. The RLS-based controller is indicated with blue and the KF-based controller with red. A net $0\%$ increase is indicated by the dashed black line.

the pitch increases. Nonetheless, the power production is at maximum around $1.5° - 2.0°$ helix pitch amplitude for both methods. Here, we can find an average increase in power generation with respect to the BL case of $1.72\%$ and $1.63\%$ for $1.5°$ and $2.0°$ respectively. Compared to the RLS method, the KF controller adds another $+0.01\%$ average power generation on top. From Figure 4-6, it can be concluded that for the *NREL 5-MW* reference turbine with the helical inflow profile at $4D$ in OpenFAST, a pitch amplitude between $1.5°$ and $2.0°$ would result in the largest performance increase. However, as we are still interested in wake mixing capabilities to affect downstream turbines, a pitch amplitude of around $2.5°$ can still be considered.

### 4-4-4 Synchronization with the Helical Wake

Let us consider the case where the turbine distance is $4D$ and the helix pitch amplitude is $2°$. To demonstrate the synchronization process, the RLS-based synchronized case is compared to both a baseline controller and a regular helix method. Figure 4-7 shows time-domain results of two helical wind inflows which are $90°$ out of phase. The data is filtered using a zero-phase digital low-pass filter with a pass-band frequency of $f_e$ and a stop-band frequency of $5 \cdot 10^{-2}$ Hertz. Individual pitch control is switched on at $T = 200$ seconds. Within about 30 seconds, the tilt and yaw blade bending moments of the synchronized case (red line) increase in magnitude. The synchronized case is also in phase with the baseline turbine, which represents the bending moments caused by the helical inflow only. The regular helix method, which has no information about the phase of the incoming helical wake, does not align with the baseline case. For the $+90°$ helical inflow, the magnitude of the bending moments in the regular helix case became smaller once the pitching was turned on. This implies that the regular helix method was out of phase with the incoming wake, resulting in destructive interference. Moreover, it shows that a non-synchronized helix method in a waked downstream turbine could result in poor performance over a baseline case. Appendix C-1 shows the time domain results of other power and load related signals.

A benefit of synchronizing with the helical wake is that, due to constructive interference, larger MBC-transformed blade bending moments can be generated with less pitch actuation.

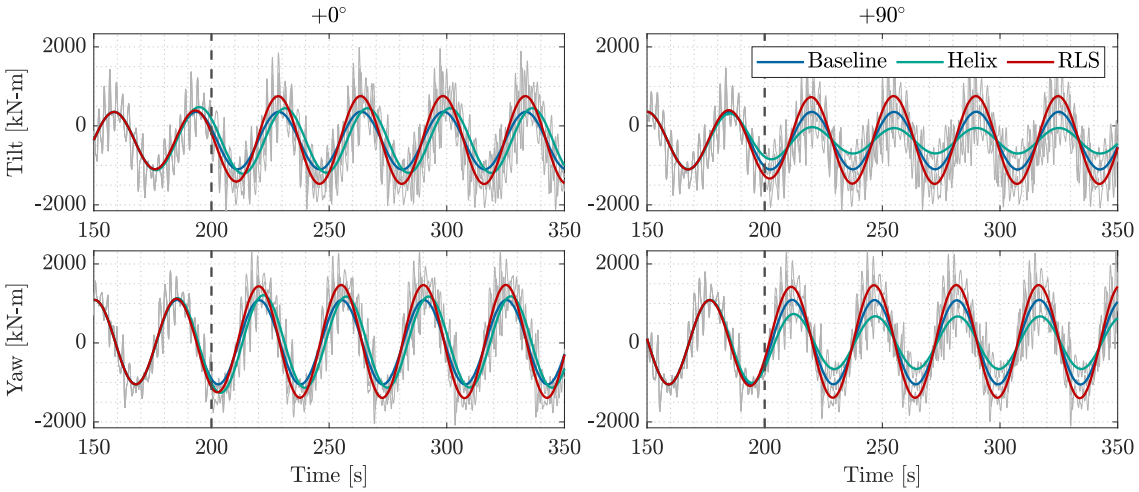



**Figure 4-7:** Comparison of tilt and yaw blade bending moments of three different control strategies for two different helical inflows. The control methods consist of a baseline controller (blue), a regular helix method (green), and an RLS-based synchronized helix method (red). Both helix methods are CCW with an amplitude of 2°. The data is post-processed by using a zero-phase digital low-pass filter. The unfiltered data is shown in gray. The dashed line at $T = 200$ seconds indicates the individual pitch control for the helix method being turned on.

This way, a similar magnitude of blade bending moments can be generated in T2 as in T1, but with less control action. On top of that, this synchronization results in a small power generation increase of 1.63% with respect to the baseline case. Hence, the increase in blade bending moments can be achieved with zero power losses in OpenFAST. Likewise, this implies that the blade bending moments can be decreased as well in the case of out-of-phase synchronization, or destructive interference. This topic will thus be explored in OpenFAST in the following section.

### 4-4-5 Rejection of the Helical Wake

The previous section showed that in OpenFAST for steady wind conditions, helix wake synchronization results in a small increase in generated power over a baseline case. On top of that, it demonstrated that, under these conditions, running a non-synchronized helix in a waked downstream turbine may result in worse power output. Chapter 3 also experimented with helix wake rejection, for which the KF-based controller goes partly or fully out-of-phase with the incoming helix. Instead of increasing the power output of the second turbine, it could potentially decrease fatigue loads as the blade bending moments are reduced. It also has the potential to break up the incoming wake, such that turbines even further downstream could benefit from it. A similar time-domain experiment is conducted as was done in previous sections. The out-of-phase synchronization starts at $T = 200$ seconds and the total simulation length is 1000 seconds. Compared to Figure 4-7, only the +0° wind inflow is used. In total three different out-of-phase synchronizations are implemented in OpenFAST. These are partial and complete rejections, with added phases of $+\pi/2$ and $+\pi$ respectively. The final synchronization is a full rejection, where the KF-based estimator is also used to estimate the pitch amplitude of the fictitious periodic load disturbance at the input. To do this, we can

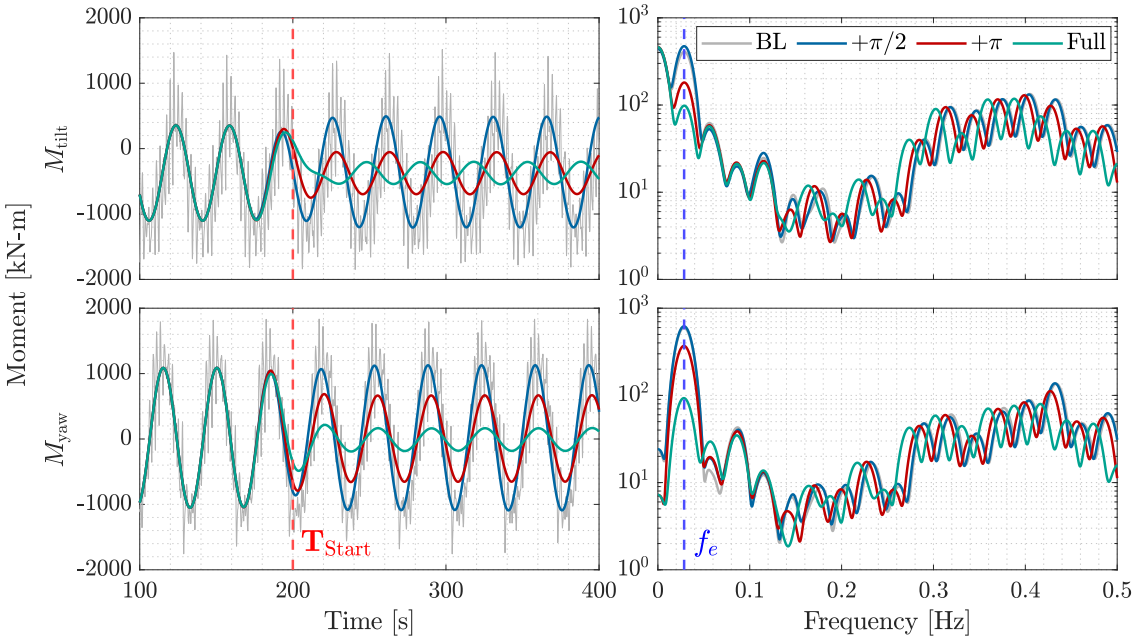



**Figure 4-8:** Time- and frequency-domain results of the tilt and yaw blade bending moments for helix wake rejection. **Left:** Time-domain simulation for the three different rejection cases. The data is post-processed by using a zero-phase digital low-pass filter. The unfiltered data in gray represents the bending moments of a baseline case. The dashed red line indicated the start of the rejection. **Right:** Welch power spectra estimates of the bending moments. The dashed blue line indicates the excitation frequency. The top row consists of the tilting moment $M_{\text{tilt}}$ and the bottom row represents the yaw moment $M_{\text{yaw}}$.

compute the Euclidean norm of Equation 2-29, which results in the amplitude estimate. This pitch angle is then used as control input for the helix method together with a 180° shifted phase estimate. In this scenario, the KF minimizes the magnitude of the tilt and yaw blade bending moments at the excitation frequency. The other two methods have a fixed pitch amplitude of 2° since this was also done for the helix wake synchronization. The results are shown in Figure 4-8.

From the Welch power spectra estimates on the right of Figure 4-8, it can be seen that the partial rejection method has a similar magnitude to a baseline case. However, from the time-domain results, it can be seen that there is a slight phase shift in the output. Comparing this to Equation 2-26, we find that because of interference the resulting phase of the output will be shifted by a combination of the magnitudes and phases of the input and helical wake. Likewise, for the complete rejection method, the control input is 180° out-of-phase but still appears to be in-phase. This is due to the amplitude of the control input not being large enough to reject the wake fully. From the power spectra, it can be seen that this method does succeed in lowering the magnitude by a significant amount compared to a baseline case. The full helix wake rejection method estimates a disturbance pitch amplitude of 4.4°. However, it is not able to fully reject the magnitude of the peak at the excitation frequency. It has the best rejection of all three methods, but this is mainly due to the larger pitch action. The KF expects the amplitudes of both tilt and yaw blade bending moments to be equal and for those moments to be centered around zero. However, from the upper left corner of Figure 4-8 it is

evident that this is not the case for the tilting moment. This could be the reason why the method cannot fully reject the wake.

Overall, this experiment demonstrates some of the possibilities for the partial or complete rejection of a helical wake using synchronization methods. In terms of power generation, these methods perform worse compared to in-phase synchronization. The three methods have a mean power output of $-1.04\%$, $-4.96\%$, and $-13.1\%$ compared to the baseline case for the $+\pi/2$, $+\pi$, and full rejection methods, respectively. These losses are proportional to a reduction in their rotor speed. Nonetheless, this method still has the potential for load mitigation or wake mixing in general.

### 4-4-6 Concluding Remarks Low-Fidelity Results

Section 4-4 shows the results for the simulations performed in OpenFAST for the *NREL 5-MW* reference turbine. It was demonstrated that the customized wind inflow data from TurbSim can be used to study the interactions of a helical wake with a downstream turbine on a low level. Although in [24], it was shown that the blade load signals in OpenFAST are similar enough to the loads in SOWFA, the validity of these results remains questionable. For example, the BEM theory used in OpenFAST assumes symmetric rotor loads contained in the actuator disc. The combination of helical wind inflow and pitch actuation might lead to large blade deflections which may cause the near wake of the turbine to diverge from its uniform shape [67]. Higher-fidelity aerodynamic models are required to account for the increased complexity of the interaction between the wake and turbine. Additionally, the helical wind profile has a low spatial resolution and was produced by a *DTU 10-MW* reference turbine model in SOWFA under steady wind conditions. Although pitch amplitude, turbine spacing, and excitation frequency parameters have been varied throughout these experiments, the effect of a considerable amount of settings remains unclear. The above-presented results do point toward the idea that a downstream turbine can benefit from an incoming helical wake. Whether that be via in-phase or out-of-phase synchronization. For these reasons, helix wake synchronization is also tested out in the higher-fidelity simulation tools QBlade and SOWFA. A brief summary of the low-fidelity results and a comparison with the high-fidelity results will be given at the end of this chapter. The next section will discuss the high-fidelity results.

## 4-5 High-Fidelity Results: QBlade & SOWFA Simulations

In the final part of this chapter, the results of the high-fidelity simulation tools, QBlade and SOWFA, are shown and evaluated. For this thesis, these tools are considered to be high-fidelity compared to OpenFAST as for both, multiple turbines and their wake are simulated. There are two main differences between these simulation setups. QBlade computed the wake via the free-wake vortex method while SOWFA uses CFD to compute the entire wind field and the wake dynamics. The second difference is that in QBlade we consider a two-turbine setup and in SOWFA a three-turbine setup. This is because in QBlade, we are interested in helix wake synchronization capabilities of the waked downstream turbine in steady and turbulent conditions. While in SOWFA we consider the effect of synchronization on a total power production level. The next part will start with the results of the QBlade simulations.

### 4-5-1 QBlade Results

This section follows the simulation setup as presented in Section 4-3-1. Two experiments are performed to test the helix wake synchronization method in a waked downstream turbine (T2) in a two-turbine setup. The first test is similar to the experiment shown in Figure 4-7 and examines the increase in power generation in T2 compared to a baseline case. The second experiments also examine power generation, but a turbulent wind field is superimposed. Here, two cases are compared, each with a different boundary layer. In both experiments, the helix synchronization is turned on at $T = 300$ seconds, as about 200 seconds is required for the free vortex wake to reach T2 and stabilize. Below the results for the steady wind conditions are shown.

#### Steady Wind Inflow

The results of the steady wind inflow simulations are shown in Figure 4-9. On the left of this figure, it can be seen that the RLS-based estimator is able to differentiate the four different phases by roughly 90°. After $T = 300$ seconds, the baseline phase estimate has an average standard deviation of 7.75° while the synchronized helix has an average standard deviation of 5.1° from their mean. Hence, the baseline estimate is less smooth compared to the synchronized case. This is also evident from the Welch power spectra estimates in Figure 4-9, as the baseline case has an average SNR of $-2.04$ dB. This is similar to the top left case in Figure 3-4, as with synchronization, and thus with pitch action, the average SNR is 3.91. This is close to the 1.93 dB shown in Figure 3-4 in terms of magnitude. It

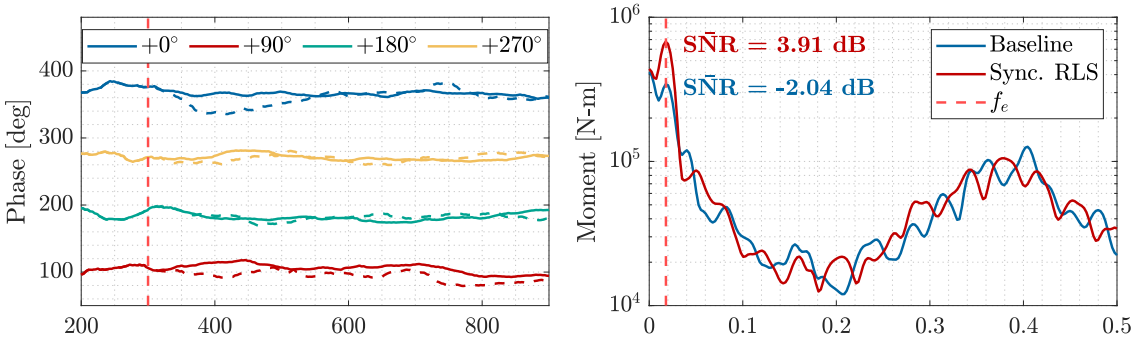



**Figure 4-9:** Time- and frequency-domain results for helix wake synchronization in QBlade for steady wind conditions. **Left:** phase estimates of the RLS filter in T2 for four different initial helix phases of T1. The solid lines represent the estimates under synchronization, while the dashed lines represent the baseline cases. The vertical red dashed line indicated the start of the synchronization. **Right:** Welch power spectrum estimate for tilt blade bending moment in T2. Both the synchronized and baseline case are shown. The red dashed line indicates the excitation frequency $f_e$.

is challenging to validate whether these phase estimates are actually correct, as the baseline case experiences more noise. The generated power is therefore used as a benchmark for this experiment. The average power is therefore computed according to Equation 4-7, for which the first 450 seconds of data are removed due to transients. On average the synchronized case generated +1.76% more power compared to the baseline case. This result is in line with

the results presented in Section 4-4-4 for a downstream turbine at $4D$ with a pitch amplitude of 2°. However, this does not guarantee that the mean power found is the maximum power achievable.

### Turbulent Wind Inflow

The results for both turbulent cases are shown in Figure 4-10 below. The left of this figure displays the Welch power spectra estimates for the tilt and yaw blade bending moments of the BL and synchronized (Sync) downstream turbines T2. Here, 1 denotes the case for which $\alpha = 0.08$ and 2 denotes the case for which $\alpha = 0.14$ from the power law given in Equation 4-6. The top right of Figure 4-10 shows the difference between both Power Law (PL) boundary layers and also compares them to the log law (LL) used in the original helix method paper [22]. Finally, the bottom right of this figure shows the difference in power between the synchronized case and the BL case. This is defined as $\Delta P_i = P_i^{\text{Sync}} - P_i^{\text{BL}}$, where the subscript $i$ denotes the case number. The mean of the difference is also shown and is represented by $\bar{P}_i$, which is the same computation as Equation 4-7. In Appendix C-2, other time domain signals for the BL and synchronized case with $\alpha = 0.08$ are shown.

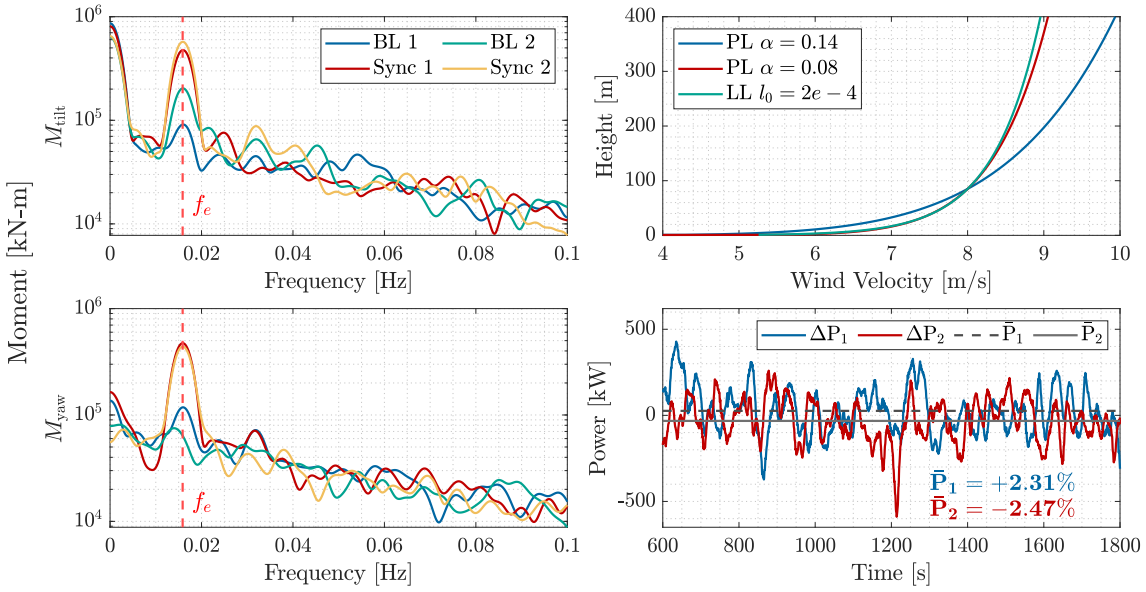



**Figure 4-10:** Results for the QBLADE simulations with turbulent wind conditions. Both cases have a turbulence intensity of $TI = 5\%$, but each with a different boundary layer exponent $\alpha$. **Left:** Welch power spectra estimates of tilt and yaw blade bending moments in T2. For both cases, the BL and synchronized (Sync) turbines are displayed. The red dashed line indicated the excitation frequency $f_e$. **Top right:** comparison of the different boundary layers. It can be seen that the PL with exponent $\alpha = 0.08$ of case 1 roughly fits the log law (LL) with roughness length $l_0 = 2 \cdot 10^{-4}$. **Bottom right:** difference in power generation between synchronized and baseline downstream turbines $\Delta$P. The mean power generation over a period of 1200 seconds for both cases is denoted by $\bar{\text{P}}$.

From Figure 4-10 it can be seen that the second BL case, with $\alpha = 0.14$, has uneven tilt and yaw blade bending moments. The tilt moments at the excitation frequency is about $2 \cdot 10^5$

kN-m, while the yaw moment is below $10^5$ kN-m. For the first BL case, with $\alpha = 0.08$, both the tilt and yaw moments are about $10^5$ kN-m at the excitation frequency. This indicates that, for case 2, the shape of the helix at the rotor disc of T2 is more skewed compared to case 1. This is also expected from Figure 4-10, as the air on top of the rotor disc moves faster compared to the bottom of the rotor disc due to the power law for $\alpha = 0.14$. We also find that the mean power generation of the second case compared to BL is $\bar{P}_2 = -2.47\%$, while the other case has a power increase of $\bar{P}_1 = +2.31\%$. This is over a period of 20 minutes, as the first 10 minutes are removed due to transients. However, in the bottom right of Figure 4-10, it can also be seen that the difference in power $\Delta P$ fluctuates considerably with time due to the turbulent wind conditions. In the period from $T = [1200, 1800]$ seconds the mean power for both cases drops to $\bar{P}_1 = +0.74\%$ and $\bar{P}_2 = -3.48\%$ for case 1 and 2 respectively. Because of this, it is more reasonable to conclude that under low turbulence intensity, helix wake synchronization in T2 may be possible with little to zero losses in the average power generation of T2. Hence, the next section will investigate the effect of helix wake synchronization on the wake mixing further downstream and at a third turbine.

### 4-5-2 SOWFA Results

This section discusses the simulation results of the high-fidelity model SOWFA, which are the final results of this thesis report. All the sets are shown as a single time series over a period of $3.2 \cdot 10^4$ seconds. The first result covers the estimated phases of T2 for each simulation while the second result shows the power generation of T2 and T3 over time. Only the synchronized helix case utilizes the RLS-based estimator online. However, this data is not available, hence all phases are computed in post. This resulted in some transients which were not present during the simulation itself. These phase estimates of T2 are shown in Figure 4-11. From this

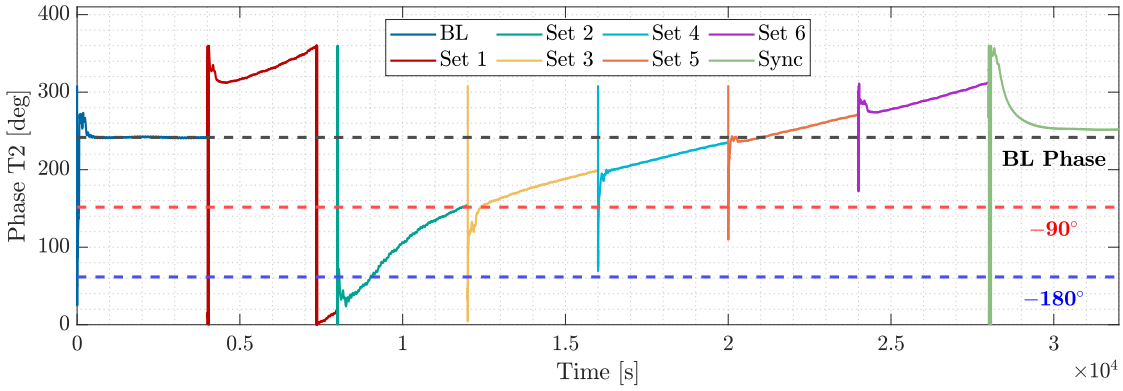



**Figure 4-11:** RLS estimates of the helix phase in T2 for all eight SOWFA sets. The phase is estimated in post, as the data was not available during post-processing. The mean phase of the BL case is indicated with the black dashed line. Likewise, $-90°$ and $-180°$ differences with this mean are shown by the red and blue dashed lines respectively.

figure, it can be seen that the mean estimated phase of the BL case is about 242°. This is indicated by the black dashed line. Likewise, a $-90°$ and $-180°$ difference with this mean are indicated as well. What is important to note here, is that the estimated phase is computed using the tilt and yaw blade bending moments of T2. We know that this estimates the phase

on the right side of Equation 2-7. Hence, the phase estimate also includes the effect of the incoming helix. Because of this, some of the phase estimates do not match the phase they were given. For example, Set 1 gradually increases from 0° to 60°, while in Figure 4-11 it roughly goes from 320° (−40°) to 20°. The incoming helical wake, therefore, perturbs the helix phase of T2. For constructive interference, we find that the estimated phase matches the control input. This is evident from Set 5, which starts at 240° and thus matches with Figure 4-11. Finally, the phase of the synchronized case converges with the phase of the BL case. However, the estimated phase is off by about 10°, which is likely the result of an azimuth offset miss-match.

The generated power over time is displayed in Figure 4-12 for both T2 and T3. The mean power of the BL is indicated with the dashed black line. From the bottom of this figure, we find that there is a clear moment where T3 is producing more power compared to the BL case. This happens between Sets 2, 3, and 4, with the maximum power output happening during Set 3. The phase of the control input of T2 for this set starts at 120° and goes to 180°. In Figure 4-11, this phase goes from about 140° to 200°, which is a shift of 20°. We also have to take into account the fact that T2 has a delayed effect on T3, due to the $5D$ distance between them. For a velocity deficit of approximately 50%, the wake would travel from T2 to T3 in about 200 seconds. With these observations, it can be found that the peak in power in T3 is approximately caused by the phase at $1.4 \cdot 10^4$ seconds in T2, which corresponds to about 178°. Subtracting the phase shift gives a control input in T2 of 158° and is thus 84° out-of-phase with the incoming helical wake. This approximation is similar to a partial wake rejection as was also done in Figure 3-5 and Figure 4-8. However, in this case, the control phase is specifically lagging about 90° compared to the incoming helical wake. In Set 3, T3

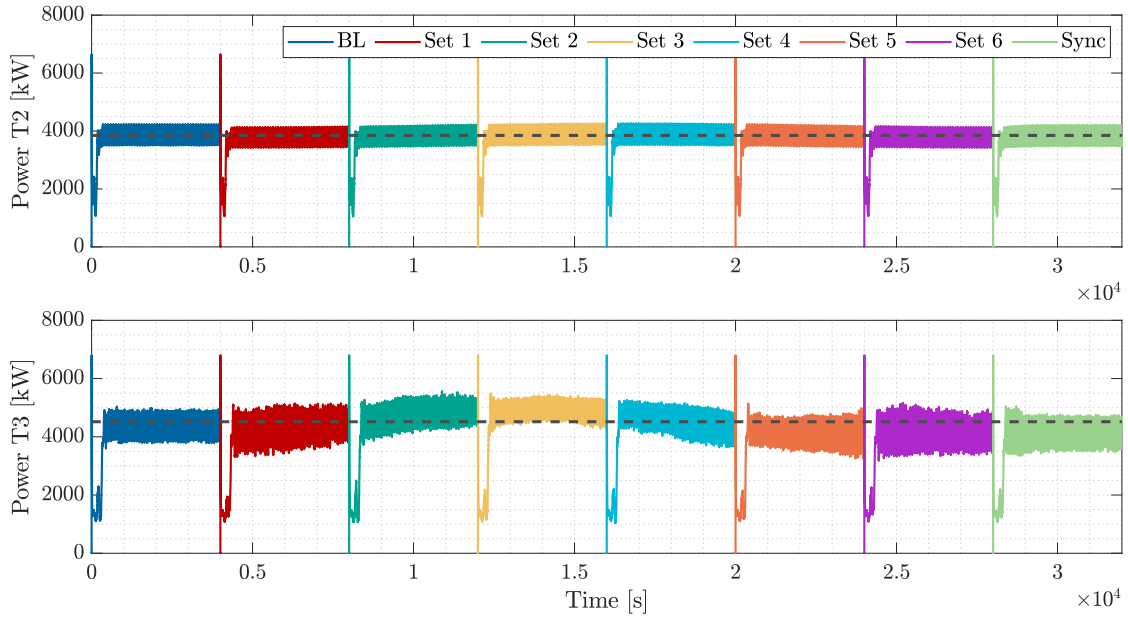



**Figure 4-12:** Generated power of the SOWFA simulations for T2 and T3. **Top:** power generation of T2 over time. **Bottom:** power generation of T3. The black dashed lines represent the mean power of both the T2 and T3 BL cases.

produces on average +9.79% more power than the BL T3. This is equal to an increase of 0.44

MW. On top of that, T2 produces on average +0.14% more power than the BL T2 for Set 3. This could mean that the partial rejection of the helix in T2 leads to better conditions for the mixing of the wake such that T3 benefits from it. The full three-turbine setting produces on average +5.35% more power compared to the BL case. The synchronized case does not show any increase in power production. Here, the three-turbine setup produces on average −4.35% less power compared to BL. An overview of the power production for all sets is given in Table 4-6.

Finally, we can also investigate the MBC-transformed blade bending moments. Figure 4-13 shows the tilt blade bending moments for all sets of T2. The data is filtered using a zero-phase digital low-pass filter with a pass-band frequency equal to the excitation frequency and stop-band frequency of 0.05 Hertz. From the right of Figure 4-13, it can be seen that this filter results in a smooth sinusoidal signal. The points where the phase estimates in Figure 4-11 crossed the dashed horizontal lines are indicated by the dashed vertical line of the same color. We find that at the −180° out-of-phase point, the tilt bending moments are at their lowest amplitude of all sets. Likewise, the tilt moments are maximal at the phase of the BL case in Set 5 and for the synchronized case, which also has the phase of the BL case. Figure 4-13 therefore shows that smaller or larger blade bending moments can be achieved in a waked downstream by altering the phase with respect to the incoming helix, while the pitch amplitude stays constant. These results from SOWFA show that there is

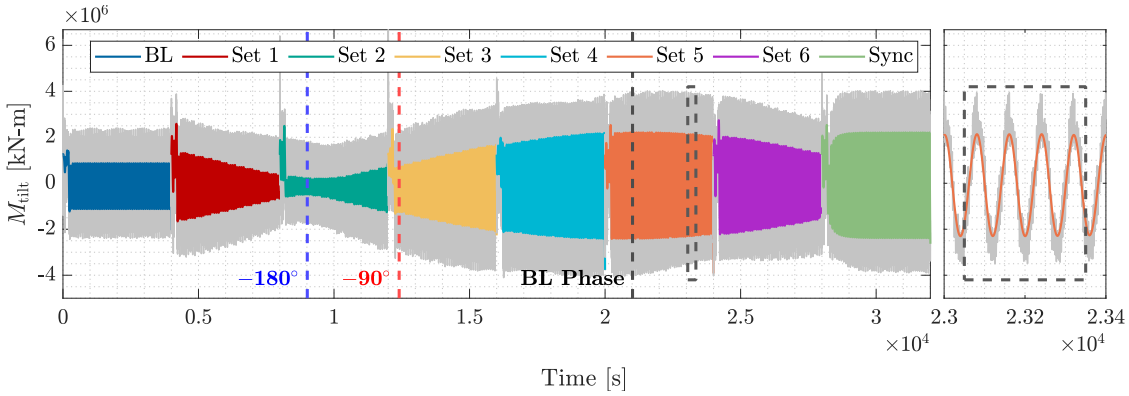



**Figure 4-13:** Tilt blade bending moments of T2 for SOWFA data sets. The moments are filtered using a zero-phase digital low-pass filter. The original data is shown in gray. A zoomed-in region is displayed on the right to better show the filtered data. The dark gray dashed rectangle indicates this. The vertical dashed lines are the times where the estimated phase crossed the horizontal lines in Figure 4-11.

a significant potential for dynamic wake mixing in a multi-turbine setting by exploiting the phase of the helical wake in a downstream turbine. A mean power increase in Set 3 for T3 of +9.79% without power losses in T2 is quite remarkable, even for steady wind conditions. This increase is in addition to the increase in power due to the regular helix method in T1.

## 4-6 Summary Results Wind Turbine Simulations

This chapter dealt with the simulation setups for all the conducted experiments with helix wake synchronization in a high-order wind turbine. The simulation environments gradually

**Table 4-5:** SOWFA mean power generation results for T2 and T3. The percentages are given with respect to the baseline case of the same turbine row. Both the power and percentages are rounded upward.

| | **Phase** | **Power [MW]** | | | | **Phase** | **Power [MW]** | | |
|---|---|---|---|---|---|---|---|---|---|
| | **[deg]** | **T2** | **T3** | **Total** | | **[deg]** | **T2** | **T3** | **Total** |
| **BL** | 242 | 3.85 | 4.52 | 8.36 | **Set 4** | 120-240 | 3.86 | 4.63 | 8.48 |
| | | - | - | - | | | +0.3% | +2.4% | +1.4% |
| **Set 1** | 0-60 | 3.77 | 4.39 | 8.16 | **Set 5** | 240-300 | 3.82 | 4.18 | 8.00 |
| | | −2.1% | −2.8% | −2.5% | | | −0.8% | −7.4% | −4.4% |
| **Set 2** | 60-120 | 3.81 | 4.84 | 8.64 | **Set 6** | 300-360 | 3.77 | 4.24 | 8.01 |
| | | −1.0% | +7.1% | +3.3% | | | −2.0% | −6.1% | −4.2% |
| **Set 3** | 120-180 | 3.86 | 4.96 | 8.81 | **Sync.** | 252 | 3.82 | 4.21 | 8.03 |
| | | +0.1% | +9.8% | +5.4% | | | −0.8% | −6.9% | −4.1% |

increased in fidelity and the number of turbines simulated. This section will give a brief summary and comparison of all the results and main findings. For OpenFAST the following main results were found:

### OpenFAST

- In-phase helix wake synchronization for increased power generation in a downstream turbine is dependent on turbine spacing and pitch amplitude. For the *NREL 5-MW* reference turbine, the optimal turbine distance is between $4D$ and $5D$, and the optimal pitch amplitude is between 1.5° and 2°.
- Increased MBC-transformed bending moments can be achieved with less pitch actuation when the downstream helix method is in-phase with the incoming helical wake. Likewise, out-of-phase synchronization can be used to reduce the blade bending moments.

To test for more complex wind conditions, the synchronization method was also implemented in QBlade. Helix wake synchronization was applied to waked downstream turbine under steady and turbulent wind conditions. The following results were found in QBlade:

### QBlade

- In a two-turbine setting, the downstream turbine was able to synchronize with the incoming helical wake for steady wind conditions. The synchronization was done with a low SNR in the frequency of the incoming helical wake.
- At low turbulence intensity, the downstream turbine was also able to synchronize with the incoming helical wake. This could be achieved with no power losses for a smooth boundary layer and with a small power loss for a rougher boundary layer.

A comparison between the results of OpenFAST and QBlade are given in Table 4-6. The in-phase synchronization method performed similarly for both simulation tools under steady wind conditions. For a low turbulence intensity and smooth surface roughness for the boundary layer, the downstream turbine managed a similar outcome. It is likely, however, that a longer simulation time might result in a lower mean power generation. Both OpenFAST and QBlade used BEM theory for the downstream turbine. Two limitations of this method are that it is not suited for large blade deflections in the actuator disc and that it assumes a steady wind inflow [67]. CFD methods are capable of capturing the increased complexity of flexible rotors and wake dynamics. Therefore, the synchronization and effect of the phase of the helix have also been studied in SOWFA. A short summary of these results is shown below.

**Table 4-6:** Comparison between OpenFAST and QBlade results.

| **Software** | **OpenFAST** | **QBlade** | **QBlade** |
|---|---|---|---|
| Wind Conditions | Steady, 9 m/s | Steady, 9 m/s | Turbulent, 8 m/s |
| Turbulence Setup | - | - | TI = 5%, $\alpha = 0.08$ |
| Distance | 4D | 4D | 4D |
| Total Simulation Time | 30 min | 30 min | 20 min |
| Helical phase T1 | $\{0°, 90°, 180°, 270°\}$ | $\{0°, 90°, 180°, 270°\}$ | $0°$ |
| Strouhal | 0.4 | 0.25 | 0.25 |
| Excitation Frequency | $2.86 \cdot 10^{-2}$ Hz | $1.79 \cdot 10^{-2}$ Hz | $1.59 \cdot 10^{-2}$ Hz |
| Helix Amplitude T1, T2 | $4°, 2°$ | $2°, 2°$ | $4°, 2°$ |
| Mean Power BL | 1.044 MW | 1.048 MW | 1.131 MW |
| Mean Power Sync. | 1.061 MW | 1.067 MW | 1.157 MW |
| Mean Power w.r.t BL | +1.63% | +1.76% | +2.31% |

### SOWFA

- In-phase helix wake synchronization in T2 did not result in an increase in power for the three-turbine system. The downstream turbine T2 was able to synchronize with the incoming helical wake with minimal power losses. However, on average T3 had a reduced power output of −6.88% with respect to the baseline case.
- It was found that for a three-turbine setting, T3 produced on average +9.79% more power compared to a baseline case when T2 was $-90°$ out-of-phase with the incoming helical wake. This did not cause any power losses in T2, which resulted in a total power increase of 5.35% for the three-turbine system.

This increase in power generation for a three-turbine system is also on top of the expected power increase from the regular helix method. This makes helix wake synchronization in a multi-turbine setting an interesting wake mixing strategy with substantial potential. Further conclusions and recommendations for this method will be given in the final chapter of this thesis report. The next chapter will derive stability and robustness conditions for both controller methods that were implemented for this work.

# Chapter 5

# Stability Analysis

The results presented in Figure 3-4 and Figure 3-5 show phase estimates which are perturbed by noise or an incorrect azimuth offset. Likewise, in Chapter 4 it was shown that the presence of turbulence resulted in a low Signal-to-Noise Ratio (SNR) at the excitation frequency. Clearly, both controller schemes have their limitations which could even cause the phase estimate to become unstable in the case of Figure 3-5. For this reason, the stability of both controllers is assessed in this chapter. Unfortunately, assessing the stability of both closed-loop systems, presented in Figure 2-8 and Figure 2-9, is not trivial. This is because they contain the highly nonlinear wind turbine, an adaptive estimator, and nonlinear feedback through phase-shifting the input for the helix. Moreover, the wind turbine system and the adaptive estimators are both time-varying. The focus of the stability analysis will therefore be on the adaptive estimators themselves, as bounded and smooth estimation results in a stable helix method. First, the boundedness and asymptotic stability of both the Kalman Filter (KF)- and Recursive Least Squares (RLS)-based estimators are shown. Then the stability of the phase convergence for the RLS estimator is assessed by analyzing the azimuth offset error. This chapter will end with a note on the robustness based on this analysis.

## 5-1 Boundedness Properties and Asymptotic Stability

In this section, it will be shown that under specific conditions both the KF and the RLS estimators share similar boundedness and stability properties. Boundedness here in this sense is defined as the state covariance matrix $P_k$ and elements of the Kalman (controller) gain $K_k$ being bounded. Under these conditions and the boundedness of the estimator itself, asymptotic stability can be proven regardless of the stability of the output error (OE) system itself. The OE system refers to the system for which the estimation is done via an output-error method, such as the KF, (see e.g. [47]). Hence, for bounded and asymptotically stable estimator dynamics, we have bounded-input, bounded-output (BIBO) stability of our adaptive filter. This means that as long as the input sequence to the estimator is bounded, the estimate itself will be bounded as well. This concept is more natural for adaptive controllers as the

estimate depends on the input sequence and the dynamics of the estimator [68, Chapter 3.4]. The boundedness and stability of continuous-time OE systems have been studied in [69]. However, for this problem, we consider a discrete-time case. We, therefore, follow the proof presented in [70] and show that specific conditions hold for the KF estimator. After this, it is shown that the RLS estimator can be treated as a special case of the KF and thus shares the same boundedness and stability properties.

Let us first consider the required assumptions. Given is a discrete-time OE system in the form of:

$$\begin{aligned} x_{k+1} &= A_k x_k + B_k u_k \\ y_k &= C_k x_k + R_k^{1/2} v_k, \end{aligned} \tag{5-1}$$

where $x_k \in \mathbb{R}^n$ is the state vector, $u_k \in \mathbb{R}^l$ the input, $y_k \in \mathbb{R}^m$ the output, and $v_k \in \mathbb{R}^m$ a Gaussian white noise signal with identity covariance matrix. The matrices $\{A_k, B_k, C_k, R_k^{1/2}\}$ are real and have the appropriate size. $R_k^{1/2}$ denotes the square root of the measurement noise covariance which is symmetric and positive definite. The discrete time step is denoted by $k = 0, 1, 2, ...$, and for all $k > 0$, the square matrix $A_k$ is assumed to be invertible. This is required for the system dynamics to be invertible such that the equality $x_k = \Phi(k, l)x_l$ holds with the state transition matrix $\Phi(k, l) = A_k A_{k-1} \dots A_{l+1}$, for all integers $k, l \geq 0$, including $k < l$ such that $\Phi^{-1}(k, l) = \Phi(l, k)$. The initial state $x(0) \in \mathbb{R}^n$ is drawn from a Gaussian distribution, where $x(0) \sim \mathcal{N}(x_0, P_0)$ with some mean value $x_0 \in \mathbb{R}^n$ and symmetric positive definite covariance matrix $P_0 \in \mathbb{R}^{n \times n}$. The final assumption is that the matrix pair $\{A_k, C_k\}$, with $A_k \in \mathbb{R}^{n \times n}$ and $C_k \in \mathbb{R}^{m \times n}$, has to be uniformly completely observable. Such a matrix pair has uniform complete observability if there exist positive constants $\rho_1, \rho_2$ and a positive integer $h$ such that, for all $k \geq h$, the following inequalities hold:

$$\rho_1 I_n \leq \sum_{s=k-h}^{k} \Phi^\top(s, k) C_s^\top R_s^{-1} C_s \Phi(s, k) \leq \rho_2 I_n, \tag{5-2}$$

where $R(s) \in \mathbb{R}^{m \times m}$ represents the covariance of the output noise in this case. Equation 5-2 represents a lower- and upper-bounded discrete-time observability Gramian [70]. Complete observability refers to each state being observable in the interval $[k - h, k]$ and uniform observability refers to Equation 5-2 to hold for all $k \leq h$ [71]. Uniform completeness in this sense ensures that the state estimation process is well-conditioned [72]. The next part will address these assumptions for the KF-based estimator.

### 5-1-1 Boundedness and Stability of KF Dynamics

The above-presented assumptions are checked for the KF-based estimator derived in Section 2-5. We, therefore, consider the augmented discrete-time state-space from Equation 2-32 and the adaptive filter update scheme from Equation 2-35. By using the Schur complement, it can be shown that $\mathbf{A}$ is invertible if $A_\mathrm{d}$ and $A_\mathrm{d}^\mathrm{p}$ are both invertible [73]. We find that both $A_\mathrm{d}$ and $A_\mathrm{d}^\mathrm{p}$ are square and full rank, hence invertible as well. The initial state $x_0 = \mathbf{0} \in \mathbb{R}^n$ and the initial covariance matrix is set to $P_0 = I_n \succ 0$, which checks the assumptions for the initial conditions.

It should be noted that Equation 5-1 is expressed in a different form than presented in Equation 2-32. The KF-based estimator also contains the system feedthrough matrix $\mathbf{D}$ and process noise $w_k$. In this sense, the process noise could be expressed as a Gaussian white noise signal with identity covariance matrix and scaled by $Q_k^{1/2}$. For the case where the matrix pair $\{A_k, Q_k^{1/2}\}$ is uniformly completely controllable and $\{A_k, C_k\}$ is uniformly completely observable, the Kalman filter is stable [74]. However, as zero load disturbance is assumed on the augmented states, the uniform complete observability condition can not be guaranteed. The absence of the feedthrough matrix $\mathbf{D}$ does not affect the boundedness and stability of the KF-based estimator. This is because the innovation sequence is independent of $\mathbf{D}$ and the input as $e_k = C_k(x_k - \hat{x}_k)$. This error only influences the state estimate $\hat{x}_k$. Hence for a bounded and real feedforward matrix and bounded control input, the stability is not affected. The covariance matrix of the measurement noise is given by $R = \sigma_v I_m$ for all time steps $k$ with $\sigma_v 10^{-5}$. Therefore it is symmetric, positive definite, and has a strict positive lower bound.

The remaining condition to be checked is the uniform complete observability of $\{A_k, C_k\}$. Equation 5-1 considers a linear time-varying system. As the KF-based estimator uses a linearized and averaged model of our system, this final assumption can be simplified. Instead of finding the bounds $\rho_1, \rho_2$ and positive integer $h$ such that, for all $k \geq h$, Equation 5-2 holds, we can check for linear time-invariant observability. We find that this observability matrix for the discrete-time augmented matrix pair $\{\mathbf{A}, \mathbf{C}\}$ is full rank and can therefore conclude that the augmented state-space in Equation 2-32 is observable. This also checks the condition presented in Equation 5-2. With this, all assumptions are met for the KF-based estimator. Following the proof presented in [70] and with these sufficient conditions it is found that the KF-based estimator has a positive definite and bounded state covariance matrix $P_k$ and bounded Kalman gain matrix $K_k$. These results and conditions are also sufficient to guarantee the asymptotic stability of the Kalman filter dynamics.

### 5-1-2 Boundedness and Stability of RLS Dynamics

The previous section followed the proof presented in [70] and showed that the KF-based estimator has bounded and stable dynamics. Interestingly, this method can also be applied to the RLS-based estimator. As was mentioned in Section 2-5, the update schemes in Equation 2-21 and Equation 2-35 have a very similar structure. And by viewing the dynamics of the RLS algorithm as a special case of a Kalman filter with an OE model as shown in Equation 5-1, the boundedness and stability of the RLS-based estimator can be proven. The underlying OE dynamics for the RLS algorithm can be written as:

$$\begin{aligned} x_{k+1} &= \lambda^{-1/2} x_k \\ y_k &= \mathbf{H}_k x_k + v_k, \end{aligned} \tag{5-3}$$

where $\lambda$ is the forgetting factor, with $0 \ll \lambda \leq 1$, and $\mathbf{H}_k$ is the linear time-varying matrix defined in Equation 2-15. In contrast to Equation 5-1, it is now assumed that there is no control input. We can thus define the state matric $A_k = \lambda^{-1/2} I_n$, output matrix $C_k = \mathbf{H}_k$ and measurement noise covariance matrix $I_m$, while $B_k = Q_k = 0$.

With the OE system defined in Equation 5-3, we can check for the same assumptions as for the KF-based estimator. For the initialization of the algorithm, we again find that $x_0 = \mathbf{0} \in \mathbb{R}^n$

and $P_0 = I_n \succ 0$. We also find that both $A_k$ and $R_k$ are square symmetric and positive definite with a strict lower bound. This implies that $A_k$ is invertible as well. The final assumption to be checked is the uniform complete observability of the matrix pair $\{\lambda^{-1/2} I_n, \mathbf{H}_k\}$. Here, we use an assumption that the output matrix can be viewed as an analytically-varying system such that:

$$\mathbf{H}(t) = \begin{bmatrix} \cos(\omega_e t) & -\sin(\omega_e t) & 1 & 0 \\ \sin(\omega_e t) & \cos(\omega_e t) & 0 & 1 \end{bmatrix}, \tag{5-4}$$

where $\omega_e$ is the excitation rotational frequency and $t$ denotes the analytic variable. Let us consider the matrix pair $\{A(t), C(t)\}$ on some time interval $\mathcal{I} = [\tau_0, \tau_1]$ and $t_0 \in \mathcal{I}$ being some arbitrary point in this interval, then observability on $\mathcal{I}$ is equivalent to:

$$\operatorname{rank} \begin{bmatrix} N_0(t_0) \\ N_1(t_0) \\ \vdots \\ N_k(t_0) \end{bmatrix} = n \qquad \text{for some } k, \tag{5-5}$$

where inductively on $i$ we have

$$N_0(t) = C(t), \tag{5-6}$$

and

$$N_{i+1}(t) = N_i(t) A(t) + \frac{d}{dt} N_i(t) \tag{5-7}$$

for $t \in \mathcal{I}$ (see e.g. [75]). Using this method, the analytic matrix pair $\{\lambda^{-1/2} I_n, \mathbf{H}(t)\}$ is found to be observable for the interval $\mathcal{I} = [0, +\infty]$ for all $t \in \mathcal{I}$ and $k \geq 3$. As the state matrix $\lambda^{-1/2} I_n$ is constant for all $t$, this observability property can be extended to a discrete-time case under appropriate conditions. Such conditions imply that

$$\begin{aligned} \frac{d}{dt}\mathbf{H}(t) &= \begin{bmatrix} -\omega_e \sin(\omega_e t) & -\omega_e \cos(\omega_e t) & 0 & 0 \\ \omega_e \cos(\omega_e t) & -\omega_e \sin(\omega_e t) & 0 & 0 \end{bmatrix} \\ &\approx T_s^{-1} \begin{bmatrix} \cos(\omega_e (k+1) T_s) - \cos(\omega_e k T_s) & -\sin(\omega_e (k+1) T_s) + \sin(\omega_e k T_s) & 0 & 0 \\ \sin(\omega_e (k+1) T_s) - \sin(\omega_e k T_s) & \cos(\omega_e (k+1) T_s) - \cos(\omega_e k T_s) & 0 & 0 \end{bmatrix} \\ &= T_s^{-1} \left( \mathbf{H}_{k+1} - \mathbf{H}_k \right), \end{aligned} \tag{5-8}$$

which represents the sampled difference equation with sampling time $T_s$. Hence, if $T_s$ is chosen small enough such that the approximation in Equation 5-8 holds, we have uniform complete observability for the matrix pair $\{\lambda^{-1/2} I_n, \mathbf{H}_k\}$. With this result, we can conclude that all the assumptions for the proof of [70]. Therefore, we find that both the state covariance matrix $P_k$ is positive definite and bounded and the Kalman gain matrix $K_k$ is bounded. The dynamics of the RLS algorithm are thus asymptotically stable as well.

In this section, it was shown that both the KF- and RLS-based estimators have bounded estimator dynamics and are therefore asymptotically stable. This implies that if the input sequence to the adaptive estimators is bounded, the estimate is bounded as well. This property is important for the overall stability of the closed-loop helix synchronization scheme. It does however not guarantee that the estimates are correct and that the downstream turbine thus converges to the phase of the incoming helical wake. In the following section, the stability of the phase convergence of the RLS-based estimator will therefore be assessed.

## 5-2 Stability of the Phase Convergence

As was discussed in Section 2-4-4, the RLS-based estimator is not able to estimate the phase of the helical wake directly. It is only capable to estimate the phase of the tilt and yaw blade bending moments in the $dq$ reference frame. The trick here is to use this phase for the helix method input nonetheless. For this, we consider the following nonlinear difference equation:

$$\phi_{k+1} = \arctan\left(\frac{a\sin(\theta_a) + b\sin(\phi_k + \Delta\psi_0)}{a\cos(\theta_a) + b\cos(\phi_k + \Delta\psi_0)}\right), \tag{5-9}$$

where $\phi_k$ is the estimated phase at discrete-time step $k$, $\theta_a$ is the constant phase of the incoming helical wake, $\Delta\psi_0$ represents the azimuth error, and $a$ and $b$ denote the amplitudes of the helical wake and helix actuation respectively. Both amplitudes are considered to be the amplitudes of the blade blending moments in the $dq$ reference frame at the excitation frequency $\omega_e$. The azimuth error is defined as the amount of phase deviation from the optimal azimuth offset $\psi_0^*$ with $\Delta\psi_0 \in [-\pi, \pi]$. To assess the stability of this system, we first compute the equilibrium points. This computation is done by analyzing Equation 5-9 for the case where $\phi_{k+1} = \phi_k = \bar{\phi}$, with $\bar{\phi}$ being the equilibrium point. The full derivation is shown in Appendix A-3. From this, it is found that all possible equilibrium points are given by:

$$\bar{\phi} = \theta_a - \arcsin\left(-\frac{b}{a}\sin(\Delta\psi_0)\right). \tag{5-10}$$

This relation shows the importance of the inclusion of the azimuth error $\Delta\psi_0$. This is because for the cases where $\Delta\psi_0 = n\pi$, for all $n \in \mathbb{Z}$, the equilibrium point equals $\bar{\phi} = \theta_a$, which is the desired result. It also shows that the equilibrium point of Equation 5-9 depends on the amplitudes of both the incoming and actuated helices. Before we discuss any further implications of this, let us first analyze the stability of the equilibrium points and their region of convergence. For this, the derivative of our nonlinear difference equation has to be evaluated at the equilibrium point. Let us consider the continuous-time function $f(\phi)$ which equals Equation 5-9 for $\phi_k = \phi$. The derivative of this function is given by:

$$\begin{aligned}\frac{d}{d\phi}f(\phi) &= \frac{d}{d\phi}\left(\arctan\left(\frac{a\sin(\theta_a) + b\sin(\phi + \Delta\psi_0)}{a\cos(\theta_a) + b\cos(\phi + \Delta\psi_0)}\right)\right) \\ &= \frac{b(a\cos(\Delta\psi_0 + \phi - \theta_a) + b)}{a^2 + b^2 + 2ab\cos(\Delta\psi_0 + \phi - \theta_a)}.\end{aligned} \tag{5-11}$$

Next, this derivative is evaluated at $\phi = \bar{\phi}$, which results in:

$$\left.\frac{d}{d\phi}f(\phi)\right|_{\phi=\bar{\phi}} = \frac{b(a\cos(p) + b)}{a^2 + b^2 + 2ab\cos(p)}, \tag{5-12}$$

with $p = \Delta\psi_0 - \arcsin\left(-\frac{b}{a}\sin(\Delta\psi_0)\right)$. For Equation 5-10 to be a stable equilibrium point, the absolute value of Equation 5-12 has to be smaller than 1 for it to be stable (see e.g. [76]). For the case where $\Delta\psi_0 = 0$, it is found that $p = 0$, hence

$$\left|\frac{b(a\cos(p) + b)}{a^2 + b^2 + 2ab\cos(p)}\right| = \left|\frac{b}{b + a}\right| < 1 \quad \forall\, a, b > 0, \tag{5-13}$$

where it is assumed that $a$ and $b$ are strictly positive. Likewise, for the case where $\Delta\psi_0 = \pm\pi$, it is found that $p = \pm\pi$ as well, resulting in

$$\left|\frac{b(a\cos(p)+b)}{a^2+b^2+2ab\cos(p)}\right| = \left|\frac{b}{a-b}\right| < 1 \quad \forall\, a > 0,\, 0 < b < \frac{a}{2}. \tag{5-14}$$

Using the knowledge that the stability of an equilibrium point depends on the ratio between $a$ and $b$ and the azimuth error $\Delta\psi_0$, we can compute all values of these parameters for which we have a stable equilibrium. Here, we define $\Delta\bar{\phi} = -\arcsin\left(-\frac{b}{a}\sin(\Delta\psi_0)\right)$ such that the equilibrium point equals $\bar{\phi} = \theta_a + \Delta\bar{\phi}$. Using this, we can map the value of $\Delta\bar{\phi}$ for all ratios of $b/a$ and azimuth errors $\Delta\psi_0$ and find the region of convergence (ROC). This is shown in Figure 5-1, where the purely real value of $\Delta\bar{\phi}$ is depicted for $\Delta\psi_0 \in [-\pi, \pi]$ and $b/a \in [0,\, 10]$.

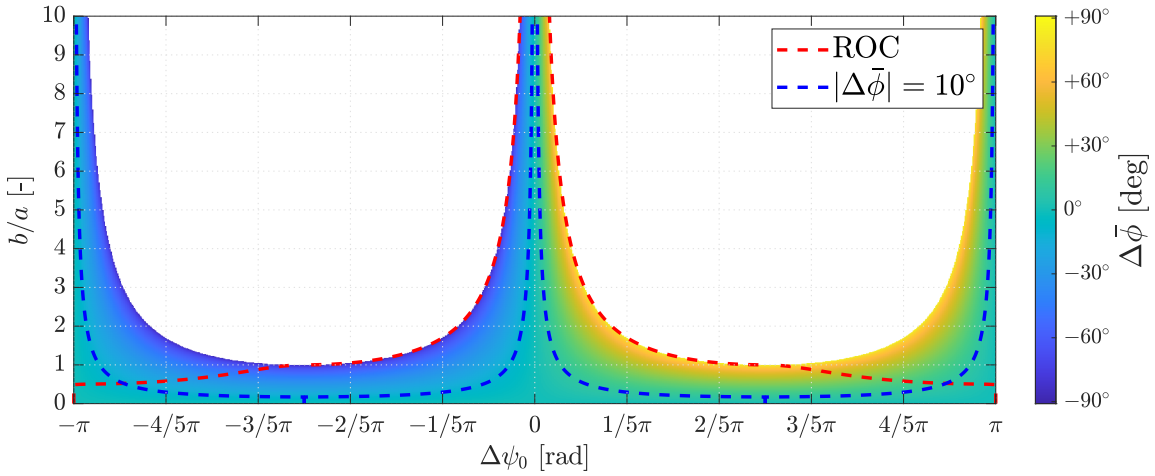



**Figure 5-1:** Purely real-valued part of $\Delta\bar{\phi}$ for the ration $b/a$ and azimuth error $\Delta\psi_0$. $\Delta\bar{\phi}$ represents the part of the equilibrium point that is independent of $\theta_a$ and is equal to $-\arcsin\left(-\frac{b}{a}\sin(\Delta\psi_0)\right)$, with $a$ and $b$ being the amplitudes of the helical wake and helix actuation respectively. Both are assumed to be the blade bending moments in a $dq$ reference framework at the excitation frequency $\omega_e$. The area inside and below the dashed red line indicates the region of convergence (ROC) for which pairs of $b/a$ and $\Delta\psi_0$ will converge to a stable equilibrium point. All the points outside this area are unstable. The area inside and underneath the blue dashed line represents all $\left|\Delta\bar{\phi}\right| \leq 10°$ which would result in a minimum of 99.2% of the attainable interference with the helical wake.

Besides the purely real-valued $\Delta\bar{\phi}$, Figure 5-1 also shows the region of convergence for which the system described by Equation 5-9 will always converge to a stable equilibrium point. For any pair of $\Delta\psi_0$ and the ratio $b/a$ within the area marked with the dashed red line, the system will converge to a stable equilibrium. Likewise, for all pairs outside this area, the system becomes unstable. The blue dashed line indicates all the equilibrium points for which $\left|\Delta\bar{\phi}\right| \leq 10°$. Comparing this to Figure 2-7 shows that all combinations of $b/a$ and $\Delta\psi_0$ inside this area will thus result in a minimal attainable interference of 99.2% with the helical wake. Figure 5-1 therefore gives us a measure of stability and performance for the RLS-based estimator. This will be further elaborated on in the next section.

## 5-3 Note on Robust Stability and Performance

In the first section of this chapter, we evaluated the boundedness and stability of both the KF- and RLS-based estimators. The previous section looked at the stability of the phase convergence for the RLS-based estimator. Both sections gave insight into the nominal stability of both controller schemes. This section will discuss the implications of both results on the robust stability and performance of both methods. First, definitions of a nominal plant for both controllers will be given together with their stability and performance properties. After this, these findings will be translated into robust stability and robust performance measures.

For the KF-based estimator, the nominal model is defined as the KF without model miss-matches and noise. Which therefore has nominal stability as long as the wind turbine itself is operating under stable conditions. This nominal stability is true for partial or full helix wake rejection as well as the phase of the helical inflow is estimated directly. This also implies nominal performance as it can achieve any level of interference with the helical wake through helix pitch actuation under nominal conditions. The nominal plant for the RLS-based estimator can be defined in a few ways. The first nominal plant definition is for helix wake amplification while we have perfect knowledge about the optimal azimuth offset $\psi_0^*$, hence resulting in $\Delta\psi_0 = 0$. Like the KF, the RLS-based estimator has bounded dynamics and is asymptotically stable. From Figure 5-1, we find that in the case of $\Delta\psi_0 = 0$ the estimated phase $\phi_k$ will always converge to the phase of the incoming helix $\theta_a$. On top of that, this also ensures that the estimated phase is always within 100% attainable constructive interference with the incoming helical wake, which equals nominal performance. Other nominal models for the RLS-based estimator can be defined as partial or full wake rejection cases. For these cases, we find that both the nominal stability and performance depend on the ratio $b/a$ (see Figure 5-1). Nonetheless, compared to the nominal KF model, these latter nominal models have worse stability and performance properties. From this, it can be concluded that with a certain plant, the KF-based estimator has the best overall performance.

The robustness properties of the KF-based estimator for the problem of helix wake synchronization have not been studied for this work. Specifically, the stability of the phase estimate under model miss-matches in the KF dynamics. Model miss-matches could lead to incorrect state estimates $\hat{\mathbf{x}}_k$, and thus incorrect $\hat{y}_k$ as well. This in turn could result in the wrong phase estimate. Because of this reason, the RLS estimator was implemented for all experiments where the model was unavailable or uncertain. The robust stability and performance of the RLS method for the problem of helix wake synchronization are mainly defined through the result presented in Figure 5-1. A model miss-match is defined as deviation from the optimal azimuth offset $\psi_0^*$. Additionally, measurement noise, or noise due to turbulence, can end up in the phase estimate through the RLS filter via the harmonics of $\psi(t)$ and $\psi(t)+\omega_e t$ for $M_{dq}$ and $M_{\alpha\beta}$ respectively (see Equation 2-16). In Figure 3-2 it was shown that under nominal conditions the first harmonic of $\psi(t)+\omega_e t$ only has a small contribution to the phase estimate due to the low-pass filter. However, noise at the excitation frequency will result in a noisy estimate, hence noise in $\Delta\psi_0$. For robust stability and performance, we thus have to consider both the azimuth offset error and the amount of noise present in the phase. With this information and for a given $b/a$ we can find the stability and performance using Figure 5-1. One practical issue that was found during the experiments is that more complex wind conditions, such as turbulence, lead to a low SNR at the excitation frequency. This translates to $a < b$, and results in a large $b/a$. The stability and performance margins that are shown in Figure 5-1

for large $b/a$ become tight and do not allow for much noise in $\Delta\psi_0$. Likewise, the error in $\Delta\psi_0$ in this region creates a large variance in $\Delta\bar{\phi}$.

In this chapter, it was shown that both the KF- and RLS-based estimators have bounded and asymptotically stable dynamics. This allows for stable estimates under the assumption that the input is bounded as well. The RLS method also includes the convergence of the phase estimate to that of the helical wake. This section evaluated the stability and performance of this subsystem under nominal and uncertain conditions. It was found that stability issues can arise under low SNR conditions. Both the stability and performance margins have been established by considering the ratio between the amplitudes of the control input and helical wake, as well as an azimuth error. With these margins, the stability and performance of the RLS estimator can be considered along with phase convergence.

# Chapter 6

# Conclusions and Recommendations

## 6-1 Conclusions

This master's thesis investigated the synchronization between a downstream turbine and the incoming helical wake, which launches a novel field in dynamic wake mixing for wind farm control. The hypothesis of this work was that the helix method can be initiated with less pitch actuation in a downstream turbine via synchronization with an incoming helical wake. Therefore, to investigate this, the main research question was formulated as follows:

*How can the wake of an upstream turbine employing the helix method be used to the benefit of a downstream turbine using control?*

---

To answer this question, three sub-questions were formulated in Chapter 1. The results of this master's thesis contributed to answering these questions and formulating the main conclusion of this work.

1. *To what extent can the helix method be initiated in a downstream turbine by using the excitation frequency of the incoming helix wake?*

As was shown in [24], a downstream turbine can measure the helical wake through the Multi-Blade Coordinate (MBC)-transformed blade bending moments. These signals are of interest, as they are also a measure of the helix control action itself. This work demonstrated that key components, such as the phase of the helix, can be extracted from these signals by using adaptive filtering methods. The phase can be used in a closed-loop form to initialize a helix control action which is synchronized with the incoming helical wake. Various control strategies can be implemented to achieve this synchronization. This master's thesis explored the model-free Recursive Least Squares (RLS) estimator with phase convergence and a model-based Kalman Filter (KF) method. Under nominal conditions, the KF was more versatile and showed better performance compared to the RLS method. For uncertain conditions, the RLS

method proved to be a more suitable option, also because it does not require knowledge of the system dynamics. Both methods successfully implemented the helix method in a downstream turbine via in-phase synchronization with the helical wake in both low- and high-order models. Additionally, since the KF method estimates the phase of the input, its estimate is unaffected by any control action, enabling out-of-phase synchronization.

2. *What is the effect of amplifying the helical wake via synchronization on the power production of a waked downstream turbine?*

To answer this question, the synchronization with the helical wake was tested in three different simulation tools with increasing levels of fidelity. In OpenFAST, the control scheme could be evaluated by using helical wind data as input for the model. The synchronization increased the power production of the turbine by a small amount compared to the Baseline (BL) case. However, the validity of this result remains questionable, because OpenFAST is not suited for asymmetric loads in the actuator disc due to large blade deflections. On top of that, the wind data itself has a low spatial resolution and was linearly scaled to match the dimensions of the *NREL 5-MW* turbine. To this end, the synchronization controller was also tested on a two-turbine setup in QBlade. Under steady wind conditions, the downstream turbine was able to synchronize with the incoming helical wake, resulting in a similar power increase as in OpenFAST. This was also tested for inflow with a 5% Turbulence Intensity (TI), which is similar to offshore wind conditions. Although the turbine was able to synchronize with the incoming helical wake, the power generation was less compared to a BL case. The final synchronization test was performed in SOWFA for a three-turbine setting. The results showed that both T2 and T3 did not benefit from helix wake synchronization in terms of power generation compared to the BL case.

3. *What is the effect of rejecting the helical wake via synchronization on the power production of a multi-turbine setting?*

In addition to in-phase synchronization, strategies for out-of-phase downstream wake mixing were also investigated in this work. In the low-order SM model, OpenFAST and SOWFA, this concept was experimented with. The KF-based estimator was used in the low-order model and OpenFAST to synchronize 90° and 180° out-of-phase. These represent partial and complete rejection, respectively. In OpenFAST, complete rejection resulted in the reduction of the MBC-transformed blade bending moments. Furthermore, the partial rejection method did not lower these moments significantly. During the SOWFA simulations, partial wake rejection was also achieved by slowly varying the helix phase in T2. It was found that at the $-90°$ out-of-phase with the incoming helical wake, the combined three-turbine setup benefited significantly in terms of power production for steady wind conditions.

With these sub-questions answered, we find that in-phase or out-of-phase synchronizing of the helix method with the incoming helical wake can be beneficial for a downstream turbine in terms of power production under suitable wind conditions. The three simulation tools used for this thesis each give a different insight into the benefits of the different kinds of synchronization with an incoming helical wake. As of today, no research has been done on the topic of wake synchronization in downstream turbines for wake mixing strategies. This thesis, therefore,

serves as an initial step toward dynamic wake mixing strategies using synchronization in a multi-turbine setting. Because of this, more research has to be done to further investigate and develop this concept. The next section will thus present recommendations for future work to explore this topic.

## 6-2 Recommendations

This master's thesis took the first steps in research on wake synchronization, but the potential is clear: significant performance increases can be achieved in a multi-turbine setup, as shown by Computational Fluid Dynamics (CFD) simulations. Since this work was limited, future research should prove its full potential. This section discusses three topics with recommendations for future research.

1. *Investigate the potential of partial helix wake rejection in SOWFA under turbulent wind conditions.*

Although it was shown in QBlade that for low TI the downstream turbine was not able to benefit from the helical wake in terms of power generation, the excitation frequency was present in the BL case. This implies that the phase of this wake can nevertheless be measured and synchronized with it. Combining this with the final result from SOWFA, we find that this helical wake could be disturbed by partial helix wake rejection. This could potentially lead to an increase in wake mixing, allowing T3 to benefit from an accelerated wake recovery. Such an experiment is not limited to SOWFA, but could also be investigated in other high-fidelity tools, such as AMR-Wind [77]. The next step would be to test this in wind tunnel experiments on scaled wind turbines or in field tests.

2. *Study the effect of different wind conditions on the phase and frequency of the helical wake for synchronization.*

This thesis was mainly constrained to steady wind conditions and perpendicular flow to the rotor disc. Helix wake synchronization was tested using low TI wind inflow with a realistic boundary layer. However, other wake effects such as wake meandering were not considered. Likewise, the influence of partial wake overlap on synchronization capabilities remains unknown. This report also provided an analysis of the error sensitivity in the phase estimate for the RLS method. This can be translated into a performance measure under uncertainty in the phase. However, uncertainty in the frequency is not taken into account for this work. Quantifying the effect of various changes in the wind on the frequency and phase of the helical wake can help in improving the helix wake synchronization controller design.

3. *Improve the current controller designs for optimal helix wake synchronization.*

The two controllers used throughout this thesis showed good performance under steady wind conditions. The effect of model miss-matches for the KF-based estimator has not been investigated in this work. Because of this, the RLS method was chosen over the KF, as only an

azimuth offset had to be determined. However, the RLS method showed poor performance under partial or complete wake rejection due to the instabilities in the phase convergence method that was implemented. The RLS method could therefore be improved by alleviating the phase convergence such that it can cope with out-of-phase synchronization. Likewise, the KF method could be improved by extending it to an Linear Parameter-Varying (LPV) setting for multiple wind speeds, or an extended Kalman filter (EKF) to incorporate the nonlinear dynamics of the wind turbine. The entire controller design could also be overhauled by implementing state-of-the-art sensor technology, such as LiDAR or smart rotor designs. These methods could be used to estimate the frequency, phase, and possibly more useful parameters of an incoming helical wake in a novel controller strategy.

# Appendix A

# Mathematical Derivations

## A-1 Using a DC-offset for Phase Estimation

Assume the MOoP signals have been converted to their respective tilt and yaw moments ($T_p(\psi(t))$ transformation), and that these moments can be described by sinusoidal functions with frequency $\omega_e$. Thus, these moments can be given by

$$\begin{aligned} M_{tilt} &:= x_1 = A_1 \sin(\omega_e t + \phi) + d_1 \\ M_{yaw} &:= x_2 = A_2 \cos(\omega_e t + \phi) + d_2. \end{aligned} \tag{A-1}$$

where $A_1$ and $A_2$ are the amplitudes, $\omega_e$ is the frequency, $\phi$ the phase and $d_1$ and $d_2$ are DC offsets. Next, we rotate the matrix at each time step using

$$\begin{bmatrix} y_1 \\ y_2 \end{bmatrix} = \underbrace{\begin{bmatrix} \cos(\omega_e t) & -\sin(\omega_e t) \\ \sin(\omega_e t) & \cos(\omega_e t) \end{bmatrix}}_{T_{dq}(\omega_e t)} \begin{bmatrix} x_1 \\ x_2 \end{bmatrix}, \tag{A-2}$$

where

$$\hat{M}_{tilt} := y_1, \quad \hat{M}_{yaw} := y_2 \tag{A-3}$$

are the tilt and yaw moments resulting from a $T_p(\psi(t) + \omega_e t)$ transformation.

$$\begin{aligned} y_1 &= x_1 \cos(\omega_e t) - x_2 \sin(\omega_e t) \\ &= A_1 \sin(\omega_e t + \phi)\cos(\omega_e t) - A_2 \cos(\omega_e t + \phi)\sin(\omega_e t) + d_1 \cos(\omega_e t) - d_2 \sin(\omega_e t). \end{aligned} \tag{A-4}$$

If $\boldsymbol{A_1 = A_2}$, we get

$$\begin{aligned} y_1 &= A_1 \sin(\omega_e t + \phi)\cos(\omega_e t) - A_2 \cos(\omega_e t + \phi)\sin(\omega_e t) + d_1 \cos(\omega_e t) - d_2 \sin(\omega_e t) \\ &= A_1 \sin(\omega_e t + \phi - \omega_e t) + d_1 \cos(\omega_e t) - d_2 \sin(\omega_e t) \\ &= A_1 \sin(\phi) + d_1 \cos(\omega_e t) + d_2 \cos\left(\omega_e t + \frac{\pi}{2}\right). \end{aligned} \tag{A-5}$$

Using the relation $a\sin(x+\theta_a)+b\sin(x+\theta_b)=c\sin(x+\theta)$, we get

$$y_1 = \underbrace{A_1\sin(\phi)}_{\text{DC component}} + \underbrace{c\cos(\omega_e t+\theta)}_{\text{Frequency component}} . \tag{A-6}$$

If $\boldsymbol{A_1 \neq A_2}$, we get

$$\begin{aligned} y_1 &= A_1\sin(\omega_e t+\phi)\cos(\omega_e t) - A_2\cos(\omega_e t+\phi)\sin(\omega_e t) + d_1\cos(\omega_e t) - d_2\sin(\omega_e t) \\ &= \frac{1}{2}\left[(A_1+A_2)\sin(\omega_e t+\phi-\omega_e t) + (A_1-A_2)\sin(\omega_e t+\phi+\omega_e t)\right] + d_1\cos(\omega_e t) - d_2\sin(\omega_e t) \\ &= \frac{1}{2}(A_1+A_2)\sin(\phi) + \frac{1}{2}(A_1-A_2)\sin(2\omega_e t+\phi) + c\cos(\omega_e t+\theta). \end{aligned} \tag{A-7}$$

Which can be simplified as

$$y_1 = \underbrace{D_1\sin(\phi)}_{\text{DC component}} + \underbrace{D_2\sin(2\omega_e t+\phi)+c\cos(\omega_e t+\theta)}_{\text{Frequency component}}. \tag{A-8}$$

Regardless of whether $A_1 = A_2$ or $A_1 \neq A_2$, we find that the DC component always contains the phase information $\phi$. A similar derivation can be done for $y_2$. This will result in a DC component equal to $\frac{1}{2}(A_1+A_2)\cos(\phi) = D_1\cos(\phi)$.

$$y_2 = \underbrace{D_1\cos(\phi)}_{\text{DC component}} - \underbrace{D_2\cos(2\omega_e t+\phi)+c\sin(\omega_e t+\theta)}_{\text{Frequency component}}. \tag{A-9}$$

## A-2 Bound on $\Delta\phi$

Given is the trigonometric identity:

$$a\sin(\omega t+\theta_a)+b\sin(\omega t+\theta_b)=c\sin(\omega t+\phi). \tag{A-10}$$

With constants $a, b, c \in \mathbb{R}_{>0}$ and some frequency $\omega \in \mathbb{R}$. We are interested in finding bounds on $\theta_b$, such that $c$ is sufficiently larger. At the case where $\theta_a = \theta_b$, the amplitude is given by $c = a + b$ which equals constructive (maximum) interference. Sufficiently large is, therefore, defined as $|\theta_a - \theta_b| \leq \Delta\psi$. Destructive (minimum) interference occurs at $\theta_b = \theta_a - \pi$, hence, we define $\theta_a = 0$ and $\theta_b \in [0, \pi]$. Equation A-10 can be rewritten for the variable $c$ as a function of $\theta_b$, $a$ and $b$ as follows:

$$c(a,b,\theta_b) = \sqrt{a^2+b^2+2ab\cos(\theta_b)}. \tag{A-11}$$

This function can be scaled to map its output between 0 and 1. This can be achieved by subtracting the value of minimum interference, $|a-b|$, and dividing by the difference between the maximum and minimum interference. This gives:

$$\Sigma(a,b,\theta_b) = \frac{\sqrt{a^2+b^2+2ab\cos(\theta_b)}-|a-b|}{a+b-|a-b|}, \quad \text{where } a,b>0, \tag{A-12}$$

which now satisfies $\Sigma(a, b, \theta_b) \in [0, 1]$. For any positive $a$ and positive $b$ pair, there exists a function $\Sigma_{ab}(\theta_b) \in \mathcal{S}$, where $\mathcal{S}$ is the set of all possible functions that satisfy Equation A-12. The lowest bound $\Delta\psi$ is defined by the lowest possible function $\Sigma_{ab}(\theta_b)$. This is given by:

$$\Sigma_{ab}^{-}(\theta_b) = \inf\{\Sigma(a, b, \theta_b) \in \mathcal{S} : a, b > 0\}, \tag{A-13}$$

where inf denotes the infimum. One condition for $\Sigma_{ab}^{-}(\theta_b)$ is that its area under the curve should be the minimum. We therefore compute:

$$\int_0^{\pi} \frac{\sqrt{a^2 + b^2 + 2ab\cos(\theta_b)} - |a - b|}{a + b - |a - b|} d\theta_b = \left[ \frac{-\theta_b|a - b| + 2|a - b|E(\frac{\theta_b}{2} \mid \frac{4ab}{(a+b)^2})}{a + b - |a - b|} \right]_0^{\pi}, \tag{A-14}$$

for which the equality holds due to $a, b, \theta_b \in \mathbb{R}$. Here, $E(\phi \mid k^2)$ denotes the elliptic integral which is given by:

$$E(\phi \mid k^2) = \int_0^{\phi} \sqrt{1 - k^2 \sin^2\theta} d\theta, \tag{A-15}$$

where $E(0 \mid k^2) = 0$. Evaluating the right side of Equation A-14, therefore, gives:

$$\frac{-\pi|a - b| + 2|a - b|E(\frac{\pi}{2} \mid \frac{4ab}{(a+b)^2})}{a + b - |a - b|} - 0. \tag{A-16}$$

The smallest non-zero area can be found by taking either the limit $\lim_{a\to\infty}$ or $\lim_{b\to\infty}$. For e.g. $\lim_{a\to\infty}$, this can be viewed as $a$ being infinitely larger than $b$. Therefore, deviation from the phase $\theta_a$ leads to the largest reduction in amplitude compared to maximum interference. The limit is computed using *WolframAlpha*. The result is given by:

$$\lim_{a\to\infty} \frac{-\pi|a - b| + 2|a - b|E(\frac{\pi}{2} \mid \frac{4ab}{(a+b)^2})}{a + b - |a - b|} = \frac{\pi}{2}, \quad \forall\, b > 0. \tag{A-17}$$

Hence, the lowest $\Sigma_{ab}(\theta_b)$ should satisfy:

$$\int_0^{\pi} \Sigma_{ab}^{-}(\theta_b) = \frac{\pi}{2}. \tag{A-18}$$

Computing the same limit for Equation A-12 gives:

$$\lim_{a\to\infty} \Sigma(a, b, \theta_b) = \lim_{a\to\infty} \frac{\sqrt{a^2 + b^2 + 2ab\cos(\theta_b)} - |a - b|}{a + b - |a - b|} = \cos^2\left(\frac{\theta_b}{2}\right). \tag{A-19}$$

We can therefore conclude that $\Sigma_{ab}^{-}(\theta_b) = \cos^2\left(\frac{\theta_b}{2}\right)$ is the smallest possible curve in the set $\mathcal{S}$ for which $a, b \in \mathbb{R}_{>0}$.

## A-3 Equilibrium Points Phase Convergence

We consider the nonlinear difference equation given in Equation 5-9. This section serves as proof for the stability assessment of this system shown in chapter 5. First, the equilibrium points of Equation 5-9 are computed. This is done by analyzing the case where $\phi_{k+1} = \phi_k = \bar{\phi}$:

$$\tan\left(\bar{\phi}\right) = \frac{a\sin(\theta_a) + b\sin\left(\bar{\phi} + \Delta\psi_0\right)}{a\cos(\theta_a) + b\cos\left(\bar{\phi} + \Delta\psi_0\right)}, \tag{A-20}$$

where we took the tangent of both sides. The denominator of the right side is brought to the left and using trigonometric identities we find that Equation A-20 can be rewritten as:

$$\begin{aligned}\left(a\cos(\theta_a)+b\left[\cos(\Delta\psi_0)\ -\sin(\Delta\psi_0)\right]\begin{bmatrix}\cos\left(\bar{\phi}\right)\\ \sin\left(\bar{\phi}\right)\end{bmatrix}\right)\tan\left(\bar{\phi}\right) &= a\sin(\theta_a)\dots\\ &\quad\dots+b\left[\cos(\Delta\psi_0)\ \sin(\Delta\psi_0)\right]\begin{bmatrix}\sin\left(\bar{\phi}\right)\\ \cos\left(\bar{\phi}\right)\end{bmatrix}\\ a\cos(\theta_a)\tan\left(\bar{\phi}\right)+b\left[\cos(\Delta\psi_0)\ -\sin(\Delta\psi_0)\right]\begin{bmatrix}\sin\left(\bar{\phi}\right)\\ \frac{\sin^2(\bar{\phi})}{\cos\left(\bar{\phi}\right)}\end{bmatrix} &= a\sin(\theta_a)\dots\\ &\quad\dots+b\left[\cos(\Delta\psi_0)\ \sin(\Delta\psi_0)\right]\begin{bmatrix}\sin\left(\bar{\phi}\right)\\ \cos\left(\bar{\phi}\right)\end{bmatrix}.\end{aligned} \tag{A-21}$$

Next, $b\cos(\Delta\psi_0)\sin\left(\bar{\phi}\right)$ can be removed from both sides, leaving:

$$\begin{aligned}a\cos(\theta_a)\tan\left(\bar{\phi}\right)-b\sin(\Delta\psi_0)\frac{\sin^2(\bar{\phi})}{\cos\left(\bar{\phi}\right)} &= a\sin(\theta_a)+b\sin(\Delta\psi_0)\cos\left(\bar{\phi}\right)\\ a\cos(\theta_a)\tan\left(\bar{\phi}\right)-b\sin(\Delta\psi_0)\underbrace{\left(\frac{\sin^2(\bar{\phi})}{\cos\left(\bar{\phi}\right)}+\cos\left(\bar{\phi}\right)\right)}_{\sec\left(\bar{\phi}\right)} &= a\sin(\theta_a)\\ a\cos(\theta_a)\tan\left(\bar{\phi}\right)-b\sin(\Delta\psi_0)\sec\left(\bar{\phi}\right) &= a\sin(\theta_a),\end{aligned} \tag{A-22}$$

where we now have a secant term on the left side. We can bring this secant term outside as follows:

$$\begin{aligned}a\cos(\theta_a)\tan\left(\bar{\phi}\right)-b\sin(\Delta\psi_0)\sec\left(\bar{\phi}\right) &= a\sin(\theta_a)\\ \sec\left(\bar{\phi}\right)\left(a\sin\left(\theta_a-\bar{\phi}\right)+b\sin(\Delta\psi_0)\right) &= 0.\end{aligned} \tag{A-23}$$

Next, we want to solve this equation for our equilibrium point $\bar{\phi}$. This gives the two equalities given by:

$$\sec\left(\bar{\phi}\right)=0\vee\left(a\sin\left(\theta_a-\bar{\phi}\right)+b\sin(\Delta\psi_0)\right)=0, \tag{A-24}$$

where we note that $\sec\left(\bar{\phi}\right)\neq 0$ for all $\bar{\phi}$. Hence, we only consider the right equality, which results in the following equilibrium point:

$$\bar{\phi}=\theta_a-\arcsin\left(-\frac{b}{a}\sin(\Delta\psi_0)\right). \tag{A-25}$$

# Appendix B

# MBC Transformation Second-Order System

This appendix gives the derivation of the second-order equations of motion of a three-bladed wind turbine, which is used for the linearization shown in Equation 4-3. This derivation is adapted from [23].

The second-order system may be defined as a mass-spring-damper system written as:

$$M\ddot{X} + C\dot{X} + KX = Fu + F_d w, \tag{B-1}$$

with output equations given as:

$$Y = C_v\dot{X} + C_d X + Du + D_d w. \tag{B-2}$$

Here, $M$, $C$, $K$, $F$, and $F_d$ are the mass, damping, stiffness, control, and disturbance matrices respectively. The vectors $u$, $w$, and $Y$ denote the control inputs, disturbances, and outputs respectively. $X$ represents the physical vector containing a total of $nF + 3m$ degrees of freedom. Here, $nF$ is the number of fixed-frame-referenced degrees of freedom, and $m$ is the number of rotating degrees of freedom for each blade. Hence, $m$ is multiplied by 3. This vector can be transformed to a non-rotating framework $X_{NR}$ via:

$$T_1 = \begin{bmatrix} I_{nF\times nF} & & & \\ & \tilde{t}_1 & & \\ & & \ddots & \\ & & & \tilde{t}_1 \end{bmatrix}, \quad \text{with} \quad \tilde{t}_1 = \begin{bmatrix} 1 & \cos(\psi_1) & \sin(\psi_1) \\ 1 & \cos(\psi_2) & \sin(\psi_2) \\ 1 & \cos(\psi_3) & \sin(\psi_3) \end{bmatrix}, \tag{B-3}$$

where $T_1 \in \mathbb{R}^{(nF+3m)\times(nF+3m)}$. The matrix $\tilde{t}_1$ is equivalent to the backward MBC-transformation given in Equation 2-6. By computing the first and second time derivatives of this transformation, we can compute the following set of equations:

$$\begin{aligned} X &= T_1 X_{NR} \\ \dot{X} &= T_1\dot{X}_{NR} + \omega_r T_2 X_{NR} \\ \ddot{X} &= T_1\ddot{X}_{NR} + 2\omega_r T_2\dot{X}_{NR} + (\omega_r^2 T_3 + \dot{\omega}_r T_2)X_{NR}. \end{aligned} \tag{B-4}$$

As a result of the time derivatives, $T_2$ and $T_3$ are defined as followed. The $T_2$ matrix is described by:

$$T_2 = \begin{bmatrix} \mathbf{0}_{nF\times nF} & & & \\ & \tilde{t}_2 & & \\ & & \ddots & \\ & & & \tilde{t}_2 \end{bmatrix}, \quad \text{with} \quad \tilde{t}_2 = \begin{bmatrix} 0 & -\sin(\psi_1) & \cos(\psi_1) \\ 0 & -\sin(\psi_2) & \cos(\psi_2) \\ 0 & -\sin(\psi_3) & \cos(\psi_3) \end{bmatrix}, \tag{B-5}$$

where $T_2 \in \mathbb{R}^{(nF+3m)\times(nF+3m)}$. Likewise, $T_3$ is defined as:

$$T_3 = \begin{bmatrix} \mathbf{0}_{nF\times nF} & & & \\ & \tilde{t}_3 & & \\ & & \ddots & \\ & & & \tilde{t}_3 \end{bmatrix}, \quad \text{with} \quad \tilde{t}_3 = \begin{bmatrix} 0 & -\cos(\psi_1) & -\sin(\psi_1) \\ 0 & -\cos(\psi_2) & -\sin(\psi_2) \\ 0 & -\cos(\psi_3) & -\sin(\psi_3) \end{bmatrix}, \tag{B-6}$$

with $T_3 \in \mathbb{R}^{(nF+3m)\times(nF+3m)}$. Substituting for $X$ and its time derivatives from Equation B-4 in equations Equation B-1 and Equation B-2, we get the following equations of motion in non-rotating reference frame:

$$M_{NR}\ddot{X}_{NR} + C_{NR}\dot{X}_{NR} + K_{NR}X_{NR} = F_{NR}u_{NR} + F_{d\,NR}w. \tag{B-7}$$

Similarly, the output is described by:

$$Y_{NR} = C_{v\,NR}\dot{X}_{NR} + C_{d\,NR}X_{NR} + D_{NR}u_{NR} + D_{d\,NR}w \tag{B-8}$$

The subscript $NR$ denotes that the quantity is in the non-rotating reference frame. The remaining matrices are defined as follows:

$$\begin{aligned} M_{NR} &= MT_1 \\ C_{NR} &= 2\omega_r MT_2 + CT_1 \\ K_{NR} &= \omega_r^2 MT_3 + \dot{\omega_r} MT_2 + \omega_r CT_2 + KT_1 \\ F_{NR} &= FT_{1C} \\ F_{d\,NR} &= F_d \\ C_{v\,NR} &= T_{1O}^{-1} C_v T_1 \\ C_{d\,NR} &= T_{1O}^{-1}(\omega_r C_v T_2 + C_d T_1) \\ D_{NR} &= T_{1O}^{-1} D T_{1C} \\ D_{d\,NR} &= T_{1O}^{-1} D_d \end{aligned} \tag{B-9}$$

Note that the disturbance matrix remains unchanged, as the disturbance $w$ is already in the non-rotating framework. The control input and system output vectors can be transformed via $u = T_{1C}u_{NR}$ and $Y = T_{1O}Y_{NR}$ respectively. Here, these matrices are defined as:

$$T_{1C} = \begin{bmatrix} I_{F_C\times F_C} & & & \\ & \tilde{t}_1 & & \\ & & \ddots & \\ & & & \tilde{t}_1 \end{bmatrix}, \quad T_{1O} = \begin{bmatrix} I_{F_O\times F_O} & & & \\ & \tilde{t}_1 & & \\ & & \ddots & \\ & & & \tilde{t}_1 \end{bmatrix}, \tag{B-10}$$

with $T_{1C} \in \mathbb{R}^{(F_C+3m_C)\times(F_C+3m_C)}$ and $T_{1O} \in \mathbb{R}^{(F_O+3m_O)\times(F_O+3m_O)}$, where $F_C$ and $F_O$ are the number of fixed-frame control inputs and outputs and $m_C$ and $m_O$ are the number of rotating control inputs and outputs.

# Appendix C

# OpenFAST & QBlade Results

## C-1 OpenFAST: Synchronization

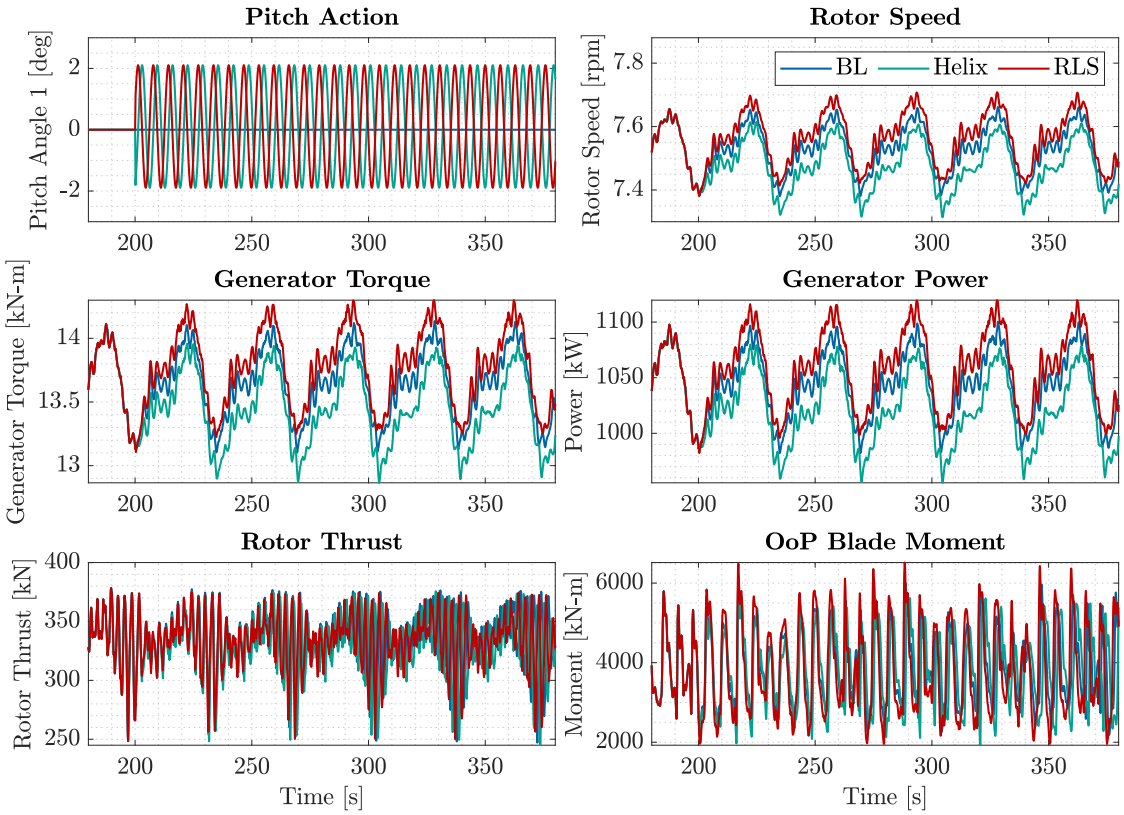



**Figure C-1:** Time domain simulation results of power and load related signals for a baseline, Helix, and synchronized Helix controller in OpenFAST. The data corresponds to the synchronization experiment from Section 4-4-4.

## C-2 QBlade: Synchronization

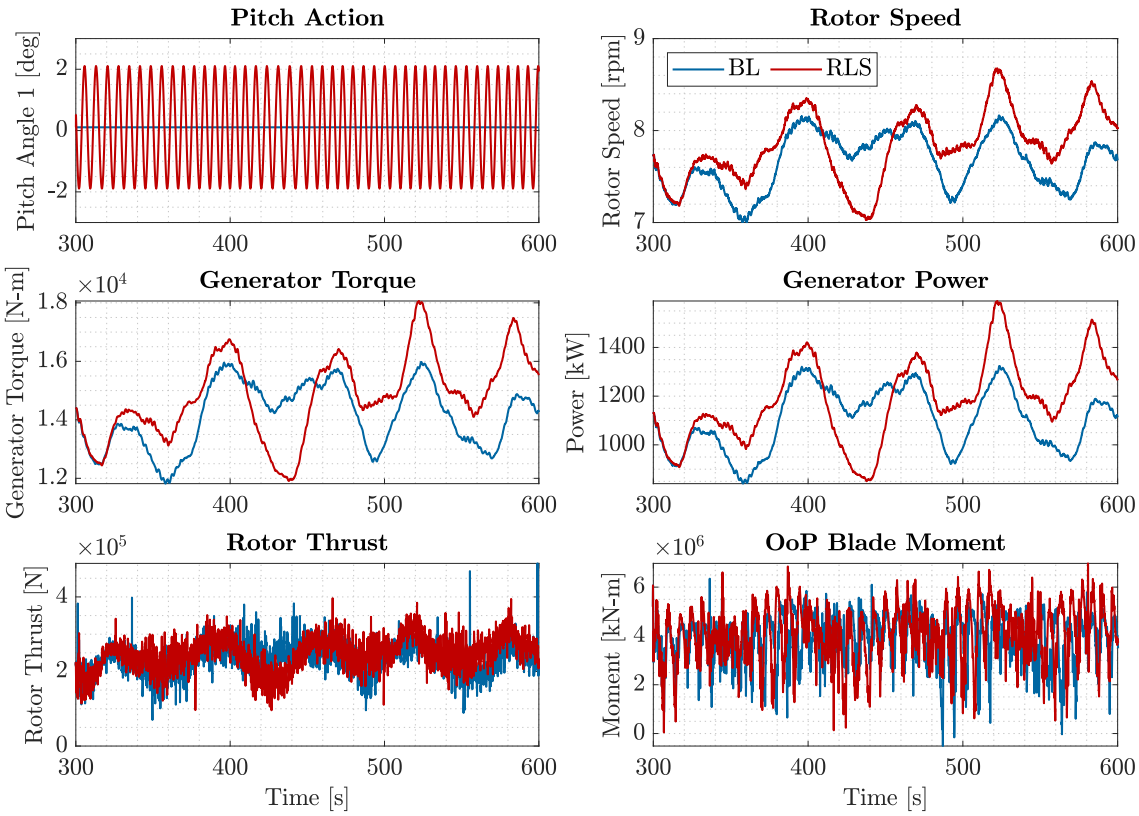



**Figure C-2:** Time domain simulation results of power and load related signals for a baseline, Helix, and synchronized Helix controller in QBlade. The data corresponds to the synchronization experiment with low TI and boundary layer with $\alpha = 0.08$ from Figure 4-10.

# Bibliography


[1] N. Jenkins, T. Burton, E. Bossanyi, D. Sharpe, and M. Graham, *Wind Energy Handbook 3e*. Wiley, Apr. 2021. DOI: 10.1002/9781119451143.

[2] T. Burton, N. Jenkins, D. Sharpe, and E. Bossanyi, *Wind Energy Handbook*. Wiley, May 2011. DOI: 10.1002/9781119992714.

[3] A. Betz, "Das maximum der theoretisch möglichen ausnutzung des windes durch windmotoren," *Zeitschrift für das gesamte Turbinenwesen*, pp. 307–309, 1920.

[4] E. Gaertner, J. Rinker, L. Sethuraman, *et al.*, "Iea wind tcp task 37: Definition of the iea 15-megawatt offshore reference wind turbine," Mar. 2020. DOI: 10.2172/1603478.

[5] K. Thomsen and P. Sørensen, "Fatigue loads for wind turbines operating in wakes," *Journal of Wind Engineering and Industrial Aerodynamics*, vol. 80, no. 1-2, pp. 121–136, Mar. 1999. DOI: 10.1016/s0167-6105(98)00194-9.

[6] J. Bossuyt, M. F. Howland, C. Meneveau, and J. Meyers, "Measurement of unsteady loading and power output variability in a micro wind farm model in a wind tunnel," *Experiments in Fluids*, vol. 58, no. 1, Dec. 2016. DOI: 10.1007/s00348-016-2278-6.

[7] M. T. van Dijk, J. W. van Wingerden, T. Ashuri, and Y. Li, "Wind farm multi-objective wake redirection for optimizing power production and loads," *Energy*, vol. 121, pp. 561–569, Feb. 2017. DOI: 10.1016/j.energy.2017.01.051.

[8] P. A. Fleming, P. Gebraad, S. Lee, *et al.*, "Evaluating techniques for redirecting turbine wakes using SOWFA," *Renewable Energy*, vol. 70, pp. 211–218, Oct. 2014. DOI: 10.1016/j.renene.2014.02.015.

[9] R. J. Barthelmie, K. Hansen, S. T. Frandsen, *et al.*, "Modelling and measuring flow and wind turbine wakes in large wind farms offshore," *Wind Energy*, vol. 12, no. 5, pp. 431–444, Jul. 2009. DOI: 10.1002/we.348.

[10] S. Boersma, B. M. Doekemeijer, P. M. O. Gebraad, *et al.*, "A tutorial on control-oriented modeling and control of wind farms," in *2017 American Control Conference (ACC)*, IEEE, May 2017. DOI: 10.23919/acc.2017.7962923.

[11] J. Meyers, C. Bottasso, K. Dykes, *et al.*, "Wind farm flow control: Prospects and challenges," Mar. 2022. DOI: 10.5194/wes-2022-24.

[12] C. L. Bottasso and F. Campagnolo, "Wind tunnel testing of wind turbines and farms," in *Handbook of Wind Energy Aerodynamics*, Springer International Publishing, 2021, pp. 1–57. DOI: 10.1007/978-3-030-05455-7_54-1.

[13] D. van der Hoek, S. Kanev, J. Allin, D. Bieniek, and N. Mittelmeier, "Effects of axial induction control on wind farm energy production - a field test," *Renewable Energy*, vol. 140, pp. 994–1003, Sep. 2019. DOI: 10.1016/j.renene.2019.03.117.

[14] C. Santoni, U. Ciri, M. Rotea, and S. Leonardi, "Development of a high fidelity CFD code for wind farm control," in *2015 American Control Conference (ACC)*, IEEE, Jul. 2015. DOI: 10.1109/acc.2015.7170980.

[15] P. Fleming, J. Annoni, J. J. Shah, *et al.*, "Field test of wake steering at an offshore wind farm," *Wind Energy Science*, vol. 2, no. 1, pp. 229–239, May 2017. DOI: 10.5194/wes-2-229-2017.

[16] M. F. Howland, S. K. Lele, and J. O. Dabiri, "Wind farm power optimization through wake steering," *Proceedings of the National Academy of Sciences*, vol. 116, no. 29, pp. 14 495–14 500, Jul. 2019. DOI: 10.1073/pnas.1903680116.

[17] B. M. Doekemeijer, S. Kern, S. Maturu, *et al.*, "Field experiment for open-loop yaw-based wake steering at a commercial onshore wind farm in italy," *Wind Energy Science*, vol. 6, no. 1, pp. 159–176, Jan. 2021. DOI: 10.5194/wes-6-159-2021.

[18] S. G. R. Energy. "Wake adapt." (2019), [Online]. Available: https://www.siemensgamesa.com/en-int/newsroom/2019/11/191126-siemens-gamesa-wake-adapt-en (visited on 06/29/2022).

[19] J. P. Goit and J. Meyers, "Optimal control of energy extraction in wind-farm boundary layers," *Journal of Fluid Mechanics*, vol. 768, pp. 5–50, Feb. 2015. DOI: 10.1017/jfm.2015.70.

[20] W. Munters and J. Meyers, "Towards practical dynamic induction control of wind farms: Analysis of optimally controlled wind-farm boundary layers and sinusoidal induction control of first-row turbines," *Wind Energy Science*, vol. 3, no. 1, pp. 409–425, Jun. 2018. DOI: 10.5194/wes-3-409-2018.

[21] J. A. Frederik, R. Weber, S. Cacciola, *et al.*, "Periodic dynamic induction control of wind farms: Proving the potential in simulations and wind tunnel experiments," *Wind Energy Science*, vol. 5, no. 1, pp. 245–257, Feb. 2020. DOI: 10.5194/wes-5-245-2020.

[22] J. A. Frederik, B. M. Doekemeijer, S. P. Mulders, and J. W. van Wingerden, "The helix approach: Using dynamic individual pitch control to enhance wake mixing in wind farms," *Wind Energy*, vol. 23, no. 8, pp. 1739–1751, 2020. DOI: https://doi.org/10.1002/we.2513.

[23] G. Bir, "Multi-blade coordinate transformation and its application to wind turbine analysis," in *46th AIAA Aerospace Sciences Meeting and Exhibit*, American Institute of Aeronautics and Astronautics, Jan. 2008. DOI: 10.2514/6.2008-1300.

[24] J. A. Frederik and J. W. van Wingerden, "On the load impact of dynamic wind farm wake mixing strategies," *Renewable Energy*, vol. 194, pp. 582–595, 2022, ISSN: 0960-1481. DOI: https://doi.org/10.1016/j.renene.2022.05.110.

[25] M. Stammler, P. Thomas, A. Reuter, F. Schwack, and G. Poll, "Effect of load reduction mechanisms on loads and blade bearing movements of wind turbines," *Wind Energy*, vol. 23, no. 2, pp. 274–290, 2020. DOI: https://doi.org/10.1002/we.2428.

[26] M. Stammler, A. Reuter, and G. Poll, "Cycle counting of roller bearing oscillations case study of wind turbine individual pitching system," *Renewable Energy Focus*, vol. 25, pp. 40–47, Jun. 2018. DOI: 10.1016/j.ref.2018.02.004.

[27] C. Muscari, P. Schito, A. Viré, A. Zasso, D. van der Hoek, and J. W. van Wingerden, "Physics informed DMD for periodic dynamic induction control of wind farms," *Journal of Physics: Conference Series*, vol. 2265, no. 2, p. 022 057, May 2022. DOI: 10.1088/1742-6596/2265/2/022057.

[28] R. P. Coleman and A. M. Feingold, "Theory of self-excited mechanical oscillations of helicopter rotors with hinged blades," Tech. Rep., 1957.

[29] R. H. Park, "Two-reaction theory of synchronous machines generalized method of analysis-part i," *Transactions of the American Institute of Electrical Engineers*, vol. 48, no. 3, pp. 716–727, Jul. 1929. DOI: 10.1109/t-aiee.1929.5055275.

[30] C. J. O'Rourke, M. M. Qasim, M. R. Overlin, and J. L. Kirtley, "A geometric interpretation of reference frames and transformations: Dq0, clarke, and park," *IEEE Transactions on Energy Conversion*, vol. 34, no. 4, pp. 2070–2083, Dec. 2019. DOI: 10.1109/tec.2019.2941175.

[31] G. S. Bir, "User's guide to MBC3: Multi-blade coordinate transformation code for 3-bladed wind turbine," Tech. Rep., Sep. 2010. DOI: 10.2172/989416.

[32] E. Clarke, "Determination of voltages and currents during unbalanced faults," *General Electric Review*, vol. 40, no. 11, pp. 511–513, 1937.

[33] E. van Solingen and J. van Wingerden, "Linear individual pitch control design for two-bladed wind turbines," *Wind Energy*, vol. 18, no. 4, pp. 677–697, Feb. 2014. DOI: 10.1002/we.1720.

[34] M. H. Hayes, *Statistical Digital Signal Processing and Modeling*, 1st. USA: John Wiley Sons, Inc., 1996, ISBN: 0471594318.

[35] E. A. Bossanyi, "Individual blade pitch control for load reduction," *Wind Energy*, vol. 6, no. 2, pp. 119–128, 2003. DOI: 10.1002/we.76.

[36] S. P. Mulders, A. K. Pamososuryo, G. E. Disario, and J.-W. van Wingerden, "Analysis and optimal individual pitch control decoupling by inclusion of an azimuth offset in the multiblade coordinate transformation," *Wind Energy*, vol. 22, no. 3, pp. 341–359, Nov. 2018. DOI: 10.1002/we.2289.

[37] V. Madisetti, *Digital Signal Processing Fundamentals*. CRC Press, Nov. 2009. DOI: 10.1201/9781420046076.

[38] Q. Lu, R. Bowyer, and B. L. Jones, "Analysis and design of coleman transform-based individual pitch controllers for wind-turbine load reduction," *Wind Energy*, vol. 18, no. 8, pp. 1451–1468, Jun. 2014. DOI: 10.1002/we.1769.

[39] S. Navalkar, J. van Wingerden, E. van Solingen, T. Oomen, E. Pasterkamp, and G. van Kuik, "Subspace predictive repetitive control to mitigate periodic loads on large scale wind turbines," *Mechatronics*, vol. 24, no. 8, pp. 916–925, Dec. 2014. DOI: 10.1016/j.mechatronics.2014.01.005.

[40] Y. Liu, R. M. G. Ferrari, and J. W. van Wingerden, "Periodic load rejection for floating offshore wind turbines via constrained subspace predictive repetitive control," in *2021 American Control Conference (ACC)*, IEEE, May 2021. DOI: 10.23919/acc50511.2021.9483333.

[41] F. D. Freijedo, A. Vidal, A. G. Yepes, *et al.*, "WLSE for fast, accurate and robust generation of references in power converter applications," in *2010 IEEE International Symposium on Industrial Electronics*, IEEE, Jul. 2010. DOI: 10.1109/isie.2010.5637405.

[42] L. Zheng, H. Geng, and G. Yang, "Fast and robust phase estimation algorithm for heavily distorted grid conditions," *IEEE Transactions on Industrial Electronics*, vol. 63, no. 11, pp. 6845–6855, Nov. 2016. DOI: 10.1109/tie.2016.2585078.

[43] T. Richardson and R. Kwong, "On positive definite solutions to the algebraic riccati equation," *Systems & Control Letters*, vol. 7, no. 2, pp. 99–104, Apr. 1986. DOI: 10.1016/0167-6911(86)90014-9.

[44] E. Simley and L. Y. Pao, "Evaluation of a wind speed estimator for effective hub-height and shear components," *Wind Energy*, vol. 19, no. 1, pp. 167–184, Dec. 2014. DOI: 10.1002/we.1817.

[45] S. Gre, M. Döhler, P. Andersen, and L. Mevel, "Kalman filter-based subspace identification for operational modal analysis under unmeasured periodic excitation," *Mechanical Systems and Signal Processing*, vol. 146, p. 106 996, Jan. 2021. DOI: 10.1016/j.ymssp.2020.106996.

[46] A. A. W. van Vondelen, J. Ottenheym, A. Pamososuryo, S. T. Navalkar, and J. van Wingerden, "Phase synchronization for helix enhanced wake mixing in downstream wind turbines," *Work submitted for publication*, 2023.

[47] M. Verhaegen and V. Verdult, *Filtering and System Identification*. Cambridge University Press, Apr. 2007. DOI: 10.1017/cbo9780511618888.

[48] A. Sayed and T. Kailath, "A state-space approach to adaptive RLS filtering," *IEEE Signal Processing Magazine*, vol. 11, no. 3, pp. 18–60, Jul. 1994. DOI: 10.1109/79.295229.

[49] P. Pillay and R. Krishnan, "Modeling of permanent magnet motor drives," *IEEE Transactions on Industrial Electronics*, vol. 35, no. 4, pp. 537–541, 1988. DOI: 10.1109/41.9176.

[50] S. Chai, L. Wang, and E. Rogers, "Model predictive control of a permanent magnet synchronous motor with experimental validation," *Control Engineering Practice*, vol. 21, no. 11, pp. 1584–1593, Nov. 2013. DOI: 10.1016/j.conengprac.2013.07.008.

[51] A. Favato, P. G. Carlet, F. Toso, and S. Bolognani, "A model predictive control for synchronous motor drive with integral action," in *IECON 2018 - 44th Annual Conference of the IEEE Industrial Electronics Society*, IEEE, Oct. 2018. DOI: 10.1109/iecon.2018.8591769.

[52] L. Ljung, *System identification*, Dec. 1999. DOI: 10.1002/047134608x.w1046.

[53] J. Jonkman, S. Butterfield, W. Musial, and G. Scott, "Definition of a 5-MW reference wind turbine for offshore system development," Tech. Rep., Feb. 2009. DOI: 10.2172/947422.

[54] S. G. R. Energy. "Sg 14-236 dd." (2022), [Online]. Available: https://www.siemensgamesa.com/products-and-services/offshore/wind-turbine-sg-14-236-dd (visited on 01/12/2023).

[55] K. Stol, H.-G. Moll, G. Bir, and H. Namik, "A comparison of multi-blade coordinate transformation and direct periodic techniques for wind turbine control design," in *47th AIAA Aerospace Sciences Meeting including The New Horizons Forum and Aerospace Exposition*, American Institute of Aeronautics and Astronautics, Jan. 2009. DOI: 10.2514/6.2009-479.

[56] NREL. "Openfast." (2018), [Online]. Available: http://openfast.readthedocs.io (visited on 06/16/2022).

[57] P. J. Moriarty and A. C. Hansen, "AeroDyn theory manual," Tech. Rep., Jan. 2005. DOI: 10.2172/15014831.

[58] B. J. Jonkman, "Turbsim user's guide: Version 1.50," Sep. 2009. DOI: 10.2172/965520.

[59] D. Marten, C. O. Paschereit, X. Huang, *et al.*, "Predicting wind turbine wake breakdown using a free vortex wake code," *AIAA Journal*, vol. 58, no. 11, pp. 4672–4685, Nov. 2020. DOI: 10.2514/1.j058308.

[60] D. Marten, *Qblade: A modern tool for the aeroelastic simulation of wind turbines*, en, 2020. DOI: 10.14279/DEPOSITONCE-10646.

[61] D. van den Berg, D. de Tavernier, and J. van Wingerden, "Using the helix mixing approach on floating offshore wind turbines," *Journal of Physics: Conference Series*, vol. 2265, no. 4, p. 042 011, May 2022. DOI: 10.1088/1742-6596/2265/4/042011.

[62] L. Bergami and M. Gaunaa, *Ateflap aerodynamic model, a dynamic stall model including the effects of trailing edge flap deflection*, Feb. 2012.

[63] R. J. Barthelmie, J. P. Palutikof, and T. D. Davies, "Estimation of sector roughness lengths and the effect on prediction of the vertical wind speed profile," *Boundary-Layer Meteorology*, vol. 66, no. 1-2, pp. 19–47, Oct. 1993. DOI: 10.1007/bf00705458.

[64] S. A. Hsu, E. A. Meindl, and D. B. Gilhousen, "Determining the power-law wind-profile exponent under near-neutral stability conditions at sea," *Journal of Applied Meteorology*, vol. 33, no. 6, pp. 757–765, Jun. 1994. DOI: 10.1175/1520-0450(1994)033<0757:dtplwp>2.0.co;2.

[65] M. Churchfield and S. Lee, *Sowfa: Simulator for wind farm applications*, 2015. [Online]. Available: https://www.nrel.gov/wind/nwtc/sowfa.html.

[66] C. Bak, F. Zahle, R. Bitsche, *et al.*, *The dtu 10-mw reference wind turbine*, English, Danish Wind Power Research 2013 ; Conference date: 27-05-2013 Through 28-05-2013, 2013.

[67] NREL. "Openfast documentation v2.4.0." (2020), [Online]. Available: https://raf-openfast.readthedocs.io/en/docs-fast8readme/ (visited on 01/20/2023).

[68] S. Sastry, M. Bodson, and J. F. Bartram, "Iadaptive control: Stability, convergence, and robustness/i," *The Journal of the Acoustical Society of America*, vol. 88, no. 1, pp. 588–589, Jul. 1990. DOI: 10.1121/1.399905.

[69] B. Ni and Q. Zhang, "Stability of the kalman filter for output error systems," *IFAC-PapersOnLine*, vol. 48, no. 28, pp. 1106–1111, 2015. DOI: 10.1016/j.ifacol.2015.12.279.

[70] Q. Zhang, "On stability of the kalman filter for discrete time output error systems," *Systems & Control Letters*, vol. 107, pp. 84–91, 2017.

[71] R. E. Kálmán, "Contributions to the theory of optimal control," 1960.

[72] L. Zhang and Q. Zhang, "Observability conservation by output feedback and observability gramian bounds," *Automatica*, vol. 60, pp. 38–42, Oct. 2015. DOI: 10.1016/j.automatica.2015.06.031.

[73] F. Zhang, Ed., *The Schur Complement and Its Applications*. Springer-Verlag, 2005. DOI: 10.1007/b105056.

[74] R. E. Kalman, "Mathematical description of linear dynamical systems," *Journal of the Society for Industrial and Applied Mathematics Series A Control*, vol. 1, no. 2, pp. 152–192, Jan. 1963. DOI: 10.1137/0301010.

[75] E. D. Sontag, *Mathematical Control Theory*. Springer New York, 1998. DOI: 10.1007/978-1-4612-0577-7.

[76] H. K. Khalil, *Nonlinear Systems*, ser. Pearson Education. Prentice Hall, 2002, ISBN: 9780130673893.

[77] M. A. Sprague, S. Ananthan, G. Vijayakumar, and M. Robinson, "ExaWind: A multifidelity modeling and simulation environment for wind energy," *Journal of Physics: Conference Series*, vol. 1452, no. 1, p. 012 071, Jan. 2020. DOI: 10.1088/1742-6596/1452/1/012071.

# Glossary

## List of Acronyms

| | |
|---|---|
| **IPC** | Individual Pitch Control |
| **CFD** | Computational Fluid Dynamics |
| **TSR** | Tip-Speed Ratio |
| **LCoE** | Levelized Cost of Energy |
| **AIC** | Axial Induction Control |
| **DIC** | Dynamic Induction Control |
| **MBC** | Multi-Blade Coordinate |
| **TI** | Turbulence Intensity |
| **DEL** | Damage Equivalent Load |
| **CW** | Clockwise |
| **CCW** | Counter-Clockwise |
| **PSD** | Power Spectral Density |
| **BOoP** | Blade Out-of-Plane |
| **NR** | Non-rotating |
| **DC** | Direct Current |
| **1P** | Once-per-Revolution |
| **LP** | Low-Pass |
| **MAF** | Moving-Average Filter |
| **SISO** | Single-Input Single-Output |
| **MIMO** | Multi-Input Multi-Output |
| **RLS** | Recursive Least Squares |
| **KF** | Kalman Filter |
| **PMSM** | Permanent Magnet Synchronous Machine |
| **GT** | Ground Truth |
| **RMSE** | Root-Mean-Square Error |
| **SNR** | Signal-to-Noise Ratio |
| **LTI** | Linear Time-Invariant |
| **LPV** | Linear Parameter-Varying |
| **BEM** | Blade Element Momentum |
| **PL** | Power Law |
| **LES** | Large Eddy Simulations |
| **ALM** | Actuator Line Model |
| **BL** | Baseline |